UNIVERSIDAD COMPLUTENSE DE MADRID

FACULTAD DE CIENCIAS FÍSICAS
Departamento de Óptica

FIRST-ORDER OPTICAL SYSTEMS IN INFORMATION PROCESSING AND OPTRONIC DEVICES

MEMORIA PARA OPTAR AL GRADO DE DOCTOR

PRESENTADA POR

José Augusto Rodrigo Martín-Romo

Bajo la dirección de las doctoras
Tatiana Alieva y María L. Calvo

Madrid, 2008

- **ISBN: 978-84-669-3198-4**

Universidad Complutense de Madrid

Facultad de Ciencias Físicas

Departamento de Óptica

First-order optical systems in information processing and optronic devices

Sistemas ópticos de primer orden en procesado de información y dispositivos optrónicos

Autor/Author:
José A. Rodrigo

Directores/Supervisors:
Dr. Tatiana Alieva
Dr. María L. Calvo

June 19, 2008

Preface

This Thesis concludes my research on first-order optical systems in information processing and optronic devices, which has been developed in almost four years. The first part of this book corresponds to a brief summary written in Spanish, as it is demanded by Universidad Complutense de Madrid, UCM. I would like to thank to UCM for let me write my Thesis in English.

Optical information processing together with optoelectronic and holography are exciting research fields which had caught my imagination during these years. I am grateful to my supervisors: Tatiana Alieva and María Luisa Calvo, who are possibly even more enthusiastic about the topic than I am. Thanks for all the time you devoted to, and interested you showed in, this research.

The financial support of the Spanish Ministry of Education and Science under project TIC 2002-01846 via the FPI research fellowship as well as the project TEC 2005-02180 and "Slab Waveguide Spatial Heterodyne Spetrometer project", Contract ref. 9F028−064201/007/MTB, Space Technology Development Program of Canada Space Agency, are acknowledged.

José A. Rodrigo Martín-Romo
March, 2008.

Dedicado a mis padres y hermana.

Este trabajo ha sido financiado por los proyectos TIC 2002-01846 y TEC 2005-02180 del Ministerio de Educación y Ciencia. Mi sincero agradecimiento al Ministerio de Educación y Ciencia por la concesión de la beca FPI asociada a TIC 2002-01846.

Resumen

Introducción

A lo largo de las últimas décadas, la óptica ha desempeñado un papel relevante en diferentes áreas tales como telecomunicaciones, tecnologías de computación, almacenamiento de datos, optoelectrónica, procesado de información, etc. Por ejemplo, en el área de la comunicaciones y almacenamiento de datos las tecnologías ópticas han ido reemplazando gradualmente las tecnologías electrónicas. No obstante, en general la óptica es empleada de forma complementaria con la electrónica.

El desarrollo de una gran variedad de sistemas ópticos de primer orden ha permitido realizar diferentes operaciones de gran interés en procesado óptico de la información, tales como: caracterización de haces, transformación de modos, filtrado, encriptación, correlación, etc. Estos sistemas paraxiales se construyen a partir de elementos básicos como lentes delgadas, prismas, intervalos espaciales, etc. Actualmente las transformaciones fraccionarias tienen una gran importancia ya que permiten realizar estas operaciones ofreciendo un grado de libertad extra, el orden fraccionario. La implementación óptica de tales transformaciones, a través combinación de lentes e intervalos espaciales, ha experimentado un gran avance en los últimos años. La lista de operaciones aumenta considerablemente al aplicar lentes cilíndricas. De hecho, esto permite implementar operaciones atractivas como rotación de haces (o imágenes), transformada fraccionaria de Fourier (FRFT) separable y gyrator (GT). Otras trasnformaciones fraccionarias como la transformada de Hilbert también se pueden implementar ópticamente gracias a estos sistemas.

Hasta ahora, los diseños ópticos propuestos para realizar transformaciones fraccionarias no son flexibles puesto que éstas se ven afectadas por factores extras de escala, rotación y fase en función del orden fraccionario. Nuestro objetivo principal es la obtención de un diseño óptico flexible capaz de realizar estas transformaciones sólo a través de la rotación de lentes cilíndricas sin cambiar la distancia entre ellas. En particular, nos centramos en las operaciones de rotación, FRFT separable y GT. Este esquema es una idea relevante de esta investigación ya que además ofrece una notable ventaja frente a sistemas no flexibles en los que es necesario ajustar la distancia entre las lentes y los planos de entrada-salida. Puesto que cualquier sistema óptico paraxial cuadrático se descompone en función de los sistemas asociados a la FRFT separable y de rotación, la obtención del diseño flexible propuesto tiene una gran importancia.

El estudio correspondiente tanto a este diseño como a su implementación óptica experimental es realizado en detalle a lo largo de este trabajo. Dedicamos tres de los siete capítulos a la operación GT ya que es poco conocida por la comunidad óptica. De hecho, analizamos detalladamente por primera vez sus principales propiedades e implementación óptica experimental. La operación GT ofrece interesantes aplicaciones como la generación óptica de modos estables (singulares o no) que son también estudiadas en detalle. Así pues, podemos destacar la originalidad de este estudio que ha permitido introducir la transformada gyrator.

Un gran número de dispositivos optoelectrónicos basados en sistemas ópticos de primer orden han sido desarrollados en las últimas décadas. Estos tipos de dispositivos son ampli-

amente demandados por diferentes áreas, desde biomedicina a telecomunicaciones ópticas. En particular, diferentes diseños de microespectrómetros han sido propuestos con el objetivo principal de reducir su tamaño sin afectar significativamente a sus prestaciones. En el último capítulo proponemos el diseño de un microespectrómetro de Fourier basado en redes de guías de onda (AWG). El estudio analítico realizado no solo permite obtener un diseño optimizado del dispositivo, sino que también describe su comportamiento. La recuperación de la información espectral (para el infrarrojo cercano, 1500 nm) se realiza gracias a su esquema interferométrico compacto, alcanzado una resolución espectral de hasta 0.3 nm. Los resultados numéricos correspondientes a su simulación ilustran su funcionamiento, demostrando un gran acuerdo con los resultados teóricos encontrados. Ciertamente, el diseño propuesto para este tipo de dispositivo resulta innovador. Además se analiza por primera vez los efectos, en este tipo de dispositivos, de la difracción de la luz para el régimen de campo cercano de Fresnel. El diseño permite una reducción de hasta -40 dB del ruido originado por interferencias entre canales (*crosstalk*).

A lo largo de las siguientes secciones se realiza un breve resumen de los resultados obtenidos y conclusiones, expuestos en los siete capítulos de esta Tesis doctoral.

Capítulo 1

Introducción a sistemas ópticos de primer orden

En este capítulo se introduce el formalismo matricial que describe y caracteriza a los sistemas ópticos de primer orden, también conocidos como sistemas **ABCD**. Estos sistemas paraxiales tales como lentes delgadas, espejos, prismas, intervalos espaciales, etc. juegan un papel muy importante en el procesado óptico de la información. Nótese que por intervalo se entiende la región por dónde la luz se propaga en el espacio libre. Sistemas ópticos sofisticados pueden ser construidos gracias a la combinación de elementos ópticos básicos como son las lentes delgadas e intervalos espaciales. Todos estos sistemas están caracterizados por la matriz real 4×4 de transformación de rayos $\mathbf{T}$, Ec. (1.1). Esta matriz parametriza el kernel de la transfomada canónica integral lineal que describe la evolución del campo de amplitud compleja a través del sistema óptico, Ec. (1.2). Además la matriz de transformación es simpléctica, Ec. (1.4), lo que implica que sólo hay diez parámetros libres. La descomposición modificada de Iwasawa, Ec. (1.7), permite expresar la matriz $\mathbf{T}$ a través del producto de tres matrices asociadas a: una escala asimétrica, una fase cuadrática correspondiente a una lente anamórfica, y finalmente a un sistema orto-simpléctico. Precisamente esta última matriz da cuenta de una serie de transformaciones de gran interés, en particular: rotación, transformada FRFT separable y GT. Varios ejemplos de sistemas ópticos de primer orden como lentes y el sistema correspondiente a la operación FRFT simétrica son introducidos.

Nuestro objetivo es obtener un diseño óptico flexible para realizar dichas transformaciones orto-simplécticas. Por tanto también realizamos una introducción a estas transformaciones, sección 1.1.1. Las submatrices, que componen la matriz de transformación de rayos 4×4, asociadas a estas tres operaciones están dadas por las ecuaciones Ec. (1.13), Ec. (1.15) y Ec. (1.17), respectivamente. Puesto que cualquier sistema orto-simpléctico está dado por la composición del sistema asociado a la transformada FRFT separable embebido en dos sistemas rotadores, Ec. (1.22), este estudio tiene una importancia manifiesta.

Capítulo 2

Diseño óptico para transformaciones orto-simplécticas en espacio de fase

Tal y como hemos mencionado, el diseño óptico asociado a diferentes transformaciones orto-simplécticas, es realizado a través del formalismo matricial para sistemas ópticos paraxiales (sin pérdidas) de primer orden. En nuestro caso nos centramos en tres transformaciones orto-simplécticas básicas: transformada FRFT separable, operación rotador y la operación GT. El análisis de la matriz de transformación de rayos (**ABCD**), correspondiente a estos sistemas, permite alcanzar una configuración óptica escrita como producto de matrices asociadas a lentes generalizadas y a intervalos equidistantes. Nótese que por intervalo espacial se entiende la separación entre lentes generalizadas consecutivas, conjunto de lentes cilíndricas en contacto y alineadas entre sí [Ec. (2.1)], donde la luz se propaga en el espacio libre. Puesto que estamos interesados en una configuración flexible, se ha de imponer sobre esta descomposición dos restricciones: la distancia entre lentes generalizadas es fija (constante) y la rotación de las lentes es variable pero dada en función de los parámetros de transformación considerada. Los fundamentos correspondientes a sistemas ópticos de primer orden y al diseño de estos sistemas se exponen en el capítulo 1 y en la sección 2.1, respectivamente.

Un análisis detallado de los sistemas simétricos, asociados a esta configuración óptica, permite encontrar el número mínimo de lentes e intervalos necesarios correspondientes a la transformada FRFT separable y a la transformada de gyrator, sección 2.2. Concretamente, la implementación óptica de ambas transformaciones requiere el empleo de dos intervalos (de

distancia z) y tres lentes generalizadas, donde la primera y última lente son idénticas. En el caso de la transformada FRFT las submatrices asociadas a estas lentes ($\mathbf{L}_1$ y $\mathbf{L}_2$) están dadas por Ecs. (2.23), mientras que para la transformada gyrator están dadas por Ecs. (2.24). A partir de estos resultados se extraen dos importantes conclusiones: el sistema óptico es capaz de realizar la transformada FRFT antisimétrica y gyrator sólo a través de la rotación de las lentes para un rango determinado de parámetros de transformación, y además ha de ser simétrico. También a partir de este análisis se puede encontrar las expresiones correspondientes a los casos singulares asociados a FRFT separable. En efecto, para el caso en el que uno de los ángulos de transformación (γ_x o γ_y) es múltiplo entero de π, por ejemplo $\gamma_y = \pi$, la transformación puede ser implementada ópticamente gracias al esquema anteriormente mencionado. Concretamente las lentes generalizadas están dadas por las expresiones Ecs. (2.26). No obstante, en los casos singulares correspondientes a la transformada FRFT con ángulos γ_x y/o γ_y igual a 0, y la operación gyrator para $\alpha = 0$ (ambas asociadas a la transformación identidad trivial) no pueden ser realizados por el sistema propuesto.

Una vez determinado el sistema óptico, asociado a estas dos transformaciones, es necesario realizar el análisis concerniente al diseño e implementación óptica de las lentes generalizadas $\mathbf{L}_1$ y $\mathbf{L}_2$ requeridas, tal y como se demuestra en la sección 2.3. La transformada FRFT antisimétrica $\gamma_x = -\gamma_y = \alpha$ y GT, pueden ser implementadas gracias a lentes generalizadas correspondientes al conjunto formado por dos lentes cilíndricas y una esférica convergente. La submatriz de esta configuración, denominada triplete, esta dada por Ec. (2.27). En ambos casos la potencia de las lentes está dada en función de la distancia z de los intervalos, que es constante. Dado que dicha distancia se mantiene fija, sólo un cierto rango de valores del ángulo de transformación α puede ser alcanzado. Una discusión más detallada acerca de la configuración óptica de las lentes generalizadas para el caso $\gamma_x = -\gamma_y = \alpha$ y GT es realizada en el capítulo 3 y 6, respectivamente. Las lentes generalizadas asociadas a la transformada FRFT con ángulos de transformación γ_x y γ_y no pueden ser implementadas a través de la configuración triplete ya que corresponden a un conjunto de dos lentes cilíndricas cruzadas y de focal variable. Este caso también es analizado en el capítulo 3, página 17. Cabe mencionar que una alternativa a la implementación de estas lentes es el empleo de moduladores espaciales de luz (SLM).

Finalmente, el diseño óptico asociado a la operación rotator es analizado en la sección 2.4. Parte de las publicaciones concernientes a la implementación óptica de esta operación realmente tratan el caso de un rotador imperfecto ya que añade una fase adicional al campo óptico rotado. Otras, sin embargo, corresponden a reflectores con rotación (véanse referencias en sección 2.4). Nuestra estrategia es la misma que hemos empleado anteriormente, es decir, encontrar el número mínimo de lentes generalizadas e intervalos tal que la transformación pueda ser realizada tan sólo gracias a la rotación de las lentes. A este respecto hay que añadir la idea de lograr en primer lugar el diseño de un rotador imperfecto para luego corregir la fase adicional empleando una lente más. Esto permite demostrar que el sistema óptico correspondiente a la operación de rotación ha de ser asimétrico, estando constituido por la combinación de cuatro lentes generalizadas [Ecs. (2.40)] y cuatro intervalos espaciales. Al igual que en los casos anteriores la distancia z entre lentes generalizadas se mantiene fija. Este análisis nos ha permitido demostrar que la configuración encontrada para la operación de rotación es la que requiere un menor número tanto de lentes como de intervalos. Una discusión detallada acerca de su implementación óptica, ha tener en cuenta experimentalmente, es realizada en el capítulo 3.

Capítulo 3

Implementación óptica para la transformada fraccionaria de Fourier separable y la operación rotador

Puesto que cualquier sistema óptico paraxial de primer orden puede expresarse como la combinación de los sistemas asociados a FRFT separable embebido en dos rotadores, la implementación óptica de ambas transformaciones tiene un papel muy importante. Además, este resultado permite calcular numéricamente una transformada canónica lineal e integral (TCL) a través de algoritmos convencionales desarrollados para la transformada fraccionaria de Fourier. Gracias al diseño propuesto en el capítulo 2, alternativamente se puede calcular numéricamente una TCL empleando un algoritmo basado en la propagación de la luz bajo el régimen de difracción de Fresnel (intervalos) y funciones de modulación de fase asociadas a las lentes. De hecho este algoritmo es empleado en la simulación numérica de los sistemas ópticos considerados en este trabajo. Una breve discusión acerca del algoritmo para la difracción de la luz es presentada en el apéndice A.

El propósito principal de este capítulo es realizar un análisis detallado de la implementación óptica de las trasformaciones FRFT separable y rotator, encontrada anteriormente. Dicho análisis ha de tenerse en cuenta para su implementación experimental. Además se consideran diferentes simulaciones numéricas con el objetivo de ilustrar ambas transformaciones. El capítulo comienza analizando operación FRFT para ángulos de transformación arbitrarios. En este caso estos ángulos γ_x y γ_y no pueden ser cambiados a través de la rotación de las lentes cilíndricas, y es necesario ajustar la potencia de estas lentes para cada combinación de ángulos. No obstante el sistema es flexible puesto que la distancia entre las lentes es constante para cualquier valor de los ángulos de transformación. La implementación óptica de estas lentes puede ser realizada empleando SLM o a través de hologramas multiplexados. No obstante, en el caso particular de la operación FRFT antisimétrica ($\gamma_x = -\gamma_y = \alpha$) el ángulo de transformación α si puede ser cambiado solamente a través de la rotación de lentes. Para este caso las lentes pueden ser implementadas empleando la configuración triplete anteriormente analizada, Ec. (2.27).

La evolución del campo complejo a lo largo de este sistema para ambos casos es estudiada, encontrando su expresión analítica. A través de este estudio se encuentran las curvas de operación (Figs. 3.1 y 3.4) correspondientes a las lentes cilíndricas, dadas respectivamente por las expresiones Ec. (3.7) y Ec. (3.13). También se determina el factor de escala en función de la longitud de onda λ y de la distancia z del intervalo.

A modo de ejemplo, una simulación numérica (Fig. 3.2) es realizada con el fin de ilustrar dicha transformación para el caso $\gamma = 2\gamma_x = -\gamma_y$: $\gamma = 0$ (a), $\gamma = \pi/4$ (b), $\gamma = \pi/2$ (c), y $\gamma = 3\pi/4$ (d). Los parámetros empleados en esta simulación son $\lambda = 532$ nm, y $z = 0.5$ m donde el tamaño de la imagen de entrada es 428×256 píxeles. Los resultados concuerdan con las predicciones teóricas, demostrando la viabilidad del algoritmo propuesto.

La implementación óptica de la operación rotador requiere emplear un mayor número de lentes que en el caso de la transformada FRFT. Concretamente son necesarios cuatro intervalos y cuatro lentes generalizadas (en total ocho lentes cilíndricas). Ciertamente la implementación experimental de este sistema, aún siendo flexible, resulta relativamente costosa. No obstante, la configuración óptica encontrada es la óptima puesto que requiere el menor número de lentes e intervalos para construir un rotador puro. De hecho otro sistema rotador propuesto por Simon et al., basado también en la combinación de lentes-intervalos, requiere emplear diez lentes y ocho intervalos. Dicho sistema realmente corresponde a la combinación en cascada de dos reflectores, tal que la rotación de uno con respecto al otro permite realizar la transformación. Resulta pues evidente la notable ventaja experimental que implica el sistema rotador encontrado en este trabajo frente al anterior. Cabe mencionar que la operación de rotación puede ser realizada por otros sistemas sin lentes como por ejemplo la combinación

de dos prismas Dove, los cuales presentan problemas tales como la alteración del estado de polarización del haz. Puesto que cualquier sistema paraxial de primer orden puede ser construido a través de la combinación de los sistemas asociados a la transformada FRFT y rotador, es oportuno comentar que esto no implica necesariamente que tales sistemas requieran el empleo de un exagerado número de lentes. De hecho esto queda demostrado en el caso de la transformada de gyrator (tres lentes generalizadas y dos intervalos).

Capítulo 4

Propiedades de la transformada gyrator

Otro de los resultados importantes obtenidos en este trabajo concierne tanto al diseño óptico como al estudio de la operación GT. En este capítulo estudiamos en detalle las propiedades básicas de esta transformación, se determina analíticamente la transformada de gyrator para una lista de funciones habituales (Tabla 4.3), y se presenta la acción de GT como conversor óptico de modos estables. A pesar de que GT pertenece, al igual que la operación FRFT, al conjunto de transformaciones canónicas integrales lineales, es aún una operación poco conocida. Cabe resaltar que GT ofrece interesantes resultados que pueden ser de utilidad en procesado óptico de la información, caracterización de haces, computación cuántica, generación y transformación de modos, etc.

Mientras que el kernel de la transformada FRFT separable [Ec. (3.1)] se expresa como el producto de ondas planas y esféricas con ángulos de transformación γ_x y γ_y, el kernel de GT [Ec. (4.1), página 27] se expresa como el producto de ondas planas e hiperbólicas con ángulo α. Esto permite realizar una rotación acompañada de una *torsión* en torno a los planos (x, q_y) y (y, q_x) (posición-frecuencia espacial) en el espacio de fase. A modo de ejemplo, el kernel de GT es representado gráficamente en el caso $\alpha = \pi/4$ para coordenadas de salida $x_o = y_o = 0$ y $2x_o = y_o = 1$ en Fig. 4.1(a) y (b), respectivamente.

Para $\alpha = 0$ GT corresponde a la transformación identidad, para $\alpha = \pi/2$ se reduce a la FRFT antisimétrica con ángulo $\pi/2$ acompañada de una rotación $\pi/2$ de coordenadas. Para $\alpha = \pi$ la transformación descrita por el kernel $\delta(\mathbf{r}_o + \mathbf{r}_i)$. Resulta fácil demostrar que GT es una transformación cíclica y periódica a partir su matriz de transformación $\mathbf{T}$ [Ec. (4.2)], es decir, $\mathbf{T}(\alpha)\,\mathbf{T}(\beta) = \mathbf{T}(\alpha + \beta)$. La transformación inversa corresponde a GT con $-\alpha$, Ec. (4.4). Al igual que el resto de TCL, GT satisface la relación de Parseval como se demuestra en Ec. (4.5).

La aplicación de GT sobre una función de entrada $f_i(\mathbf{r})$ para un ángulo α será indicado en lo sucesivo como $R^{\alpha}[f_i(\mathbf{r}_i)](\mathbf{r_o})$. Una de las propiedades básicas a estudiar es la asociada al desplazamiento (*shift*) de la función de entrada: $R^{\alpha}[f_i(\mathbf{r}_i - \mathbf{v})](\mathbf{r}_o)$. Esta operación da como resultado un desplazamiento $\mathbf{v}\cos\alpha$ de la función de salida que además está modulada por una onda plana inclinada, Ec. (4.6). Por otro lado, el efecto de la modulación de $f_i(\mathbf{r})$ por una onda plana $\exp(-i2\pi\mathbf{k}^t\mathbf{r}_i)$ da un resultado [Ec. (4.7)] similar al obtenido en el caso de la transformada FRFT. Un resultado importante a tener en cuenta corresponde también al teorema de escala, formulado en el caso de GT a través de la expresión Ec. (4.8). A partir de este teorema se concluye que la operación GT de una función escalada, $R^{\alpha}[f_i(\mathbf{S}\mathbf{r}_i)](\mathbf{r}_o)$, implica una modulación de fase adicional correspondiente a una onda hiperbólica aplicada sobre la transformación GT: $R^{\beta}[f_i(\mathbf{r}_i)]\,((\cos\beta/\cos\alpha)\mathbf{S}\mathbf{r}_o)$, donde $\cot(\beta) = \cot(\alpha)/s_x s_y$. En función de los parámetros de escala s_x y s_y se distinguen diferentes casos como Ecs. (4.10)−(4.13), que son demostrados en la sección 5.1.2 como aplicación particular en la generación haces elípticos con estructura helicoidal.

La Tabla 4.3 contiene una lista de la transformación bajo GT de diferentes funciones. De entre estos resultados destacamos el caso correspondiente a la onda hiperbólica $\exp(i2\pi c x_i y_i)$, fila 2, ya que ésta se transforma a delta de Dirac bajo la acción de GT si el ángulo de transformación satisface la relación $\cot\alpha = -c$. Este resultado es importante ya que permite emplear GT para la detección de ondas hiperbólicas contenidas en un frente de ondas. De hecho este

resultado tiene como aplicación la eliminación de ruido aditivo con estructura hiperbólica, tal y como demostramos en el capítulo 5 dedicado a las aplicaciones básicas de GT en procesado de imágenes. Otra propiedad interesante es encontrada al aplicar GT sobre una función periódica. Tal y como se demuestra a partir de Ec. (4.19), una función periódica transformada por GT presenta un efecto [Ec. (4.20)] análogo al de Talbot.

Un resultado importante y de gran interés concierne a la transformación de modos Hermite-Gauss $\mathrm{HG}_{m,n}(\mathbf{r};w)$ a través de GT. Los modos Hermite-Gauss, Ec. (4.14), son estables puesto que mantienen su estructura a lo largo de su propagación en el espacio libre y aparecen de forma natural en cavidades láser. Bajo la acción de GT un modo $\mathrm{HG}_{m,n}$ se transforma en un Laguerre-Gauss, Ec. (4.16), para un rango de ángulos α concretos. Los modos Laguerre-Gauss $\mathrm{LG}^{\pm}_{p,l}(\mathbf{r};w)$ también son estables y gozan de gran interés en diversas aplicaciones por tratarse de haces singulares capaces de transferir momento orbital angular (OAM). Los índices se denominan radial $p = \min(m,n)$ y carga topológica $l = |m-n|$; número de saltos 2π en la distribución de fase del modo. En concreto el OAM transferido es $l\hbar$, y la singularidad o indeterminación en el valor de la fase es la responsable del área con distribución de intensidad nula que distingue a este tipo de haces. Cabe resaltar que los modos Hermite-Gauss son autofunciones de la transformada fraccionaria de Fourier y por tanto lo son de la transformada gyrator si el modo está rotado en $\pi/4$ (fila 7, Tabla 4.3). Esto no resulta extraño puesto que como se mencionó anteriormente GT se puede expresar en función de la operación FRFT, véase Ec. (1.23).

Capítulo 5

Aplicaciones de la transformada gyrator: conversor óptico de modos y procesado de imágenes

La transformación de modos Hermite-Gauss a Laguerre-Gauss es ilustrada gracias a diferentes ejemplos calculados numéricamente para diferentes valores del ángulo de transformación. Nótese que el cálculo numérico de la integral asociada a GT corresponde a la simulación numérica del sistema óptico asociado a GT para valores $\lambda = 532$ nm, $w = 0.73$ mm, y resolución espacial de 20 μm. Para los ángulos de transformación $\alpha = \pi/4,\ 3\pi/4,\ 5\pi/4, 7\pi/4$ un modo $\mathrm{HG}_{m,n}(\mathbf{r};w)$ se transforma en $\mathrm{LG}^{\pm}_{p,l}(\mathbf{r};w)$ mientras que para el resto de valores se obtiene un modo intermedio. La secuencia de resultados asociada a tal transformación es representada en Fig. 5.1 para el caso $\mathrm{HG}_{1,0}$, página 36. Los modos obtenidos para cualquier ángulo α son estables y poseen OAM fraccionario. Las propiedades de escala y desplazamiento o *shift* discutidas anteriormente son ilustradas gráficamente en Figs. 5.2 y 5.3, respectivamente. Finalmente, demostramos la transformación de la composición de modos $\mathrm{HG}_{3,0} + \mathrm{HG}_{0,3}$ a la combinación $\mathrm{LG}^{+}_{0,3} + \mathrm{LG}^{-}_{0,3}$, bajo la acción de GT para valores α comprendidos entre 0 y $\pi/4$, Fig. 5.4. Los resultados obtenidos hacen pensar que la operación GT puede jugar un papel importante en determinadas aplicaciones como generación de modos, caracterización de haces, holografía, computación cuántica, entre otras. De hecho GT puede ser considerado como un conversor de modos sintonizable y universal. Así pues, su implementación experimental tiene un peso relevante en este trabajo tal y como demostramos en el siguiente capítulo.

El propósito de incluir GT en la lista de herramientas de procesado de imágenes, implica realizar un estudio acerca de su empleo en ciertas tareas básicas tales como filtrado, reducción de ruido y encriptación óptica. Es oportuno recordar que sistemas ópticos de primer orden capaces de realizar la operación FRFT han sido ampliamente aplicados en tareas como filtrado variante, reducción de ruido, encriptación, etc. El empleo de GT aún ofreciendo resultados análogos a los obtenidos empleando la transformada FRFT, abre nuevas perspectivas en procesado de imágenes.

Al contrario que la transformada FRFT, GT sólo puede aplicarse a funciones bidimensionales

por la propia estructura de su kernel, Ec. (4.1). En este caso hemos elegido una imagen de 256×256 píxeles, Lena, empleada habitualmente como test en procesado óptico y digital.

La primera prueba consiste en considerar la reconstrucción la imagen test $f_i(\mathbf{r}_i)$ a partir de la información de sólo-fase o sólo-amplitud asociada al campo transformado por GT para diferentes ángulos de transformación: $R^{\alpha}[f_i(\mathbf{r}_i)](\mathbf{r}_o) = F_{\alpha}(\mathbf{r}_o)\exp(i\varphi_{\alpha}(\mathbf{r}_o))$. Así pues, los resultados correspondientes a las transformaciones $R^{-\alpha}[F_{\alpha}(\mathbf{r}_o)](\mathbf{r})$ y $R^{-\alpha}[\exp(i\varphi_{\alpha}(\mathbf{r}_o))](\mathbf{r})$, permiten concluir que la información esencial de la estructura de la imagen (bordes) es preservada a partir de la información de sólo-amplitud para un pequeño rango de valores α, mientras que a partir de sólo-fase esta información se mantiene para todos los valores α. En Fig. 5.6 se demuestran estos resultados para los casos: (a, e) $\alpha = 2^o$, (b, f) $\alpha = 10^o$, (c, g) $\alpha = 60^o$, (d, h) $\alpha = 90^o$. En conclusión, la parte de información correspondiente al campo complejo es más relevante lo que indica que los filtros de sólo-fase pueden ser aplicados en detección y reconocimiento de patrones en el dominio de GT. En este sentido GT es similar a FT.

Otro ejemplo que ilustra los cambios experimentados en la reconstrucción de la imagen es el de la operación de filtrado en diferentes dominios de la GT. Los casos considerados corresponden a procesos de filtrado pasa-alta (H) y pasa-baja (L), para los cuales se emplea un filtro de amplitud binario de apertura circular localizado en lo que sería el plano de Fourier del sistema ($\alpha = \pi/2$). Ambos filtros, H y L, pueden observarse en Fig. 5.7(a) y Fig. 5.8(a) para $\alpha = 0$. El resto de resultados en Figs. 5.7 y 5.8 demuestran el proceso de filtrado para ángulos α comprendidos entre 0 y $\pi/2$. Cabe resaltar que este proceso no es invariante bajo desplazamiento salvo para el ángulo $\alpha = \pi/2$. En el caso del filtro H el resultado indica un realce selectivo de bordes en función del centrado del filtro, mientras que para el filtro L se obtiene un suavizamiento de la imagen reconstruida. Estos resultados tan sólo indican las tendencias del proceso filtrado en dominio de GT. Procesos más sofisticados han de emplearse en función de la tarea particular considerada.

Anteriormente mencionamos que la transformada gyrator puede emplearse en la detección de ondas hiperbólicas. Concretamente permite la reducción de ruido aditivo de naturaleza hiperbólica, Ec. (5.5). En Fig. 5.9 se muestra el resultado de este proceso de reducción de ruido. La imagen afectada por el ruido [Fig. 5.9(a)] es transformada por GT para un ángulo $\alpha = \arctan(1/c) = 10\pi/9$ tal que la componente asociada al ruido hiperbólico aparece espacialmente separada de la información asociada a la imagen, Fig. 5.9(b). Empleando una máscara para bloquear dicha componente de ruido $\delta(\mathbf{r}_o + \mathbf{v}\cos\alpha)$, Ec. (5.6), se logra reducir casi por completo el ruido en la imagen tal y como se demuestra en Fig. 5.9(c).

Finalmente, el proceso de encriptación propuesto para el caso de GT es propuesto. En general este proceso se puede efectuar de forma sucesiva o iterativa con un cierto número de pasos N, descritos por la expresión Ec. (5.7). Estos pasos corresponden a la aplicación de N operaciones GT sobre el campo modulado por otras tantas funciones de modulación de fase $\exp(i\phi_n)$, $n = 1, 2...N$. Tanto los ángulos α_n de transformación como la función $\phi_n(\mathbf{r})$ actúan como llaves sin las cuales la imagen original no puede ser recuperada. Este proceso de encriptación/decriptación ha sido realizado para el caso $N = 2$ con ángulos $\alpha_1 = 100^o$ y $\alpha_2 = 10^o$, Fig. 5.10. Una de las funciones de fase empleadas se muestra en Fig. 5.10(a), mientras que la imagen encriptada y reconstruida se muestran en (b) y (c), respectivamente. Tal y como puede apreciarse la calidad de la reconstrucción es notable, lo que contrasta con el caso en el que no se emplean las llaves correctas, Fig. 5.10(d). Resultados similares se encuentran para otros valores (α_1, α_2).

Todos estos resultados demuestran el interés y viabilidad de la aplicación de la transformada gyrator en procesado de imágenes. No obstante, un estudio mucho más profundo es requerido para tareas más sofisticadas que las consideradas en este trabajo. El estudio realizado sirve de apoyo en tales tareas.

Capítulo 6

Implementación experimental de la transformada gyrator

La evolución del campo de amplitud compleja a lo largo del sistema óptico asociado a GT se puede determinar analíticamente de forma concisa. Tal y como se demostró anteriormente, este sistema está formado por la combinación de tres lentes generalizadas y dos intervalos. El sistema es simétrico por lo que la primera y última lente son idénticas al igual que ambos intervalos. La configuración triplete que permite implementar ópticamente la lente generalizada, requerida tanto por la transformada FRFT como por GT, puede ser simplificada en el caso de gyrator a un par de lentes cilíndricas convergentes en contacto. La rotación de ambas lentes cilíndricas está dada en función del ángulo de transformación α de GT. El esquema asociado a este sistema y a la lente generalizada se muestra en Fig. 6.1(a) y (b), respectivamente. La función de modulación de fase asociada a la lente generalizada está dada por la expresión Ec. (6.2). Así pues, la evolución del campo complejo $g_i(x_i, y_i)$ a lo largo de este sistema se puede determinar empleando las correspondientes funciones de modulación de las lentes generalizadas y propagando en el régimen de difracción de Fresnel el campo resultante, a través de cada intervalo. En efecto, el campo $g_1(x_1, y_1)$ justo antes de la segunda lente generalizada [Ec. (6.3)] ha de ser modulado por ésta para luego ser propagado de nuevo durante una distancia z [Ec. (6.4)], de tal manera que la última lente generalizada tan sólo corrige su fase dando lugar finalmente a la expresión del campo, Ec. (6.5). Esta última expresión coincide con la definición de la transformada GT con ángulo α excepto en un factor de fase constante y además con una normalización $s^2 = \lambda z$, Ec. (6.1), si la relación dada por Ec. (6.6) es satisfecha.

Precisamente, a partir de la relación Ec. (6.6) se determinan los valores de los ángulos de rotación de las lentes cilíndricas en función del ángulo de transformación α. La representación gráfica de éstos ángulos se conoce con el nombre de curva de operación, Fig. 6.2. Puesto que los ángulos de rotación φ_1 y φ_2, correspondientes a las lentes generalizadas $\mathbf{L}_1$ y $\mathbf{L}_2$, han de satisfacer la relación $\sin 2\varphi_1 = \cot(\alpha/2)$ y $\sin 2\varphi_2 = (\sin\alpha)/2$, la transformación GT sólo se puede efectuar para el rango de ángulos $\alpha \in [\pi/2,\ 3\pi/2]$. No obstante, puesto que $R^{\alpha+\pi}[f_i(\mathbf{r}_i)](\mathbf{r}_o) = R^{\alpha}[f_i(\mathbf{r}_i)](-\mathbf{r}_o)$ se puede cubrir el intervalo $\alpha \in [0,\ 2\pi]$ si fuera necesario. Nótese, que el ángulo de rotación de la primera lente cilíndrica corresponde a $\phi_1 = \varphi_{1,2}$ mientras que para la segunda lente cilíndrica se tiene $\phi_2 = -(\phi_1 + \pi/2)$. Cuando ambas lentes cilíndricas están cruzadas, es decir forman un ángulo $\pi/2$, la lente generalizada corresponde a una lente esférica. Cabe resaltar que para $\alpha = \pi$ todas las lentes generalizadas son lentes esféricas convergentes, y por tanto el sistema asociado a GT se reduce a un sistema 4-f (cascada de dos transformaciones de Fourier). Desde este punto de vista se puede entender el sistema GT como una generalización de un sistema 4-f con lentes generalizadas.

Con el objetivo de demostrar experimentalmente la acción de GT consideramos el caso de la transformación de modos Hermite-Gauss a Laguerre-Gauss. Para ello es necesario disponer de modos Hermite-Gauss con suficiente calidad óptica, como función o señal de entrada. Por esta razón hemos diseñado un sistema basado en dos moduladores espaciales de luz (SLM) acoplados que permiten implementar una función compleja arbitraria, en particular modos Hermite-Gauss. Uno de los moduladores implementa ópticamente la parte correspondiente al módulo de la señal que es proyectada sobre el segundo modulador, el cuál al implementar la fase de la señal permite obtener finalmente la señal compleja a tiempo casi real. El esquema correspondiente a este sistema se muestra en Fig. 6.3. El empleo de dos sistemas 4-f no sólo se reserva para proyectar las componentes de la señal (evitar efectos de difracción no deseados) sino que también permite filtrar ópticamente la señal mejorando así su calidad. La alineación entre ambos SLM se realiza digitalmente a través de un PC lo que simplifica su montaje al evitar el uso de posicionadores de alta precisión. Este sistema permite generar modos Hermite-Gauss con alta calidad óptica incluso para órdenes o índices altos, tal y como se demuestra en Fig. 6.5 para el caso $\mathrm{HG}_{7,4}$. Cabe resaltar que esta es la primera vez que se propone este sistema para

la implementación de este tipo de modos, el cuál ofrece mayor calidad que otros métodos basados en holografía digital y que también emplean el mismo tipo de SLM. Este sistema se discute en este capítulo (página 48) y se amplia en el apéndice C, dónde también se presenta el programa que hemos diseñado para implementar y controlar la señal en ambos SLM.

Los resultados experimentales mostrados en Figs. 6.6−6.8 demuestran la acción de GT sobre una amplia variedad de modos Hermite-Gauss: $HG_{8,6}$, $HG_{3,2}$, $HG_{3,3}$, $HG_{5,3}$ y la composición $HG_{5,2}$ + $HG_{2,5}$. Varios valores del ángulo de transformación son considerados con el objetivo de demostrar la generación de modos intermedios. Todos estos resultados están en excelente acuerdo con las predicciones teóricas y avalan la viabilidad del sistema experimental diseñado. La implementación experimental de GT promete interesantes aplicaciones más allá de la generación de modos estables singulares.

Capítulo 7

Efectos de difracción de Fresnel en microespectrómetro FT-AWG

El diseño del microespectrómetro propuesto requiere el análisis del campo difractado por las estructuras que lo conforman. En el caso particular de dispositivos basados en la tecnología de redes de guía onda AWG (*arrayed waveguide gratings*), este estudio resulta ventajoso. El esquema básico de este microespectrómetro consiste en la combinación de dos conjuntos AWG entrelazados. El campo emergente de cada uno de ellos interfiere a lo largo del chip de silicio de tal forma que el patrón de interferencia total revela la información espectral del haz incidente. Para ello el haz incidente es desfasado por cada guía de onda de tal forma que cada conjunto de guías genera un frente inclinado. Puesto que los dos conjuntos de guías de onda introducen inclinaciones opuestas, ambos haces forman un ángulo de interferencia en función de la longitud de onda, Ec. (7.2). El análisis del patrón de franjas periódicas a través de su espectro de Fourier permite detectar las diferentes longitudes de onda implicadas y sus respectivas potencias. El esquema propuesto puede entenderse como un dispositivo interferométrico dispersivo operando en transmisión, véase Fig. 7.2.

Dado que cada guía de onda propaga su modo fundamental (gaussiano), a la salida del conjunto de guías encontramos una superposición de modos que genera el haz. En función de la anchura de cada guía (por tanto del modo) y del desfase introducido entre guías adyacentes, el frente demuestra un comportamiento característico a lo largo de su propagación en el chip. La región de interferencia corresponde al dominio de campo cercano dónde los haces se propagan en el régimen de difracción de Fresnel. Por otro lado, el haz localizado inmediatamente después de cada AWG y antes de la región de interferencia, se puede expresar como una función periódica asociada a la estructura AWG. Esta función es modulada por un factor de fase lineal que da cuenta de la inclinación del haz, Ec. (7.3). Teniendo en cuenta todo esto el campo complejo W_p asociado a cada AWG_p ($p = 1, 2$) se puede determinar analíticamente, dentro de esta aproximación, según la expresión Ec. (7.5).

De este resultado se deriva un hecho interesante, y es que para un determinado rango de valores de la distancia de propagación z el frente presenta un efecto de autoimagen. Esto corresponde precisamente al efecto Talbot provocado por la estructura del AWG. Por tanto para la distancia Talbot z_T, dada en función de la longitud de onda y el periodo del AWG, el frente [Ec. (7.9)] adopta la forma correspondiente a la apertura del AWG. Concretamente, la distribución de intensidad del interferograma a la distancia z_T se expresa como Ec. (7.12). A partir de este patrón de interferencias se puede extraer a través del análisis de su espectro de Fourier el valor correspondiente a la longitud de onda. La figura 7.3 ilustra precisamente este hecho. Para ello se ha considerado el caso de un microespectrómetro con resolución espectral Rayleigh límite $\Delta\lambda = 0.1$ nm, y parámetros: 180 guías de onda por AWG, orden de interferencia $m = 40$, periodo $d = 4$ μm, anchura de modo fundamental de guía $w = 4.8$ μm. La

interpretación de Ec. (7.12) y de Fig. 7.3 es sencilla: en el espectro de Fourier del interferograma se localizan varios picos a diferentes frecuencias espaciales correspondientes a la frecuencia 2α del interferograma y de la frecuencia asociada a la estructura AWG. Para los parámetros anteriores esto implica un pico (a) localizado a 2α =30 líenas/mm que revela la existencia de la longitud de onda considerada, λ = 1502 nm, mientras que las asociadas a la estructura AWG aparecen a 250 líenas/mm (c) y 500 líenas/mm (f) acompañadas por las componentes asociadas a la frecuencia 2α: (b,d) y (e,g), respectivamente. Puesto que la resolución límite del fotodetector es aproximadamente 130 líneas/mm estas últimas componentes espectrales (b)−(g) son filtradas directamente. Es importante resaltar que los picos (b)−(g) no han interpretarse como componentes espúreas del interferograma.

La influencia del valor del periodo d del AWG se muestra en Fig. 7.4, para valores 3 μm, 4 μm, y 5 μm. Esto ilustra como la dispersión del dispositivo propuesto aumenta al reducir su periodo, tal y como sucede en un dispositivo AWG convencional.

La distribución de intensidad en la región de interferencia tanto en el chip (*combiner region*) como en el aire es mostrada en Fig. 7.5 para la longitud de onda Littrow λ_L = 1500 nm y máxima λ = 1508 nm. Esto permite visualizar el comportamiento de la propagación de los haces y su interferencia para diferentes distancias de propagación. Nótese que en Fig. 7.5(a) no existe un patrón de interferencia ya que para la longitud de onda Littrow el dispositivo no introduce desfase relativo alguno entre guías adyacentes. Sin embargo, se aprecia claramente la propagación característica en presencia del efecto Talbot, que en este caso puede entenderse como un patrón de Moiré originado por la superposición de ambos frentes. Por el contrario para el resto de longitudes de onda, a lo anterior hay que añadir la interferencia entre ambos haces tal y como se demuestra en Fig. 7.5(b) para λ = 1508 nm. Estos resultados se han obtenido a partir de la simulación numérica del dispositivo, la cuál corresponde al cálculo numérico de la integral de Fresnel. Para ello se ha empleado el mismo algoritmo mencionado en capítulos anteriores. El alto grado de acuerdo entre los resultados numéricos y teóricos es manifiesto.

Finalmente, se determina el espectro de Fourier asociado al interferograma obtenido para un haz incidente con longitudes de onda: 1502 nm, 1502.3 nm, 1504 nm, 1505 nm, 1506 nm y 1508 nm. En Fig. 7.6 se representa gráficamente este resultado. Mientras, en Fig. 7.7 se muestra el resultado de aplicar apodización gaussiana al campo. Tal y como se aprecia, el empleo de la apodización permite reducir el nivel de interferencia (*crosstalk*) de −20 dB a −40 dB. Para este caso la resolución espectral es $\Delta\lambda = 0.3$, lo que está en acuerdo con el criterio de resolución de Rayleigh.

Resultados similares se obtienen en los casos de distancias Talbot fraccionarias $z_T\eta/\zeta$, donde η y ζ son números enteros y $\eta < \zeta$. En estos casos también se puede determinar analíticamente la expresión del campo difractado, la cual está dada (para ζ par) por la expresión Ec. (7.10). Un resultado análogo se obtiene para ζ impar. Esta expresión permite encontrar la distribución del campo para la distancia $z_T/2$, Ec. (7.14), que da cuenta de la generación de autoimagen de la estructura AWG desplazada medio periodo ($d/2$). Por otro lado, la expresión Ec. (7.15) que corresponde al caso $z_T/4$ indica la existencia de un doblado de la frecuencia espacial tal y como se aprecia en el inset de Fig. 7.5(a). Estos fenómenos asociados al efecto Talbot son sobradamente conocidos, sin embargo en el contexto de este tipo dispositivos resultan ciertamente inéditos ya que habitualmente éstos se diseñan para que operen en el dominio de campo lejano o de Fraunhoffer.

El interferograma a esta distancia de propagación $z = z_T/4$ se puede calcular a partir de Ec. (7.10). Concretamente, está dado por la expresión Ec. (7.16). En el caso que nos ocupa, ésta puede simplificarse ya que la frecuencia espacial asociada al interferograma es menor que la asociada al AWG, $\alpha < 1/d$, obteniendo finalmente la expresión Ec. (7.17). Al igual que en los casos anteriores la información espectral puede extraerse a partir del espectro de Fourier, tal y como se ilustra en Fig. 7.8. Este resultado es completamente análogo al obtenido para las distancias z múltiplo de z_T salvo que para este caso el interferograma no contiene la frecuencia de 250 líneas/mm asociada a la estructura del AWG debido al término $\cos(d\pi\alpha)$ +

$\tan(2\pi\alpha x)\sin(d\pi\alpha)$, véase Fig. 7.8 (1502 nm). La aplicación de apodización gaussiana permite también una reducción considerable del *crosstalk* de -20 dB a -40 dB, Fig. 7.9.

Este análisis ha permitido lograr un diseño optimizado para este tipo de microespectrómetro a la vez que revela las propiedades y comportamiento que lo caracterizan. La implantación de este tipo de dispositivos ciertamente requiere un estudio más profundo en función de la aplicación considerada. Un hecho a tener en cuenta concierne a la integración de estos dispositivos con la tecnología de detección existente. Por ello es oportuno considerar cómo afecta el muestreo del interferograma en función de la resolución del fotodetector empleado. En nuestro caso consideramos un sensor CCD para el infrarrojo. Los periodos de muestreo estudiados y correspondientes a los píxeles del sensor son 4 μm, y 5 μm. Tal y como se demuestra en Fig. 7.10(a), no se aprecia problemas de muestreo (*aliasing*) para el valor de 4 μm (para este diseño) lo que resulta más que suficiente para la recuperación de la información espectral. Esto contrasta con el resultado obtenido para 5 μm, en el que se aprecia un aliasing que da lugar a información espectral espúrea Fig. 7.10(b). No obstante, la dispersión de este microespectrómetro puede controlarse gracias al orden de interferencia m y al periodo d del AWG. De esta manera se puede diseñar el dispositivo para lograr un interferograma que pueda ser suficientemente muestreado para cada tipo de sensor CCD disponible.

Conclusiones

Basándonos en el formalismo matricial, que describe a los sistemas ópticos de primer orden (paraxiales), hemos obtenido un diseño flexible capaz de realizar transformaciones ortosimplécticas en el espacio de fase. Este diseño está constituido por la combinación de lentes generalizadas (conjunto de lentes cilíndricas delgadas) e intervalos espaciales (propagación en el espacio libre). En concreto, esta configuración permite la implementación de las operaciones: rotación, transformada fraccionaria de Fourier (FRFT) separable y gyrator (GT). Demostramos que la operaciones FRFT y GT pueden ser realizadas empleando un sistema simétrico constituido por tres lentes generalizadas y dos intervalos. Mientras, la operación rotación corresponde a un sistema asimétrico que requiere cuatro lentes generalizadas e intervalos. Los parámetros de la transformación se alcanzan a través de la rotación de lentes cilíndricas (variación de la potencia de la lente generalizada) sin necesidad de ajustar la distancia existente entre ellas, y sin que el resultado final se vea afectado por factores extras de escala ni modulación de fase. Este es un resultado original y relevante de este trabajo.

La implementación óptica de estas transformaciones es analizada en detalle. En particular, la implementación experimental de la operación GT es demostrada en el caso de la transformación, a tiempo casi-real y de forma interactiva, de modos Hermite-Gaussian (HG) a Laguerre-Gaussian (LG). Los resultados experimentales obtenidos están en excelente acuerdo con las predicciones teóricas, demostrando la viabilidad del sistema propuesto. Así mismo, se estudia en detalle las principales propiedades de GT así como sus aplicaciones en procesado de imágenes, por primera vez. Esta transformación promete ser una herramienta útil en caracterización de haces, holografía, procesado de la información, computación cuántica, etc. Este trabajo tiene especial relevancia ya que la operación GT es muy poco conocida por la comunidad óptica.

La implementación experimental de la operación GT requiere el empleo de determinadas señales a procesar, modos HG. Esto ha requerido el desarrollo de un sistema que ofrezca alto rendimiento óptico a tiempo casi real. Dicho sistema está basado en dos moduladores espaciales de luz acoplados que implementan ópticamente una función compleja generada por ordenador. Los resultados obtenidos demuestran la generación modos HG así como la composición de modos estables con alta calidad óptica. Esta configuración ofrece importantes ventajas frente a otros sistemas basados en holografía digital, a saber: alto rendimiento óptico a tiempo real, alineamiento digital (no requiere posicionadores mecánicos), y versatilidad. Esta es la primera vez que este método es llevado a cabo, y resulta atractivo en numerosas tareas de procesado de información.

Finalmente, basándonos en el empleo de sistemas ópticos de primer orden, proponemos el diseño de un microespectrómetro de Fourier. Este dispositivo optoelectrónico opera en transmisión de tal forma que su configuración interferométrica, basada en la combinación de redes de guías de onda, permite extraer la información espectral de la luz que sobre él incide. Este estudio se realiza analíticamente dentro del formalismo de la difracción de la luz en campo próximo, cuyos resultados son confirmados por simulaciones numéricas. Esta es también la primera vez que se realiza tal estudio para este tipo de dispositivos. Los resultados obtenidos para un ancho de banda de 8 nm centrado en la longitud de onda $\lambda = 1500$ nm, con resolución Rayleigh $\Delta\lambda = 0.1$ nm, demuestran un alto grado de reducción de ruido (*crosstalk*) hasta -40 dB. El funcionamiento del dispositivo es ilustrado a través de diferentes ejemplos numéricos que demuestran su viabilidad.

Introduction

During the last decades, optics has been demonstrated to play an important role in different fields such as computing technology, data storage, communications, optoelectronics, information processing, etc. For example, in the area of communication (optical fiber, waveguides, etc.) and storage (CD, DVD, etc.), optical technologies have increasingly replaced some conventional electronical technologies. In general, optics is used together with electronics in a complementary manner. New optoelectronic developments are emerging in spectroscopy, optical interconnects, metrology, information processing, chemical and biological sensing, etc.

Optical information processing is an important and active field with many significant advances. The first optical system for information processing was introduced by Van der Lugt more than 30 years ago [1]. He proposed an optical correlator based on a thin lens to produce the two-dimensional Fourier transform (FT). This idea led to the creation of many optical and optoelectronic processors such as joint correlators, adaptive filters and optical differentiators, [2]. Other tools actively used in digital information processing such as wavelet transforms [3, 4] and bilinear distributions [5]−[11], have been also implemented in optics.

Nowadays, fractional transformations have a significant importance in information processing [12]−[20]. They offer a new degree of freedom (the fractional order) which can be very useful in many processing tasks. These kind of transformations naturally arise in different fields such as optics and quantum mechanics. For instance, the fractional Fourier transform (FRFT) is used for phase retrieval [21]−[31], signal characterization [32]−[38], space-variant filtering [39]−[58], encryption [59]−[66], watermarking [67, 68], creation of neural networks [69]−[74]. Other fractional transformations were found, for example Hilbert transform which is a promising tool for selective edge detection [75]−[78]. In addition, the fractional Hilbert and cosine transform as well as the FRFT have been also applied in digital holography for reconstructing in-line holograms [79]. We refer to reader to [80] where a review of the fractional transformations role in optical information processing is considered in detail.

Several well-known and important operations: scaling, quadratic phase modulation, and fractional transformations such as FRFT can be performed by simple optical configurations thanks to first-order optical systems. A first-order optical system is commonly constructed by thin lenses, mirrors, prisms separated by convenient free-space propagation intervals, etc. The list of operations significantly enlarged when cylindrical lenses are applied. Indeed, it allows to perform attractive operations as image rotation and nonsymmetric scaling, which lead to affine image transformation, and the separable FRFT. The combination of all these operations corresponds to linear canonical integral transformation (LCT). Other systems performing affine transformations in phase space such as the gyrator transform (GT), can be constructed by the combination of a separable FRFT system embedded in two rotator setups, [81]. Nevertheless, to the best of our knowledge no systematic study of the design of these optical systems has been realized.

In this work we analyze in detail the optical system design corresponding to these orthosymplectic transformations: rotator, separable FRFT, and GT operations. Our main goal is to find a flexible setup composed of generalized lenses (assembled set of thin cylindrical lenses) and fixed free-space intervals, where one or two-parametric transformation is reached only by

means of lens rotations. Such type of setups are demanded in different applications: beam characterization, Hermite-Gaussian to Laguerre-Gaussian mode conversion [82]−[99], phase retrieval, optical information processing, etc.

In contrast to the rotator operation and separable FRFT, the GT operation is still little-known for the optical community. This is the first time the GT optical implementation as well as its mains properties are studied. The GT action is also experimentally demonstrated for the case of stable mode generation. In fact, the GT can be considered as a generalized mode converter. Besides, we propose a number of applications of the GT application for image processing.

Other relevant applications of first-order optical systems are related to spectroscopy. In this work we propose an optimized design for a Fourier-transform microspectrometer based on two interleaved arrayed waveguide gratings (AWG) operating in transmission geometry. The retrieval of spectral information is reached by Fourier analysis of the interference pattern, which is generated by the light emerging from each AWG array. In contrast to conventional AWG devices where an image of the input waveguide is formed dispersively in the focal region, thus operating in Frauhoffer (far-field) diffraction regime, the considered device does not involve focusing and operates in Fresnel regime. Therefore, to solve the near-field diffraction problem is required. This is the first time it is addressed for an AWG device. The device design implies to analyze the spectral retrieval information in presence of the Talbot effect (self-imaging) associated to the AWG structure. The spectral retrieval information with a crosstalk level suppression of -40 dB is demonstrated for a bandwidth of 8 nm at 1500 nm.

This work is organized in seven chapters. In chapter 1 the first-order system fundamentals as well as the image rotation, separable FRFT and GT operation are introduced. Chapter 2 is devoted to the optical design for rotator, separable FRFT, and GT operations. In chapter 3 we discuss the optical implementation for rotator and separable FRFT. The GT operation is exhaustively studied trough chapters 4−6, where its main properties and applications as well as its experimental implementation are presented. Finally, the Fourier-transform AWG microspectrometer is studied in chapter 7.

Since we have developed programs for the numerical simulations of these systems, in appendix A the corresponding numerical approach is discussed. In appendix B we provide some of the intermediate calculations corresponding to the GT properties discussed in chapter 4. Finally, in appendix C we present a flexible setup based on two coupled SLMs that permits almost at real time the generation of complex optical fields. We have developed this setup for the implementation of input signals, which are used in the experimental realization of the GT operation. Several signal compositions generated by this setup are shown in detail, demonstrating its high optical throughout. We have developed a particular software for this application, which is presented in appendix C as well. The work ends with concluding remarks.

Contents

Chapter 1

Introduction to first-order optical systems

In this chapter we introduce the matrix formalism that describes the lossless first-order optical systems. This formalism offers an elegant way to find a flexible system design able to perform ortho-symplectic transformations such as image rotation, separable FRFT and GT. This flexible system design is based on two basic first-order system types; thin cylindrical lenses and free-space propagation intervals. Such basic systems as well as these ortho-symplectic transformations are also introduced.

1.1 Fundamentals and useful examples

First-order optical systems, also known as **ABCD** systems, consisting of thin lenses, mirrors, prisms, free-space propagation intervals, gradient index lenses [100], etc. have been exhaustively studied in the last decades. These paraxial systems are characterized by the well-known real 4×4 ray transformation matrix $\mathbf{T}$ [82, 83], which relates the position $\mathbf{r}_i$ and direction $\mathbf{q}_i$ of an incoming ray to the position $\mathbf{r}_o$ and direction $\mathbf{q}_o$ of the outgoing ray:

$$\begin{bmatrix} \mathbf{r}_o \\ \mathbf{q}_o \end{bmatrix} = \begin{bmatrix} \mathbf{A} & \mathbf{B} \\ \mathbf{C} & \mathbf{D} \end{bmatrix} \begin{bmatrix} \mathbf{r}_i \\ \mathbf{q}_i \end{bmatrix} = \mathbf{T} \begin{bmatrix} \mathbf{r}_i \\ \mathbf{q}_i \end{bmatrix}. \tag{1.1}$$

Notice that $\mathbf{r}^t = (x, y)$ and $\mathbf{q}^t = \left(q_x, q_y\right)$, where t stands for transposition operation and $q_{x,y}$ are the cosine directions of ray vector with the x and y axis. An example of ABCD system is displayed in Fig. 1.1. In this chapter as well as in the next one, we use dimensionless variables $\mathbf{r}_{i,o}/\sqrt{\lambda\varepsilon} \rightarrow \mathbf{r}_{i,o}$, $\mathbf{q}_{i,o}\sqrt{\varepsilon/\lambda} \rightarrow \mathbf{q}_{i,o}$, and the dimensionless submatrices $\mathbf{B}/\varepsilon \rightarrow \mathbf{B}$ and $\mathbf{C}\varepsilon \rightarrow \mathbf{C}$, where λ is the wavelength and ε corresponds to lengths such as propagation distance z, focal lens f, beam waist w, etc.

The ray transformation matrix parameterizes the kernel $K_{\mathbf{T}}$ of the operator $R^{\mathbf{T}}$ associated to LCT. The evolution of the complex field amplitude $f(\mathbf{r})$ during its propagation through the first-order optical system is described by the LCT. Indeed, the output complex field amplitude is written as it follows:

$$\begin{aligned} f_o(\mathbf{r}_o) &= R^{\mathbf{T}}[f_i(\mathbf{r}_i)](\mathbf{r}_o) = \int f_i(\mathbf{r}_i) K_{\mathbf{T}}\left(\mathbf{r}_i, \mathbf{r}_o\right) \, \mathrm{d}\mathbf{r}_i \\ &= \frac{1}{\sqrt{\det i\mathbf{B}}} \int f_i(\mathbf{r}_i) \exp\left(i\pi\left[\mathbf{r}_i^t \mathbf{B}^{-1} \mathbf{A} \mathbf{r}_i - 2\mathbf{r}_i^t \mathbf{B}^{-1} \mathbf{r}_o + \mathbf{r}_o^t \mathbf{D} \mathbf{B}^{-1} \mathbf{r}_o\right]\right) \mathrm{d}\mathbf{r}_i, \end{aligned} \tag{1.2}$$

for the nonsingular case ($\det \mathbf{B} \neq \mathbf{0}$), which corresponds to the Collins integral [101]. While in the singular case ($\mathbf{B} = \mathbf{0}$) the generalized imaging condition is obtained:

$$f_o(\mathbf{r}_o) = \frac{1}{\sqrt{|\det \mathbf{A}|}} f_i(\mathbf{A}^{-1}\mathbf{r}_o) \exp\left(i\pi\left[\mathbf{r}_o^t \mathbf{C}\mathbf{A}^{-1}\mathbf{r}_o\right]\right). \tag{1.3}$$

The transformation matrix $\mathbf{T}$ is symplectic:

$$\mathbf{T}^t\mathbf{Q}\mathbf{T} = \mathbf{Q}, \tag{1.4}$$

where

$$\mathbf{Q} = \begin{bmatrix} \mathbf{0} & \mathbf{I} \\ -\mathbf{I} & \mathbf{0} \end{bmatrix}, \tag{1.5}$$

is the skew-symmetric matrix with a unity 2×2 submatrix $\mathbf{I}$. Note that $\mathbf{T}^t$ denotes the transposition operation of $\mathbf{T}$. Because of the symplecticity condition,

$$\begin{array}{lll} \mathbf{A}\mathbf{B}^t = \mathbf{B}\mathbf{A}^t, & \mathbf{C}\mathbf{D}^t = \mathbf{D}\mathbf{C}^t, & \mathbf{A}\mathbf{D}^t - \mathbf{B}\mathbf{C}^t = \mathbf{I}, \\ \mathbf{A}^t\mathbf{C} = \mathbf{C}^t\mathbf{A}, & \mathbf{B}^t\mathbf{D} = \mathbf{D}^t\mathbf{B}, & \mathbf{A}^t\mathbf{D} - \mathbf{C}^t\mathbf{B} = \mathbf{I}, \end{array} \tag{1.6}$$

the 4×4 ray transformation matrix is described by only ten free parameters. Below we reserve capital bold letters $\mathbf{T}$, $\mathbf{Q}$, $\mathbf{M}$ and $\mathbf{R}$ to indicate the 4×4 ray transformation matrix; other bold capital letters correspond to the 2×2 submatrices, which compose the entire 4×4 matrix.

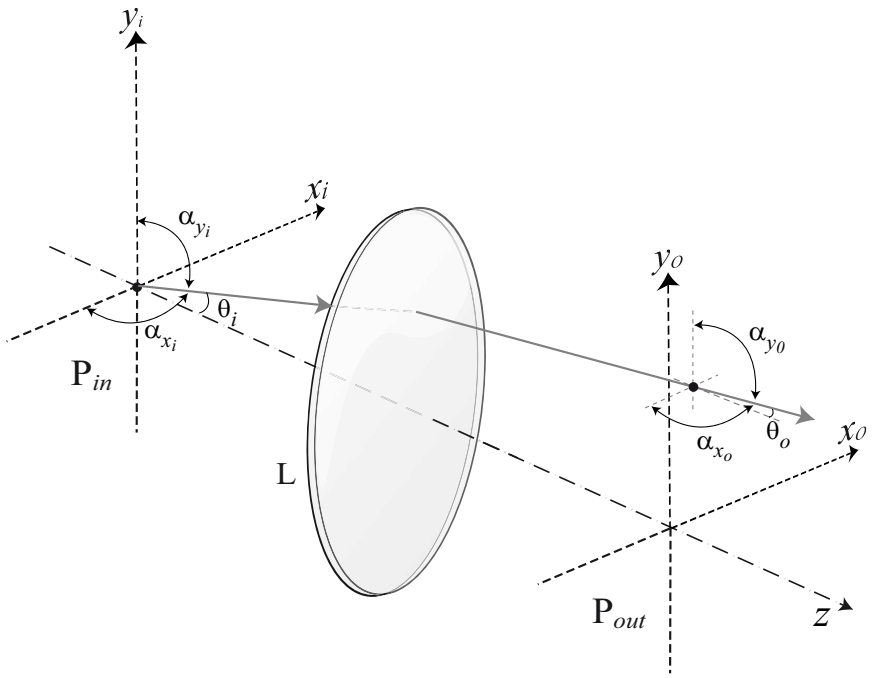

Figure 1.1: ABCD system composed by two free-space intervals and one thin lens L (without aberrations). P_{in} and P_{out} are the input and output planes, respectively. Note that cosine directions are given by $\cos\alpha_{x,y} = q_{x,y}$ with $\theta^2 = q_x^2 + q_y^2$.

Taking into account the modified Iwasawa decomposition, any ray transformation matrix $\mathbf{T}$ [83, 84] can be written as a product of an anamorphic (nonsymmetric) lens, an anamorphic

magnifier (scaling), and an ortho-symplectic system:

$$\mathbf{T} = \begin{bmatrix} \mathbf{A} & \mathbf{B} \\ \mathbf{C} & \mathbf{D} \end{bmatrix} = \begin{bmatrix} \mathbf{I} & \mathbf{0} \\ \mathbf{L} & \mathbf{I} \end{bmatrix} \begin{bmatrix} \mathbf{S} & \mathbf{0} \\ \mathbf{0} & \mathbf{S}^{-1} \end{bmatrix} \begin{bmatrix} \mathbf{X} & \mathbf{Y} \\ -\mathbf{Y} & \mathbf{X} \end{bmatrix}, \tag{1.7}$$

where

$$\begin{aligned} \mathbf{S} &= (\mathbf{A}\mathbf{A}^t + \mathbf{B}\mathbf{B}^t)^{1/2} = \mathbf{S}^t, \\ \mathbf{X} + i\mathbf{Y} &= (\mathbf{A}\mathbf{A}^t + \mathbf{B}\mathbf{B}^t)^{-1/2} (\mathbf{A} + i\mathbf{B}), \\ \mathbf{L} &= \left(\mathbf{C}\mathbf{A}^t + \mathbf{D}\mathbf{B}^t\right) (\mathbf{A}\mathbf{A}^t + \mathbf{B}\mathbf{B}^t)^{-1} = \mathbf{L}^t. \end{aligned} \tag{1.8}$$

The first matrix in the decomposition performs an anamorphic quadratic phase modulation. The scaling operation, described by the second matrix, is also well studied [83, 85]. The last ortho-symplectic matrix, orthogonal ($\mathbf{M}^t = \mathbf{M}^{-1}$) and symplectic, is a general expression for a variety of attractive transforms such as image rotation and FRFT [83, 84, 86]. In the case of ortho-symplectic matrices the conditions given by Eqs. (1.6) reduce to [83]:

$$\mathbf{X}\mathbf{Y}^t = \mathbf{Y}\mathbf{X}^t, \quad \mathbf{X}^t\mathbf{Y} = \mathbf{Y}^t\mathbf{X}, \quad \mathbf{X}\mathbf{X}^t + \mathbf{Y}\mathbf{Y}^t = \mathbf{I}. \tag{1.9}$$

Moreover, the ortho-symplectic systems can be also elegantly described by the unitary matrix $\mathbf{U} = \mathbf{X} + i\mathbf{Y}$, [84].

Sophisticated first-order optical systems can be designed thanks to the cascade of basic ones such as thin lenses and free-space propagation intervals. Our main goal is to find a minimal lens−free-space flexible system design to perform attractive ortho-symplectic operations for optical information processing, in particular: image rotation, separable FRFT, GT, etc. Here we introduce these ortho-symplectic transformations.

Because we are interested on a lens−free-space system design, let us first remind these two basic first-order systems. A free-space light propagation interval z, is described by the submatrices: $\mathbf{A} = \mathbf{D} = \mathbf{I}$, $\mathbf{C} = \mathbf{0}$, and $\mathbf{B} = z\mathbf{I}$ that lead to the well-known Fresnel integral [102]:

$$f_o(\mathbf{r}_o) = \frac{\exp(i2\pi z/\lambda)}{i\lambda z} \iint f_i(\mathbf{r}_i) \exp\left(-i\pi \left[(x_o - x_i)^2 + (y_o - y_i)^2\right]/\lambda z\right) \mathrm{d}\mathbf{r}_i. \tag{1.10}$$

Meanwhile, a thin spherical lens [102] is described by submatrices: $\mathbf{A} = \mathbf{D} = \mathbf{I}$, $\mathbf{C} = -p\mathbf{I}$, and $\mathbf{B} = \mathbf{0}$. Therefore the output complex field amplitude just after this lens is given by:

$$f_o(\mathbf{r}_o) = f_i(\mathbf{r}_o) \exp\left(-i\pi p \left[x_o^2 + y_o^2\right]/\lambda\right), \tag{1.11}$$

where the lens power $p > 0$ and $p < 0$ correspond to a convergent and divergent lens, respectively.

The composition of both systems leads to basic optical transformations such as FT used for filtering, correlation, etc. The list of transformations enlarges when anamorphic lenses are considered. An example of anamorphic lens corresponds to the composition of two cylindrical lenses crossed at angle $\pi/2$, leading to a phase modulation function:

$$\Psi(\mathbf{r}) = \exp\left(-i\pi p_x x^2/\lambda\right) \exp\left(-i\pi p_y y^2/\lambda\right), \tag{1.12}$$

where $p_{x,y}$ are the lens powers for the x and y axis. Note that a spherical lens is recovered for $p_x = p_y$. Interesting and useful anamorphic lenses can be constructed by means of an assembled set of rotated cylindrical lenses, which we refer further to as a generalized lens. Several flexible schemes based on two or more cylindrical and spherical lenses to modulate the phase, have been proposed [87, 92]. The composition of generalized lenses together with free-space intervals will be used in chapter 2 for the design of ortho-symplectic optical systems.

1.1.1 Ortho-symplectic systems

Image rotation operation

The following submatrices

$$\mathbf{X}_{rot} = \begin{bmatrix} \cos\vartheta & \sin\vartheta \\ -\sin\vartheta & \cos\vartheta \end{bmatrix}, \quad \mathbf{Y}_{rot} = \mathbf{0}, \tag{1.13}$$

describe an image rotator operation [83, 86, 91], related to the rotation in position and spatial-frequency planes (x, y) and (q_x, q_y). It implies that the input complex field $f_i(\mathbf{r}_i)$ is rotated at angle ϑ:

$$f_o(\mathbf{r}_o) = f_i(x_o \cos\vartheta - y_o \sin\vartheta,\ y_o \cos\vartheta + x_o \sin\vartheta). \tag{1.14}$$

Several schemes for image rotation by lens setups have been proposed [83, 85, 86, 91]. Some of them do not relate to pure rotation since they introduce an additional phase modulation of the rotated image. We will call them imperfect rotators. Besides, it is also remarkable to mention that the rotator operation can be implemented by a lens-less setup, for instance by means of a pair of Dove prisms.

Separable fractional FT

The FRFT plays an important role in digital and optical information processing. It was studied by Kober [14] in 1939 and then used as a mathematical tool in quantum mechanics by Namias in 1980 [15]. In 1993, Mendlovic and Ozaktas studied the FRFT optically when they analyzed gradient index (GRIN) fiber [89]. In the same year, Lohmann proposed that FRFT could be realized by using conventional lens system [90]. A general treatment of optical systems performing the FRFT was realized by Sahin et al. in 1998 [95], in which the fractional orders can be specified independently. We refer to the reader to [12, 13], where the FRFT properties such as scaling, shift, Parseval theorem, etc. and its main applications are studied in detail.

The ray transformation submatrices associated to FRFT are given by [83, 84, 86, 93, 94, 95]:

$$\mathbf{X}_{\text{FRFT}} = \begin{bmatrix} \cos\gamma_x & 0 \\ 0 & \cos\gamma_y \end{bmatrix}, \quad \mathbf{Y}_{\text{FRFT}} = \begin{bmatrix} \sin\gamma_x & 0 \\ 0 & \sin\gamma_y \end{bmatrix}, \tag{1.15}$$

which produces rotations at planes (x, q_x) and (y, q_y) of the phase space. The transformation is separable and hence it can be written as $f_o(\mathbf{r}_o) = R^{\gamma_x} R^{\gamma_y}[f_i(\mathbf{r}_i)](\mathbf{r}_o)$, where

$$\begin{aligned} &R^{\gamma_x}[f_i(\mathbf{r}_i)](\mathbf{r}_o) \\ &= \frac{\exp(i\gamma_x/2)}{\sqrt{i\sin\gamma_x}} \int f_i(x_i, y_i)\, \exp\left(i\pi\left[(x_o^2 + x_i^2)\cot\gamma_x - 2x_i x_o \csc\gamma_x\right]\right) \mathrm{d}x_i, \end{aligned} \tag{1.16}$$

with $R^{\gamma_x} R^{\gamma_y} = R^{\gamma_x, \gamma_y}$. For angles $\gamma_x = \gamma_y = 0$ it corresponds to the identity transformation, whereas for $\gamma_x = 0$ and $\gamma_y = \pi$ the FRFT reduces to image reflection. Meanwhile for $\gamma_x = \gamma_y = \pi/2$ the Fourier transform is obtained. The case $\gamma_x = \gamma_y = \gamma$ and $\gamma_x = -\gamma_y = \gamma$ corresponds to the symmetric and antisymmetric FRFT, respectively. It is usual to define the transformation angle as $\gamma = n\pi/2$, where n is called fractional order or degree. For instance, the order $n = 4$ leads to the self-imaging case meanwhile $n = -1$ corresponds to the inverse Fourier transform.

As it is known, the symmetric FRFT arises naturally in optical systems. Indeed, the composition of a spherical lens with focal distance f and two free-space intervals with distance z leads to a symmetric FRFT system [12], Fig. 1.2, which is parameterized by

$$\begin{aligned} z &= s^2 (\csc\gamma - \cot\gamma)/\lambda, \\ f &= \left(s^2 \csc\gamma\right)/\lambda. \end{aligned}$$

Therefore, the transformation angle γ is changed by adjusting the distance z. Nevertheless, the output complex field is affected by an additional scaling (s) that depends on the transformation angle. This system corresponds to the well-known Lohmann FRFT type system [90]. Note that for $z = f$ the FT is obtained.

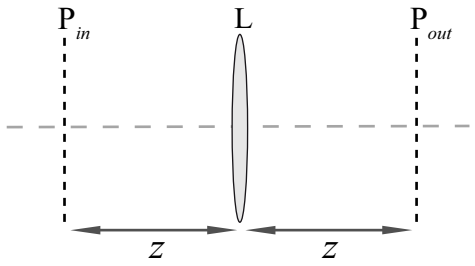

Figure 1.2: Symmetric FRFT optical setup corresponding to the Lohmann system type. The transformation angle is changed by adjusting the free-space intervals z. L is a convergent spherical thin lens meanwhile P_{in} and P_{out} are the input and output planes, respectively.

As mentioned, Sahin et al. [95] introduced a general treatment of FRFT optical systems. They derived several optical designs for the FRFT where input and output scale parameters as well as the residual spherical phase factors can be controlled. In contrast to the Lohmann type system, these systems use cylindrical lenses. However, all these systems are not flexible since for any transformation angle value the distances among lens and input−output planes as well as the lens powers have to be changed. Other FRFT systems constructed by using spherical mirrors instead thin lenses have been proposed [103, 104, 105].

Recently, an optical system based on two generalized lenses [92] to perform a FRFT has been proposed [97]. This configuration permits one to change the fractional angles by a corresponding rotation of the lenses, but the resulting FRFT has a scaling depending on the angle values. In chapter 2 we derive a flexible design for the FRFT based on three generalized lenses and two free-space intervals that permits to change the transformation angles by the proper lens rotation without depending scaling and additional phase modulation.

Gyrator transform

Another attractive and useful operation is the gyrator transform, associated with the submatrices

$$\mathbf{X}_{gyr} = \begin{bmatrix} \cos\alpha & 0 \\ 0 & \cos\alpha \end{bmatrix}, \quad \mathbf{Y}_{gyr} = \begin{bmatrix} 0 & \sin\alpha \\ \sin\alpha & 0 \end{bmatrix}, \tag{1.17}$$

that describes the rotation at the twisted position and spatial-frequency planes (x, q_y) and (y, q_x) [83, 84, 86]. Thus the GT is defined as

$$\begin{aligned} f_o(\mathbf{r}_o) &= R^{\alpha}[f_i(\mathbf{r}_i)](\mathbf{r}_o) \\ &= \frac{1}{|\sin\alpha|}\iint f_i(x_i, y_i)\, \exp\left(i2\pi\frac{(x_o y_o + x_i y_i)\cos\alpha - (x_i y_o + x_o y_i)}{\sin\alpha}\right) \mathrm{d}x_i \mathrm{d}y_i. \end{aligned} \tag{1.18}$$

While the kernel of the FRFT is given as a product of plane and elliptic waves, the GT kernel is given as a product of plane and hyperbolic waves. It is known that the gyrator operation is responsible for the Hermite-Gaussian to Laguerre-Gaussian mode conversion [83]−[86], which will be further studied in chapter 4, 5 and 6. In this work we study the GT optical implementation as well as its main properties for first time.

Arbitrary ortho-symplectic systems

For the case of the separable FRFT, image rotation operation, and GT the unitary matrix is written as

$$\mathbf{U}_{\mathrm{FRFT}}\left(\gamma_x,\gamma_y\right)=\begin{bmatrix}\exp(i\gamma_x) & 0\\ 0 & \exp(i\gamma_y)\end{bmatrix}, \tag{1.19}$$

$$\mathbf{U}_{rot}\left(\vartheta\right)=\begin{bmatrix}\cos\vartheta & \sin\vartheta\\ -\sin\vartheta & \cos\vartheta\end{bmatrix}, \tag{1.20}$$

$$\mathbf{U}_{gyr}\left(\theta\right)=\begin{bmatrix}\cos\alpha & i\sin\alpha\\ i\sin\alpha & \cos\alpha\end{bmatrix}, \tag{1.21}$$

respectively. As it was shown in [81] any ortho-symplectic system can be constructed from a FRFT system embedded in two rotator systems.

Therefore, the unitary matrix $\mathbf{U}$ for any ortho-symplectic system is written as

$$\mathbf{U}=\mathbf{U}_{rot}\left(\beta\right)\mathbf{U}_{\mathrm{FRFT}}\left(\gamma_x,\gamma_y\right)\mathbf{U}_{rot}\left(\alpha\right). \tag{1.22}$$

It is an important result since it also allows the numerical calculation of LCTs by using conventional algorithms developed for the FRFT. Notice that rotator operation produces the rotation both for the spatial variables (x,y) and the spatial-frequency variables (q_x,q_y), whereas FRFT produces a rotation through γ_x and γ_y for the space−spatial-frequency (x,q_x) and (y,q_y), correspondingly. In particular the GT can be represented as a combination of the rotator and FRFT (see reference [106]):

$$\mathbf{U}_{gyr}\left(\alpha\right)=\mathbf{U}_{rot}\left(-\pi/4\right)\mathbf{U}_{\mathrm{FRFT}}\left(\alpha,-\alpha\right)\mathbf{U}_{rot}\left(\pi/4\right). \tag{1.23}$$

In addition, thanks to the modified Iwasawa decomposition [Eq. (1.7)] an entire optical system is represented by the combination of an anamorphic lens (with matrix $\mathbf{L}$), an anamorphic magnifier (with matrix $\mathbf{S}$), and an ortho-symplectic system:

$$\mathbf{T}=\mathbf{T}_{\mathbf{L}}\mathbf{T}_{\mathbf{S}}\mathbf{T}_{rot}\left(\beta\right)\mathbf{T}_{\mathrm{FRFT}}\left(\gamma_x,\gamma_y\right)\mathbf{T}_{rot}\left(\alpha\right), \tag{1.24}$$

that brings us to a general representation of the LCT for any transformation matrix ($\mathbf{T}$), with or without a singularity of the submatrix $\mathbf{B}$.

Chapter 2

Optical system design for ortho-symplectic transformations in phase space

One of the objectives of this work is to design a flexible system for the optical implementation of attractive transformations such as image rotation, separable FRFT and gyrator transform, which are associated to ortho-symplectic matrices. This system design corresponds to a cascade of generalized lenses (assembled set of cylindrical lenses) and fixed free-space intervals. The system is flexible since the change of the transformation parameter is almost in real time achieved by the proper rotation of the cylindrical lenses or lens power variation.

In chapter 1 we have introduced the matrix formalism as well as image rotation, separable FRFT, and GT operations. In this chapter we analyze these paraxial systems, on the basis of a matrix formalism. Section 2.1 is devoted to analysis of the transformation matrix associated to a general system composed of n generalized lenses and $n+1$ free-space intervals. In Section 2.2 symmetric systems are studied in detail, which lead to obtain a flexible setup design for the separable FRFT and GT. The optical implementation of their corresponding generalized lenses is also analyzed in Section 2.3. Finally, we demonstrate that the optical setup for the image rotation operation corresponds to a nonsymmetric flexible system, Section 2.4.

2.1 System design fundamentals

The basic elements for the design of a given first-order optical system, characterized by a ray transformation matrix $\mathbf{T}$, are generalized lenses and free-space intervals. Our first step is to find the general expression that relates the submatrices of the transformation matrix associated to this system.

A generalized lens [see the first matrix in Eq. (1.7)] is a superposition of m cylindrical ones, which is represented by a submatrix [87, 92]:

$$\mathbf{L} = -\frac{1}{2}\begin{bmatrix} \sum_{i=1}^{m} p_i(1+\cos 2\varphi_i) & \sum_{i=1}^{m} p_i \sin 2\varphi_i \\ \sum_{i=1}^{m} p_i \sin 2\varphi_i & \sum_{i=1}^{m} p_i(1-\cos 2\varphi_i) \end{bmatrix}, \tag{2.1}$$

where p_i is the power (in dimensionless variables $p_i\lambda \to p_i$) and φ_i is a rotation angle among the OY axis and the principal direction of the cylindrical $i-$th lens. Note that $\mathbf{L} = \mathbf{L}^t$. Note that $p_i < 0$ and $p_i > 0$ correspond to a divergent and convergent lens, respectively. These lenses can be constructed by assembling several cylindrical, which can be also implemented using holographic multiplexing, or by means of a SLM [96].

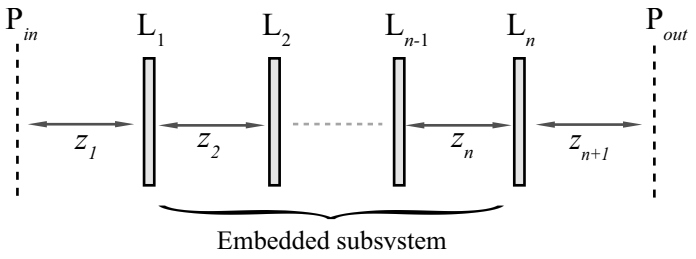

Figure 2.1: Optical setup scheme. P_{in} and P_{out} are the input and output planes, respectively. Generalized lenses $\mathbf{L}_m$ and free-space intervals z_m are displayed.

The entire system (see Fig. 2.1) contains n lenses with $n+1$ free-space intervals of length z_i ($z_i/\lambda \to z_i$) between themselves and the input−output planes. Therefore, its transformation matrix is given by

$$\mathbf{T}_n = \begin{bmatrix} \mathbf{A}_n & \mathbf{B}_n \\ \mathbf{C}_n & \mathbf{D}_n \end{bmatrix} = \begin{bmatrix} \mathbf{I} & z_{n+1}\mathbf{I} \\ \mathbf{0} & \mathbf{I} \end{bmatrix} \begin{bmatrix} \mathbf{I} & \mathbf{0} \\ \mathbf{L}_n & \mathbf{I} \end{bmatrix} \begin{bmatrix} \mathbf{I} & z_n\mathbf{I} \\ \mathbf{0} & \mathbf{I} \end{bmatrix} \cdots \begin{bmatrix} \mathbf{I} & \mathbf{0} \\ \mathbf{L}_1 & \mathbf{I} \end{bmatrix} \begin{bmatrix} \mathbf{I} & z_1\mathbf{I} \\ \mathbf{0} & \mathbf{I} \end{bmatrix}. \tag{2.2}$$

In particular, the expression for the system containing one lens $\mathbf{L}_1$is given by the transformation matrix

$$\begin{bmatrix} \mathbf{A}_1 & \mathbf{B}_1 \\ \mathbf{C}_1 & \mathbf{D}_1 \end{bmatrix} = \begin{bmatrix} \mathbf{I} & z_2\mathbf{I} \\ \mathbf{0} & \mathbf{I} \end{bmatrix} \begin{bmatrix} \mathbf{I} & \mathbf{0} \\ \mathbf{L}_1 & \mathbf{I} \end{bmatrix} \begin{bmatrix} \mathbf{I} & z_1\mathbf{I} \\ \mathbf{0} & \mathbf{I} \end{bmatrix} = \begin{bmatrix} \mathbf{L}_1 z_2 + \mathbf{I} & \mathbf{L}_1 z_1 z_2 + \mathbf{I}(z_1 + z_2) \\ \mathbf{L}_1 & \mathbf{L}_1 z_1 + \mathbf{I} \end{bmatrix}, \tag{2.3}$$

and establish the following relation among the submatrices $\mathbf{A}_1$, $\mathbf{B}_1$, $\mathbf{C}_1$, and $\mathbf{D}_1$:

$$\mathbf{B}_1 = \mathbf{A}_1 z_1 - \mathbf{C}_1 z_1 z_2 + \mathbf{D}_1 z_2. \tag{2.4}$$

In the same way a similar expression can be obtained for the systems with zero (free-space interval only), two, three and four lenses. The corresponding equations are summarized as

$$\begin{aligned}
\mathbf{B}_0 &= \mathbf{A}_0 z_1 \\
\mathbf{B}_1 &= \mathbf{A}_1 z_1 - \mathbf{C}_1 z_1 z_2 + \mathbf{D}_1 z_2, \\
\mathbf{B}_2 &= \mathbf{A}_2 z_1 - \mathbf{C}_2 z_1 z_3 + \mathbf{D}_2 z_3 + \mathbf{I} z_2, \\
\mathbf{B}_3 &= \mathbf{A}_3 z_1 - \mathbf{C}_3 z_1 z_4 + \mathbf{D}_3 z_4 + \mathbf{L}_2 z_2 z_3 + \mathbf{I}(z_2 + z_3), \\
\mathbf{B}_4 &= \mathbf{A}_4 z_1 - \mathbf{C}_4 z_1 z_5 + \mathbf{D}_4 z_5 + \mathbf{L}_2 z_2 (z_3 + z_4) + \mathbf{L}_3 z_4 (z_2 + z_3) + \mathbf{L}_3 \mathbf{L}_2 z_2 z_3 z_4 \\
&\quad + \mathbf{I}(z_2 + z_3 + z_4).
\end{aligned} \tag{2.5}$$

We observe that the submatrix $\mathbf{B}$ is a sum of submatrix $\mathbf{A}$ multiplied by the distance of the first free-space interval, submatrix $\mathbf{D}$ multiplied by the distance of the last free-space interval, submatrix $\mathbf{C}$ with opposite sign multiplied by the distance of the first and the last free-space intervals, and a term related only to the subsystem embedded between the first and the last lenses excluding them (see Fig. 2.1). Analyzing Eqs. (2.5) we have found that this additional term corresponds to the submatrix $\mathbf{B}$ of the embedded system. Then the general expression that relates the submatrices of the matrix $\mathbf{T}_n$ ($n \geq 2$) can be formulated as

$$\mathbf{B}_n = \mathbf{A}_n z_1 - \mathbf{C}_n z_1 z_{n+1} + \mathbf{D}_n z_{n+1} + \mathbf{B}^e_{n-2}, \tag{2.6}$$

where the submatrix $\mathbf{B}^e_{n-2}$ is related to the embedded subsystem, which contains $n-2$ lenses and $n-1$ free-space intervals.

It is an important result since the expression Eq. (2.6) significantly simplifies the system design as it will be demonstrated in the next section.

2.2 Symmetric systems

2.2.1 Transformation matrix and its submatrices relations

Regarding the one-dimensional case, it can be shown that there is only one ortho-symplectic matrix that corresponds to the one-dimensional FRFT [83]. The known optical systems implementing a one-dimensional FRFT and a two-dimensional fractional FT for the same angle in both orthogonal directions are symmetric, [90]. Since we are interested in symmetric systems performing ortho-symplectic transformations we first analyze their ray transformation matrix.

We underline that a symmetric system implies that $z_{n+2-k} = z_k$ and $\mathbf{L}_{n+1-k} = \mathbf{L}_k$ for $k = 1, ..., n/2$. In the case of odd n, the central lens can be represented as a cascade of two identical ones. For example, symmetric systems with one lens $\mathbf{L}$ can be represented by the matrix $\mathbf{T} = \mathbf{M}_z\mathbf{M}_L\mathbf{M}_z = \mathbf{M}_z\mathbf{M}_{L/2}\mathbf{M}_{L/2}\mathbf{M}_z$. Correspondingly, the symmetric system with two lenses can be described by $\mathbf{T} = \mathbf{M}_{z_1}\mathbf{M}_{L_1}\mathbf{M}_{z_2}\mathbf{M}_{L_1}\mathbf{M}_{z_1} = \mathbf{M}_{z_1}\mathbf{M}_{L_1}\mathbf{M}_{z_2/2}\mathbf{M}_{z_2/2}\mathbf{M}_{L_1}\mathbf{M}_{z_1}$. In general the symmetric system of n lenses can be represented by the following transformation matrix:

$$\mathbf{T} = \widetilde{\mathbf{M}}_1\widetilde{\mathbf{M}}_2...\widetilde{\mathbf{M}}_m\mathbf{M}_m...\mathbf{M}_2\mathbf{M}_1 = \widetilde{\mathbf{R}}\mathbf{R}, \tag{2.7}$$

where $\mathbf{M}_k = \mathbf{M}_{L_k}\mathbf{M}_{z_k}$, $\widetilde{\mathbf{M}}_k = \mathbf{M}_{z_k}\mathbf{M}_{L_k}$, $m = n/2$ if n is an even number and $m = (n+1)/2$ if n is an odd number. In the case of odd n, the matrix $\mathbf{M}_m$ is composed by the lens $\mathbf{L}_{(n+1)/2}$ with half of the focal distance. Note that if

$$\mathbf{M}_k = \mathbf{M}_{L_k}\mathbf{M}_{z_k} = \begin{bmatrix} \mathbf{a} & \mathbf{b} \\ \mathbf{c} & \mathbf{d} \end{bmatrix} = \begin{bmatrix} \mathbf{I} & z_k\mathbf{I} \\ \mathbf{L}_k & z_k\mathbf{L}_k + \mathbf{I} \end{bmatrix}, \tag{2.8}$$

then

$$\widetilde{\mathbf{M}}_k = \mathbf{M}_{z_k}\mathbf{M}_{L_k} = \begin{bmatrix} \mathbf{d} & \mathbf{b} \\ \mathbf{c} & \mathbf{a} \end{bmatrix} = \begin{bmatrix} z_k\mathbf{L}_k + \mathbf{I} & z_k\mathbf{I} \\ \mathbf{L}_k & \mathbf{I} \end{bmatrix}, \tag{2.9}$$

and

$$\widetilde{\mathbf{M}}_k^{-1} = \begin{bmatrix} \mathbf{d} & \mathbf{b} \\ \mathbf{c} & \mathbf{a} \end{bmatrix}^{-1} = \begin{bmatrix} \mathbf{a}^t & -\mathbf{b}^t \\ -\mathbf{c}^t & \mathbf{d}^t \end{bmatrix} = \begin{bmatrix} \mathbf{a} & -\mathbf{b} \\ -\mathbf{c} & \mathbf{d} \end{bmatrix} = \begin{bmatrix} \mathbf{I} & -z_k\mathbf{I} \\ -\mathbf{L}_k & z_k\mathbf{L}_k + \mathbf{I} \end{bmatrix}. \tag{2.10}$$

We observe that $\widetilde{\mathbf{M}}_k^{-1}(\mathbf{L}_k, z_k) = \mathbf{M}_k(-\mathbf{L}_k, -z_k)$. Note that $\mathbf{a}$, $\mathbf{b}$, $\mathbf{c}$ and $\mathbf{d}$ are 2×2 submatrices. This result is also valid for a subsystem constructed by a single thin lens or by a free-space interval. It is easy to see that if the transformation matrix of the subsystem is

$$\mathbf{R} = \begin{bmatrix} \mathbf{A}_r & \mathbf{B}_r \\ \mathbf{C}_r & \mathbf{D}_r \end{bmatrix}, \tag{2.11}$$

then

$$\widetilde{\mathbf{R}} = \begin{bmatrix} \mathbf{D}_r^t & \mathbf{B}_r^t \\ \mathbf{C}_r^t & \mathbf{A}_r^t \end{bmatrix}. \tag{2.12}$$

These expressions allow us to obtain the transformation matrix for a symmetric system:

$$\mathbf{T} = \widetilde{\mathbf{R}}\mathbf{R} = \begin{bmatrix} \mathbf{D}_r^t\mathbf{A}_r + \mathbf{B}_r^t\mathbf{C}_r & \mathbf{D}_r^t\mathbf{B}_r + \mathbf{B}_r^t\mathbf{D}_r \\ \mathbf{C}_r^t\mathbf{A}_r + \mathbf{A}_r^t\mathbf{C}_r & \mathbf{C}_r^t\mathbf{B}_r + \mathbf{A}_r^t\mathbf{D}_r \end{bmatrix}, \tag{2.13}$$

that implies $\mathbf{A} = \mathbf{D}^t$, $\mathbf{B} = \mathbf{B}^t$ and $\mathbf{C} = \mathbf{C}^t$, which is a basis for our further analysis. Taking into account the symplecticity conditions Eq. (1.6) for the matrix $\mathbf{R}$, the latter expression is simplified as following:

$$\mathbf{T} = \begin{bmatrix} \mathbf{A} & \mathbf{B} \\ \mathbf{C} & \mathbf{D} \end{bmatrix} = \begin{bmatrix} \mathbf{D}_r^t\mathbf{A}_r + \mathbf{B}_r^t\mathbf{C}_r & 2\mathbf{D}_r^t\mathbf{B}_r \\ 2\mathbf{C}_r^t\mathbf{A}_r & (\mathbf{D}_r^t\mathbf{A}_r + \mathbf{B}_r^t\mathbf{C}_r)^t \end{bmatrix}. \tag{2.14}$$

Comparing the latter conditions [Eq. (2.14)] with the ortho-symplectic matrix form ($\mathbf{A} = \mathbf{D}$ and $\mathbf{B} = -\mathbf{C}$), we conclude that an ortho-symplectic system can be implemented by a symmetric system only if its submatrices $\mathbf{X}$ and $\mathbf{Y}$ are equal to its transpose:

$$\mathbf{X} = \mathbf{X}^t, \quad \mathbf{Y}=\mathbf{Y}^t. \tag{2.15}$$

This is a relevant result that also allows us to conclude that an image rotation cannot be performed by a symmetrical system (except for the rotation at π) since in this case $\mathbf{X} \neq \mathbf{X}^t$ as can be seen from Eqs. (1.13).

If an ortho-symplectic matrix satisfies Eqs. (2.15) then according to Eq. (1.9) we obtain the following restrictions

$$\mathbf{XY} = \mathbf{YX}, \quad \mathbf{X}^2 + \mathbf{Y}^2 = \mathbf{I}. \tag{2.16}$$

Note that this relations hold for the separable FRFT and the gyrator matrices [see Eqs. (1.15) and (1.17)]. Based on the expressions Eqs. (1.6) and (2.14) we derive that

$$\begin{aligned} \mathbf{X} &= 2\mathbf{D}_r^t\mathbf{A}_r - \mathbf{I}, \\ \mathbf{Y} &= 2\mathbf{D}_r^t\mathbf{B}_r = -2\mathbf{C}_r^t\mathbf{A}_r. \end{aligned} \tag{2.17}$$

Therefore, it means that the following relation :

$$\mathbf{D}_r^t\mathbf{B}_r + \mathbf{C}_r^t\mathbf{A}_r = \mathbf{0}, \tag{2.18}$$

has to be satisfied in order to construct a symmetric ortho-symplectic system.

2.2.2 System design for the separable FRFT and GT

The previous results permit us start with the symmetric optical system design associated to separable FRFT and GT operation implementation. As mentioned in the previous chapter, there are two well-known symmetric optical configurations containing one or two lenses correspondingly, which perform the FRFT for the same angle in both orthogonal directions [89, 90]. Several other schemes to perform separable FRFT have been proposed [93, 94, 95]. However, they are not flexible; thus to change the angle of the FRFT, the distances between the lens and input−output planes and the lens powers have to be changed. Recently, an optical system based on two generalized lenses to perform a separable FRFT has been proposed [97]. This configuration permits one to change the fractional or transformation angles by a corresponding rotation of the lenses, but the resulting FRFT has a scaling depending on the angle values.

Here we obtain two symmetric systems containing three generalized lenses, which are able to perform both ortho-symplectic transformations (separable FRFT and GT) without adjusting distances when the transformation angles are changed. Note that such ortho-symplectic systems can be represented by the transformation matrix:

$$\mathbf{T} = \mathbf{M}_{z_1}\mathbf{M}_{L_1}\mathbf{M}_{z_2}\mathbf{M}_{L_2/2}\mathbf{M}_{L_2/2}\mathbf{M}_{z_2}\mathbf{M}_{L_1}\mathbf{M}_{z_1}. \tag{2.19}$$

We start considering the case $z_1 = 0$, see Fig. 2.1. Then the submatrices $\mathbf{A}_r, \mathbf{B}_r, \mathbf{C}_r$ and $\mathbf{D}_r$ are given by

$$\begin{aligned} \mathbf{A}_r &= \mathbf{L}_1 z_2 + \mathbf{I}, \\ \mathbf{B}_r &= \mathbf{I} z_2, \\ \mathbf{C}_r &= \mathbf{L}_1 + \frac{1}{2}\mathbf{L}_2 + \frac{1}{2}\mathbf{L}_2\mathbf{L}_1 z_2, \\ \mathbf{D}_r &= \frac{1}{2}\mathbf{L}_2 z_2 + \mathbf{I}. \end{aligned} \tag{2.20}$$

Thus, based on Eqs. (2.17), we obtain

$$\begin{aligned}\mathbf{X} &= z_2\left(2\mathbf{L}_1 + \mathbf{L}_2 + \mathbf{L}_1\mathbf{L}_2 z_2\right) + \mathbf{I},\\ \mathbf{Y} &= z_2\left(\mathbf{L}_2 z_2 + 2\mathbf{I}\right).\end{aligned} \tag{2.21}$$

Taking into account that $\mathbf{XY} = \mathbf{YX}$, one can see that $\mathbf{L}_1\mathbf{L}_2 = \mathbf{L}_2\mathbf{L}_1$ and therefore Eq. (2.18) holds. For the nonsingular case $\det \mathbf{Y} \neq 0$, see [81], the generalized lenses $\mathbf{L}_1$ and $\mathbf{L}_2$ can be written as a combination of the $\mathbf{X}$ and $\mathbf{Y}$ matrices as

$$\mathbf{L}_1 = \left(\mathbf{X} + \mathbf{I}\right)\mathbf{Y}^{-1} - \frac{1}{z_2}\mathbf{I}, \tag{2.22a}$$

$$\mathbf{L}_2 = \frac{1}{z_2^2}\left(\mathbf{Y} - 2z_2\mathbf{I}\right). \tag{2.22b}$$

Replacing the expressions $\mathbf{X}$ and $\mathbf{Y}$ from Eqs. (1.15) we find that the separable FRFT is obtained when

$$\mathbf{L}_1(\gamma_x, \gamma_y) = \begin{bmatrix} \cot\left(\frac{\gamma_x}{2}\right) - z_2^{-1} & 0 \\ 0 & \cot\left(\frac{\gamma_y}{2}\right) - z_2^{-1} \end{bmatrix}, \tag{2.23a}$$

$$\mathbf{L}_2(\gamma_x, \gamma_y) = \frac{1}{z_2^2}\begin{bmatrix} \sin\gamma_x - 2z_2 & 0 \\ 0 & \sin\gamma_y - 2z_2 \end{bmatrix}. \tag{2.23b}$$

Analogously, the generalized lenses corresponding to the GT operation [Eqs. (1.17)] are obtained from expression Eq. (2.22a) and Eq. (2.22b):

$$\begin{aligned}\mathbf{L}_1(\alpha) &= \begin{bmatrix} -z_2^{-1} & \cot\left(\frac{\alpha}{2}\right) \\ \cot\left(\frac{\alpha}{2}\right) & -z_2^{-1} \end{bmatrix},\\ \mathbf{L}_2(\alpha) &= \frac{1}{z_2^2}\begin{bmatrix} -2z_2 & \sin\alpha \\ \sin\alpha & -2z_2 \end{bmatrix}.\end{aligned} \tag{2.24}$$

If these generalized lenses are implemented by using ordinary cylindrical lenses, only some sets of angle parameters γ_x, γ_y or α are available without changing the lens power. For instance, the transformation angle interval $\alpha \in [\pi/2,\ 3\pi/2]$ is covered in the case of the GT and the antisymmetric FRFT $\gamma_x = -\gamma_y = \alpha$. This fact will be demonstrated in the next chapters in detail. Nevertheless, these limitations are overcome if these lenses are implemented by holographic multiplexing or by a programmable SLM.

For a singular case ($\det \mathbf{Y} = 0$) the expression Eq. (2.22a) cannot be applied. However, the generalized lens $\mathbf{L}_1$ is obtained from the following equation:

$$\mathbf{X} = \left(\mathbf{L}_1 + \frac{1}{z_2}\mathbf{I}\right)\mathbf{Y} - \mathbf{I}, \tag{2.25}$$

which is derived from the expressions given by Eqs. (2.21). It is easy to see that if $\mathbf{Y} = \mathbf{0}$ then $\mathbf{X} = -\mathbf{I}$, which coincides with: the separable FRFT for angles $\gamma_x = \gamma_y = \pi$, gyrator operation for $\alpha = \pi$, and image rotation at angle π. This operation is realizable by the proposed setup if $\mathbf{L}_1 = -z_2^{-1}\mathbf{I}$ and $\mathbf{L}_2 = -2z_2^{-1}\mathbf{I}$, that corresponds to a cascade of two Fourier transform systems.

In general, the singular case for the separable FRFT arises when at least one of the angles γ_x or γ_y equals $m\pi$, where m is an integer. Analyzing Eq. (2.25) we conclude that the FRFT operations for γ_x and/or γ_y equal to π can be obtained. In particular, for the case $\gamma_y = \pi$, the generalized lenses $\mathbf{L}_1$ and $\mathbf{L}_2$ are given by

$$\begin{aligned}\mathbf{L}_1(\gamma_x, \pi) &= \begin{bmatrix} \cot\left(\frac{\gamma_x}{2}\right) - z_2^{-1} & 0 \\ 0 & 0 \end{bmatrix},\\ \mathbf{L}_2(\gamma_x, \pi) &= \frac{1}{z_2^2}\begin{bmatrix} \sin\gamma_x - 2z_2 & 0 \\ 0 & -2z_2 \end{bmatrix}.\end{aligned} \tag{2.26}$$

Singular cases corresponding to the FRFT at angles γ_x and/or γ_y equal 0, and gyrator operation for $\alpha = 0$ (corresponding to the identity transform) cannot be realized by the proposed setup. Nevertheless, since this case corresponds to the well-known identity transform, imaging with unit magnification, we do not consider it. As it will be demonstrated in chapter 3 and 6, the proposed optical configuration is able to perform both operations for the transformation angle interval $[\pi/2, 3\pi/2]$ that is sufficient for the most of applications.

In conclusion, the separable FRFT and GT operation can be implemented by using a symmetric optical system constructed with two free-space intervals and three generalized lenses given by Eq. (2.23) and Eq. (2.24), respectively. Notice that the first and third generalized lenses are identical since the system is symmetric. The generalized lens design associated to $\mathbf{L}_1$ and $\mathbf{L}_2$ is discussed in the next section for both transformations.

2.3 Generalized lenses for antisymmetric FRFT and GT

A useful generalized lens is obtained when three particular lenses are properly assembled, $\mathcal{L}$=$\mathcal{L}_1\mathcal{L}_2\mathcal{L}_3$ (see Fig. 2.2), where $\mathcal{L}_1$ and $\mathcal{L}_2$ are convergent and divergent cylindrical lenses, respectively and $\mathcal{L}_3$ is a convergent spherical lens [92]. This generalized lens is used for the optical implementation of the antisymmetric FRFT and GT operations.

The cylindrical lenses $\mathcal{L}_1$ and $\mathcal{L}_2$ can be rotated while $\mathcal{L}_3$ remains fixed. Therefore $\mathcal{L}$ can be written as a function of $\mathcal{L}_1(\varphi_1)$, $\mathcal{L}_2(\varphi_2)$ and $\mathcal{L}_3$ as follows:

$$\mathcal{L} = -p \sin 2\omega \begin{bmatrix} -\sin 2\Omega & \cos 2\Omega \\ \cos 2\Omega & \sin 2\Omega \end{bmatrix} - p_3 \mathbf{I}, \tag{2.27}$$

where $\varphi_1 = \Omega + \omega$, $\varphi_2 = \Omega - \omega$, and $p = p_1 = -p_2$ and p_3 are the powers for the lenses $\mathcal{L}_1$, $\mathcal{L}_2$, and $\mathcal{L}_3$, correspondingly.

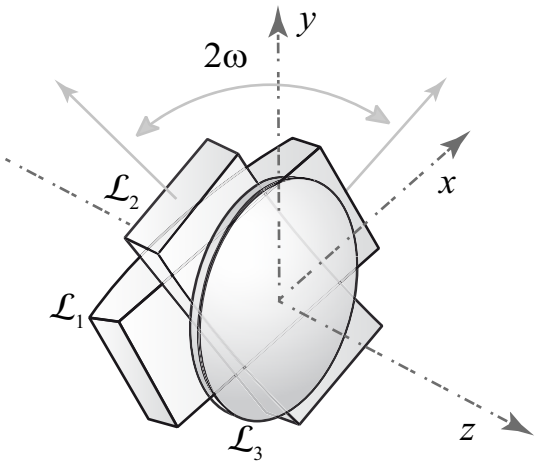

Figure 2.2: Optical system scheme associated to $\mathcal{L}$=$\mathcal{L}_1\mathcal{L}_2\mathcal{L}_3$ generalized lens.

For the antisymmetric FRFT [Eqs. (2.23) with $\gamma_x = -\gamma_y = \alpha$], $\mathbf{L}_2$ can be implemented by using lens $\mathcal{L}$ with the following parameters: $\Omega = -\pi/4$, $2\omega = \alpha = 2\varphi_1 + \pi/2$, $p = 1/z_2^2$, and $p_3 = 2/z_2$. Different values of angle α for $\mathbf{L}_2(\alpha, -\alpha)$ are obtained by rotation of cylindrical lens $\mathcal{L}_{1,2}$, while the angle $\varphi_1 + \varphi_2 = -\pi/2$ is fixed. Meanwhile, the lens

$$\mathbf{L}_1(\alpha, -\alpha) = \begin{bmatrix} \cot\left(\frac{\alpha}{2}\right) - z_2^{-1} & 0 \\ 0 & -\cot\left(\frac{\alpha}{2}\right) - z_2^{-1} \end{bmatrix}, \tag{2.28}$$

can also be implemented by means of the $\mathcal{L}$ setup, Eq. (2.27), but only for certain values of α such that $\cot(\alpha/2) = p \sin 2\omega$. In this case $\Omega = -\pi/4$, $2\omega = 2\varphi_1 + \pi/2$ and $p_3 = 1/z_2$.

For the GT operation [see Eqs. (2.24)] the lens $\mathbf{L}_1(\alpha)$, at the same angular interval as in the case of the antisymmetric FRFT (given by $\cot(\alpha/2) = p \sin 2\omega$), can be obtained by using $\mathcal{L}$ with the following parameters: $\Omega = 0$, $\omega = \varphi_1$ and $p_3 = 1/z_2$. The lens $\mathbf{L}_2(\alpha)$ [Eqs. (2.24)] is obtained for $\Omega = 0$, $2\omega = \alpha = 2\varphi_1$, $p = -1/z_2^2$, and $p_3 = 2/z_2$. In contrast to the antisymmetric FRFT case, these generalized lenses can be simplified to an assembled set of two convergent cylindrical lenses. This will be demonstrated in chapter 6 in detail.

The considered generalized lens configuration allows to implement easily both transformations, antisymmetric FRFT and GT, where the variation of the transformation angle is only reached by lens rotation. Notice that the rotation of the cylindrical lenses implies a variable lens power associated to the generalized lens. For the separable and symmetric FRFT ($\gamma_x = \gamma_y$) the lens power of the generalized lenses cannot be changed by means of lens rotations, and hence the lens power have to be adjusted directly. Nevertheless, these lenses can be implemented by holographic multiplexing or by a programmable SLM. In the following chapters this optical configuration and their experimental implementation will be discussed.

2.4 Systems for image rotation

As previously mentioned, several schemes for image rotation by lens-based setups have been proposed in the last decade. Some of them do not produce to pure rotation since they introduce an additional phase modulation of the rotated image. Therefore we call them imperfect rotators. Others are reflectors with rotation [85], which also belong to the class of ortho-symplectic systems, and are described by the submatrices

$$\mathbf{X}_{ref}(\theta) = \begin{bmatrix} \cos\theta & \sin\theta \\ \sin\theta & -\cos\theta \end{bmatrix}, \mathbf{Y} = \mathbf{0}. \tag{2.29}$$

Note that a cascade of two reflectors with rotation angles θ_1 and θ_2 corresponds to a rotator with angle $\theta_1 - \theta_2$ [83, 86, 91], since

$$\begin{aligned} \mathbf{X}_{rot}(\theta_1 - \theta_2) &= \mathbf{X}_{ref}(\theta_2)\mathbf{X}_{ref}(\theta_1) = \begin{bmatrix} \cos\theta_2 & \sin\theta_2 \\ \sin\theta_2 & -\cos\theta_2 \end{bmatrix}\begin{bmatrix} \cos\theta_1 & \sin\theta_1 \\ \sin\theta_1 & -\cos\theta_1 \end{bmatrix} \\ &= \begin{bmatrix} \cos(\theta_1 - \theta_2) & \sin(\theta_1 - \theta_2) \\ -\sin(\theta_1 - \theta_2) & \cos(\theta_1 - \theta_2) \end{bmatrix}. \end{aligned} \tag{2.30}$$

Our strategy will be to find a minimal configuration to perform an imperfect rotator and to correct it by an additional lens.

It can be demonstrated that a system with one lens cannot perform image rotation except in the trivial case $\theta = \pi$. Let us consider a system with two lenses $z_1\mathbf{L}_1 z_2 \mathbf{L}_2 z_3$. The submatrix parameters in this case are given by

$$\mathbf{A}_2 = \mathbf{L}_1(z_2 + z_3) + \mathbf{L}_2 z_3 + \mathbf{L}_2\mathbf{L}_1 z_2 z_3 + \mathbf{I}, \tag{2.31a}$$

$$\mathbf{B}_2 = \mathbf{L}_1(z_2 + z_3)z_1 + \mathbf{L}_2(z_2 + z_1)z_3 + \mathbf{L}_2\mathbf{L}_1 z_2 z_3 z_1 + \mathbf{I}(z_2 + z_3 + z_1), \tag{2.31b}$$

$$\mathbf{C}_2 = \mathbf{L}_1 + \mathbf{L}_2 + \mathbf{L}_2\mathbf{L}_1 z_2, \tag{2.31c}$$

$$\mathbf{D}_2 = \mathbf{L}_1 z_1 + \mathbf{L}_2(z_1 + z_2) + \mathbf{L}_2\mathbf{L}_1 z_2 z_1 + \mathbf{I}, \tag{2.31d}$$

and Eq. (2.6) for $n = 2$,

$$\mathbf{B}_2 = \mathbf{A}_2 z_1 - \mathbf{C}_2 z_1 z_3 + \mathbf{D}_2 z_3 + \mathbf{I} z_2. \tag{2.32}$$

Applying the conditions $\mathbf{A}_2 = \mathbf{D}_2 = \mathbf{X}$, and $\mathbf{B}_2 = \mathbf{0}$, the latter equation reduces to

$$\mathbf{C}_2 z_1 z_3 - \mathbf{I} z_2 = \mathbf{X}(z_1 + z_3). \tag{2.33}$$

It is easy to see that the requirement $\mathbf{C}_2 = \mathbf{0}$ only leads to the trivial solution $\theta = \pi$. Therefore the transformation matrix associated to this system is given by

$$\mathbf{T} = \begin{bmatrix} \mathbf{X} & \mathbf{0} \\ \mathbf{C}_2 & \mathbf{X} \end{bmatrix}, \tag{2.34}$$

with $\mathbf{X} = (\mathbf{C}_2 z_1 z_3 - \mathbf{I} z_2)/(z_1 + z_3)$. Thus from Eq. (2.31c) we conclude that the imperfect rotator cannot be constructed by a two-lens configuration, since $\mathbf{C}_2$ is a symmetric matrix.

Let us now demonstrate that the minimum number of generalized lenses to perform a pure rotator operation is four. We start from the consideration of the system that contains three lenses to perform an imperfect rotator $z_1\mathbf{L}_1 z_2 \mathbf{L}_2 z_3 \mathbf{L}_3 z_4$ and then transform it to a pure rotator applying an additional lens. Using the expressions derived in section 2.1, the submatrices for the three-lens configuration are related to each other as

$$\begin{aligned}
\mathbf{A}_3 &= \mathbf{C}_3 z_4 + \mathbf{B}_1^e \mathbf{L}_1 + \mathbf{L}_2 z_3 + \mathbf{I}, \\
\mathbf{B}_3 &= \mathbf{A}_3 z_1 - \mathbf{C}_3 z_1 z_4 + \mathbf{D}_3 z_4 + \mathbf{B}_1^e, \\
\mathbf{C}_3 &= \mathbf{L}_3[\mathbf{L}_1(z_2 + z_3) + \mathbf{L}_2 z_3 + \mathbf{L}_2 \mathbf{L}_1 z_2 z_3 + \mathbf{I}] + [\mathbf{L}_1 + \mathbf{L}_2 + \mathbf{L}_2 \mathbf{L}_1 z_2], \\
\mathbf{D}_3 &= \mathbf{C}_3 z_1 + \mathbf{L}_3 \mathbf{B}_1^e + \mathbf{L}_1 z_1 + \mathbf{L}_2 (z_1 + z_2) + \mathbf{L}_2 \mathbf{L}_1 z_2 z_1 + \mathbf{I}, \qquad (2.35) \\
\mathbf{B}_1^e &= \mathbf{L}_2 z_3 z_2 + \mathbf{I}(z_2 + z_3), \qquad (2.36)
\end{aligned}$$

where the symbol e is related to the submatrix of the embedded system of Eq. (2.6). Applying the conditions for the imperfect rotator, $\mathbf{A}_3 = \mathbf{D}_3 = \mathbf{X}_{rot}$, $\mathbf{B}_3 = \mathbf{0}$ and $\mathbf{C}_3 \neq \mathbf{0}$, we obtain

$$\mathbf{X}_{rot} = \frac{1}{(z_1 + z_4)} \left(\mathbf{C}_3 z_1 z_4 - \mathbf{B}_1^e \right). \tag{2.37}$$

From the latter equation we conclude that it is impossible to construct a pure rotator with three lenses. Indeed, if $\mathbf{C}_3 = \mathbf{0}$ we cannot satisfy Eq. (2.37), since lenses (in particular $\mathbf{L}_2$) are represented by symmetrical matrices [Eq. (2.1)], while $\mathbf{X}_{rot}$ is not symmetrical.

Equations (2.35)–(2.37) are significantly simplified if we suppose that $z_1 = z_2 = z_3 = z_4 = z$ and choose $\mathbf{L}_2$ in the form of a cylindrical lens operating in the y direction:

$$\mathbf{L}_2 = \begin{bmatrix} 0 & 0 \\ 0 & -p \end{bmatrix}. \tag{2.38}$$

Then the embedded system, and in particular $\mathbf{B}_1^e$, is completely defined as well as the rest of the lenses, including the lens $\mathbf{L}_4 = -\mathbf{C}_3 \mathbf{X}_{rot}^{-1}$ added in order to compensate the quadratic phase modulation:

$$\begin{aligned}
\mathbf{L}_1 &= (\mathbf{B}_1^e)^{-1} (\mathbf{I} - \mathbf{X}_{rot}) - \frac{2}{z}\mathbf{I}, \\
\mathbf{L}_3 &= -\left[z(\mathbf{B}_1^e)^{-1}(\mathbf{I} - \mathbf{X}_{rot}) + 3\mathbf{X}_{rot} + \mathbf{I} + \frac{2}{z}\mathbf{B}_1^e \right] \left[z\mathbf{X}_{rot} + \mathbf{B}_1^e \right]^{-1}, \\
\mathbf{L}_4 &= -\frac{1}{z^2} \left(2z\mathbf{I} + \mathbf{B}_1^e \mathbf{X}^{-1} \right). \qquad (2.39)
\end{aligned}$$

In particular for the case $p = 4/z$, the following set of lenses performing a pure rotator operation

is obtained:

$$\begin{aligned}
\mathbf{L}_1 &= -\frac{1}{2z}\begin{bmatrix} 1+\cos\theta & \sin\theta \\ \sin\theta & 1-\cos\theta \end{bmatrix} - \frac{1}{z}\begin{bmatrix} 1 & 0 \\ 0 & 2 \end{bmatrix}, \\
\mathbf{L}_2 &= -\frac{4}{z}\begin{bmatrix} 0 & 0 \\ 0 & 1 \end{bmatrix}, \\
\mathbf{L}_3 &= -\frac{1}{2z}\begin{bmatrix} 1+\cos\theta & -\sin\theta \\ -\sin\theta & 1-\cos\theta \end{bmatrix} - \frac{1}{z}\begin{bmatrix} 1 & 0 \\ 0 & 2 \end{bmatrix}, \\
\mathbf{L}_4 &= -\frac{2}{z}\begin{bmatrix} 1+\cos\theta & -\sin\theta \\ -\sin\theta & 1-\cos\theta \end{bmatrix}.
\end{aligned} \tag{2.40}$$

We remark that $\mathbf{L}_3(\theta) = \mathbf{L}_1(-\theta)$.

In conclusion we have demonstrated that four is the minimum number of generalized lenses needed to perform the pure rotator. The proposed scheme is flexible (the rotation angle θ is changed only by lens rotation) and can be performed by the combination of conventional cylindrical lenses, Eq. (2.40).

2.5 Conclusions

We have considered first-order optical systems containing only thin lenses and free-space intervals, which are able to perform ortho-symplectic transformation in phase space. Several useful equations that connect the parameters of the transformation matrix for a general and symmetrical anamorphic first-order optical system, have been derived. It has been shown that symmetrical anamorphic systems cannot perform a rotation operation except the trivial one.

Flexible configurations for three principal transformations in phase space; image rotation, separable FRFT, and GT operation, have been obtained. The first one contains four generalized lenses and can be performed by the combination of conventional cylindrical lenses. The separable FRFT and GT operations can be performed by a symmetrical anamorphic setup that contains three generalized lenses. The transformation angles can be obtained by applying a set of conventional cylindrical or alternatively by holographic multiplexed lenses. To cover all angular combinations for the separable FRFT, except some singular cases, these lenses have to be implemented by an SLM. The results presented in this chapter were reported in [107].

Chapter 3

Optical implementation for separable fractional FT and rotator operation

In this chapter we analyze the design of flexible optical systems associated to separable FRFT and rotator operation, with the aim to be achieved them experimentally. As an example of their action, we also consider different numerical simulations based on the angular spectrum algorithm for the Fresnel integral calculation (appendix A).

3.1 Separable fractional Fourier transform

As it was introduced in chapter 1, the separable FRFT at angles γ_x and γ_y is defined as $f_o(\mathbf{r}_o) = R^{\gamma_x} R^{\gamma_y}[f_i(\mathbf{r}_i)](\mathbf{r}_o)$, where

$$\begin{aligned} &R^{\gamma_x}[f_i(\mathbf{r}_i)](\mathbf{r}_o) \\ &= \frac{\exp(i\gamma_x/2)}{\sqrt{i \sin\gamma_x}} \int f_i(x_i, y_i) \, \exp\left(i\pi \left[(x_o^2 + x_i^2)\cot\gamma_x - 2x_i x_o \csc\gamma_x\right]\right) \mathrm{d}x_i, \end{aligned} \tag{3.1}$$

and $\mathbf{r}_{i,o}^t = (x_{i,o}, y_{i,o})$ indicates the input and output dimensionless coordinates, respectively. We remind that t stands for transposition operation and $R^{\gamma_x} R^{\gamma_y} = R^{\gamma_x, \gamma_y}$. The flexible system for its optical implementation requires three generalized lenses and two free-space intervals, as we have previously demonstrated.

The transformation parameters cannot be changed by means of lens rotation in the case of arbitrary combination of angles γ_x and γ_y. Indeed, in this case both generalized lenses correspond to an assembled set of two crossed cylindrical lenses [see Eqs. (2.23a)] at angle $\pi/2$, with variable lens power. This fact implies that the transformation angles have to be changed by varying directly the lens power. The optical implementation of these generalized lenses can be achieved by means of SLMs or multiplexed holograms, instead of conventional lenses for each combination of transformation angles. We remark that this optical setup does not require to change the distance between lenses.

The evolution of the complex field amplitude $g_i(x_i, y_i)$ during the propagation through this system is derived by means of the Fresnel diffraction integral [Eq. (1.10)] calculation, corresponding to each free-space interval, and the phase modulation functions associated to generalized lens $\mathbf{L}_1$ and $\mathbf{L}_2$. Analyzing the expressions Eq. (2.23a) and Eq. (2.23b), we conclude

that the phase modulation function associated to the generalized lens $\mathbf{L}_1$can be written as

$$\Psi_1(x,y) = \exp\left(-i\pi\frac{x^2+y^2}{\lambda f_1}\right)\exp\left(i\pi\frac{x^2\cot(\gamma_x/2)+y^2\cot\left(\gamma_y/2\right)}{\lambda f_2}\right), \tag{3.2}$$

meanwhile for the lens $\mathbf{L}_2$ it is given by

$$\Psi_2(x,y) = \exp\left(-i\pi\frac{x^2+y^2}{\lambda f_3}\right)\exp\left(i\pi\frac{x^2\sin\gamma_x+y^2\sin\gamma_y}{\lambda f_4}\right). \tag{3.3}$$

For the focal distance $f_1 = z$ the complex field just before the second generalized lens is written as it follows:

$$\begin{aligned} g_1(x_1,y_1) = \frac{1}{i\lambda z}\exp\left(i\pi\frac{x_1^2+y_1^2}{\lambda z}\right)\iint g_i(x_i,y_i)\exp\left(-i2\pi\frac{x_1x_i+y_1y_i}{\lambda z}\right) \\ \times\exp\left(i\pi\frac{x_i^2\cot(\gamma_x/2)+y_i^2\cot\left(\gamma_y/2\right)}{\lambda f_2}\right)\mathrm{d}x_i\mathrm{d}y_i. \end{aligned} \tag{3.4}$$

After the corresponding phase modulation by the lens $\mathbf{L}_2$, with $f_3 = f_4 = z/2$, and the propagation through a free-space interval z we derive:

$$\begin{aligned} g_2(x_2,y_2) = \frac{\exp\left(i\pi\left(x_2^2+y_2^2\right)/\lambda z\right)}{2\lambda z\sqrt{\sin\gamma_x\sin\gamma_y}}\iint g_i(x_i,y_i)\exp\left(i\pi\frac{x_i^2\cot(\gamma_x/2)+y_i^2\cot\left(\gamma_y/2\right)}{\lambda f_2}\right) \\ \times\exp\left(-i\pi\frac{(x_2+x_i)^2\csc\gamma_x+(y_2+y_i)^2\csc\gamma_y}{2\lambda z}\right)\mathrm{d}x_i\mathrm{d}y_i. \end{aligned} \tag{3.5}$$

The final expression for the complex field amplitude, at the output plane of the FRFT setup ($\mathbf{r}_2 = \mathbf{r}_o$), is obtained thanks to the third lens ($\mathbf{L}_1$) application:

$$\begin{aligned} g_o(x_o,y_o) = \frac{1/2\lambda z}{\sqrt{\sin\gamma_x\sin\gamma_y}}\iint g_i(x_i,y_i)\exp\left(-i\pi\frac{(x_o+x_i)^2\csc\gamma_x+(y_o+y_i)^2\csc\gamma_y}{2\lambda z}\right) \\ \times\exp\left(i\pi\frac{\left(x_o^2+x_i^2\right)\cot(\gamma_x/2)+\left(y_o^2+y_i^2\right)\cot\left(\gamma_y/2\right)}{\lambda f_2}\right)\mathrm{d}x_i\mathrm{d}y_i. \end{aligned} \tag{3.6}$$

Thus the expression Eq. (3.6) for $f_2 = 2z$ coincides with the definition of the separable FRFT, given by Eq. (3.1), except a constant phase factor and with normalization $s^2 = 2\lambda z$. Notice that $\cot(\gamma/2) = \csc\gamma + \cot\gamma$.

Finally we derive the expression for the generalized lenses $\mathbf{L}_1$ and $\mathbf{L}_2$ which are an assembled set of two crossed (at angle $\pi/2$) cylindrical lenses with variable lens power given by:

$$\begin{aligned} p_{x,y;1} &= z^{-1}\left(1-\cot\left(\gamma_{x,y}/2\right)/2\right), \\ p_{x,y;2} &= 2z^{-1}\left(1-\sin\gamma_{x,y}\right), \end{aligned} \tag{3.7}$$

respectively. The operation curves corresponding to both generalized lenses are displayed in Fig. 3.1. These operation curves correspond to the lens power variation as a function of the transformation angles. We remind that the propagation distance z among lenses remains fixed. Singular case arises when at least one of the angles γ_x or γ_y equals $m\pi$, where m is an integer.

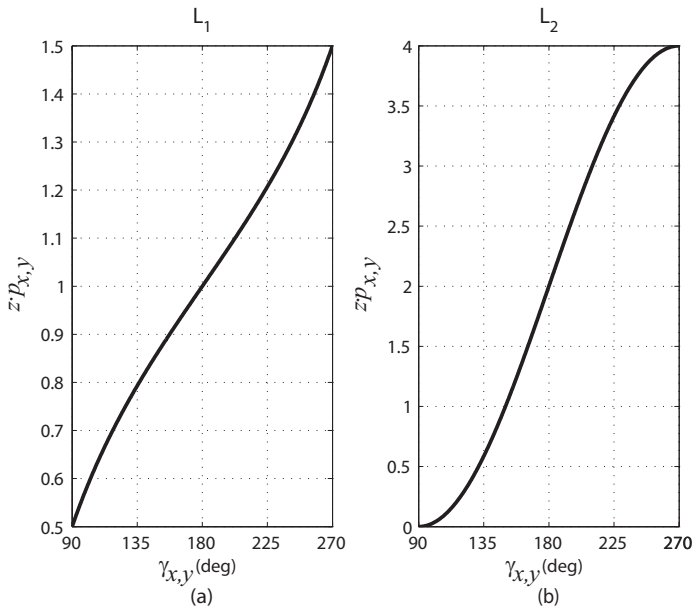

Figure 3.1: Normalized operation curves $zp_{x,y}$ for the generalized lenses $\mathbf{L}_1$(a) and $\mathbf{L}_2$ (b), corresponding to the separable FRFT setup.

Therefore, this setup performs the separable FRFT for the angle interval $\gamma_{x,y} \in [\pi/2, 3\pi/2]$, see Fig. 3.1. This interval is sufficient for a large list of the FRFT applications including adaptive filtering, beam characterization, phase space tomography, etc. Nevertheless, the entire interval $\gamma_{x,y} \in (0, 2\pi)$ can be also covered, due to $R^{\gamma_x+\pi,\gamma_y+\pi}[f_i(\mathbf{r}_i)](\mathbf{r}_o) = R^{\gamma_x,\gamma_x}[f_i(\mathbf{r}_i)](-\mathbf{r}_o)$.

As an example, Fig. 3.2 displays the intensity distribution for the separable FRFT at angles $\gamma = 2\gamma_x = -\gamma_y$ for $\gamma = \pi/4$ (b), $\gamma = \pi/2$ (c), and $\gamma = 3\pi/4$ (d). Note that the input image (a) corresponds to $\gamma = 0$. This numerical simulation has been realized for the wavelength $\lambda = 532$ nm, and $z = 0.5$ m where the input image size was set at 428×256 points (with pixel size of 20 μm). As mentioned, this optical setup simulation is based on Fresnel diffraction integral calculation which is discussed in appendix A.

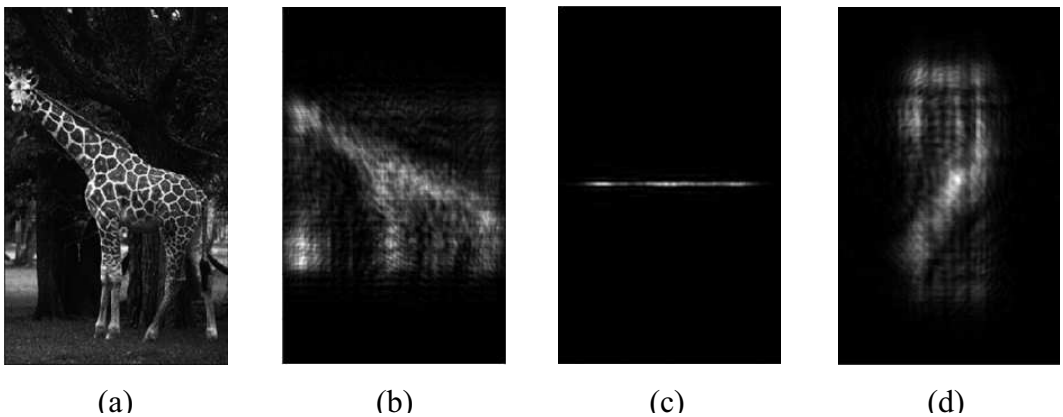

Figure 3.2: Intensity distribution for the FRFT transform at angles $\gamma = 2\gamma_x = -\gamma_y$ for $\gamma = 0$, input image (a), $\gamma = \pi/4$ (b), $\gamma = \pi/2$ (c) and $\gamma = 3\pi/4$ (d).

In the case of the antisymmetric FRFT $\gamma_x = -\gamma_y = \alpha$, the transformation angle α can be changed through lens rotations since the generalized lenses can be implemented by the triplet lens configuration discussed in Section 2.3. The optical implementation for this case will be analyzed in the next Section.

3.1.1 Optical setup for antisymmetric FRFT

The antisymmetric FRFT is defined by the expression:

$$\begin{aligned} f_o(\mathbf{r}_o) &= R^{\alpha,-\alpha}[f_i(\mathbf{r}_i)](\mathbf{r}_o) \\ &= \frac{1}{|\sin\alpha|}\iint f_i(x_i,y_i)\,\exp\left(i\pi\frac{(x_o^2-y_o^2+x_i^2-y_i^2)\cos\alpha-2\,(x_ix_o-y_iy_o)}{\sin\alpha}\right)\mathrm{d}x_i\mathrm{d}y_i, \end{aligned} \tag{3.8}$$

Note that for $\alpha = 0$ it corresponds to the identity transform. For $\alpha = \pi/2$ it reduces to the FT along the x direction and inverse FT for the y direction. In the case $\alpha = \pi$ the reverse transform $f_i(-x_o, -y_o)$ is obtained.

In this case, every generalized lens can be constructed by a combination of three thin lenses with the same power modulus: a convergent and divergent cylindrical lens together with convergent spherical one, Fig. 3.3. This generalized lens configuration corresponds to a quadratic phase modulation function given by

$$\Psi(\mathbf{r},\varphi) = \exp\left(-i\pi\frac{x^2+y^2+\left(x^2-y^2\right)\cos 2\varphi}{\lambda f}\right), \tag{3.9}$$

where λ is the wavelength, f is the focal distance, and angle φ indicates the position of the corresponding symmetry axis associated to the cylindrical lens. Thus the axis of the cylindrical lenses form an angle $\phi_1 = \varphi$ and $\phi_2 = -(\varphi + \pi/2)$ with the vertical axis OY, respectively [87, 92]. The focal distance of the first generalized lens, f_1, equals the distance z between two consecutive generalized lenses of the setup. Meanwhile $f_2 = z/2$ corresponds to the focal distance of the second generalized lens, $\mathbf{L}_2$.

The evolution of the complex amplitude field $g_i(x_i, y_i)$ during the propagation through this system can be also derived applying the same procedure as explained in the previous case. Applying the expression Eq. (3.9) corresponding to $\mathbf{L}_1$, we obtain the expression for the complex field just before the second generalized lens:

$$\begin{aligned} g_1(x_1,y_1) = \frac{1}{i\lambda z}\exp\left(i\pi\frac{x_1^2+y_1^2}{\lambda z}\right)\iint g_i(x_i,y_i) \\ \times\exp\left(-i\pi\frac{\left(x_i^2-y_i^2\right)\cos 2\varphi_1}{\lambda z}\right)\exp\left(-i2\pi\frac{x_1x_i+y_1y_i}{\lambda z}\right)\mathrm{d}x_i\mathrm{d}y_i. \end{aligned} \tag{3.10}$$

After the corresponding modulation by the lens transfer function associated to $\mathbf{L}_2$, and the propagation through a free-space interval z we get:

$$\begin{aligned} g_2(x_2,y_2) = \frac{i}{\left|2\lambda z\cos 2\varphi_2\right|}\exp\left(i\pi\frac{x_2^2+y_2^2}{\lambda z}\right)\iint g_i(x_i,y_i) \\ \times\exp\left(i\pi\frac{(x_2+x_i)^2-(y_2+y_i)^2}{2\lambda z\cos 2\varphi_2}\right)\exp\left(-i\pi\frac{\left(x_i^2-y_i^2\right)\cos 2\varphi_1}{\lambda z}\right)\mathrm{d}x_i\mathrm{d}y_i. \end{aligned} \tag{3.11}$$

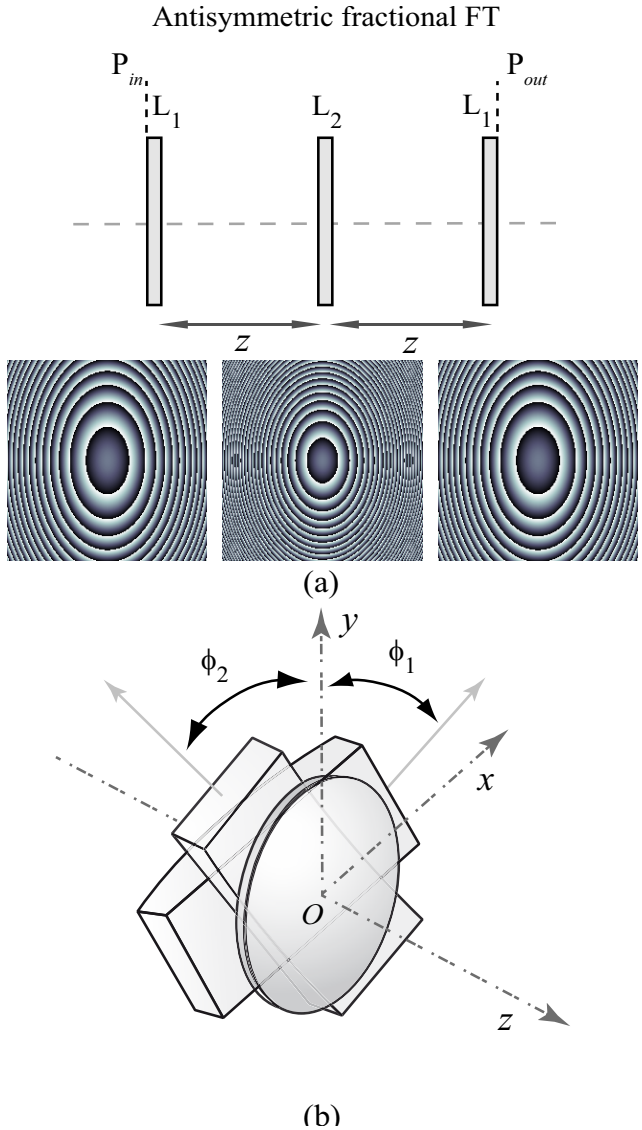

Figure 3.3: Setup scheme associated to the FRFT transform, (a). The phase modulation functions (for the case $z = 0.5$ m and $\lambda = 532$ nm) associated to each generalized lenses when the setup performs the FRFT $(\alpha, -\alpha)$ at angle $\alpha = 3\pi/4$ are shown below, where the grey levels indicate the phase distribution range $[-\pi, \pi]$. (b) The generalized lenses $\mathbf{L}_1$and $\mathbf{L}_2$ scheme are displayed.

The final expression for the complex field amplitude, at the output plane of this FRFT setup ($\mathbf{r}_2 = \mathbf{r}_o$), is obtained thanks to the third lens ($\mathbf{L}_1$) action:

$$g_o(x_o, y_o) = \frac{-i}{\left|2\lambda z \cos 2\varphi_2\right|} \iint g_i(x_i, y_i) \times \exp\left(i\pi \frac{\left(x_o^2 - y_o^2 + x_i^2 - y_i^2\right)(2\cos 2\varphi_1 \cos 2\varphi_2 - 1) - 2\left(x_o x_i - y_o y_i\right)}{2\lambda z \cos 2\varphi_2} \right) \mathrm{d}x_i \mathrm{d}y_i. \quad (3.12)$$

The latter equation coincides, except to a constant phase factor, with the definition of the antisymmetric FRFT, Eq. (3.8), with normalization $s^2 = \lambda z$ if

$$\begin{aligned} \cos 2\varphi_1 &= \cot(\alpha/2), \\ \cos 2\varphi_2 &= (\sin\alpha)/2. \end{aligned} \quad (3.13)$$

Notice that the angles φ_1 and φ_2 correspond to the generalized lenses $\mathbf{L}_1$and $\mathbf{L}_2$, respectively. It is easy to see from the latter relation that this setup performs the antisymmetric FRFT only for the angles $\alpha \in [\pi/2,\ 3\pi/2]$. Nevertheless since $R^{\alpha+\pi,-(\alpha+\pi)}[f_i(\mathbf{r}_i)](\mathbf{r}_o) = R^{\alpha,-\alpha}[f_i(\mathbf{r}_i)](-\mathbf{r}_o)$ entire interval $\alpha \in [0,\ 2\pi]$ can be covered if it is necessary.

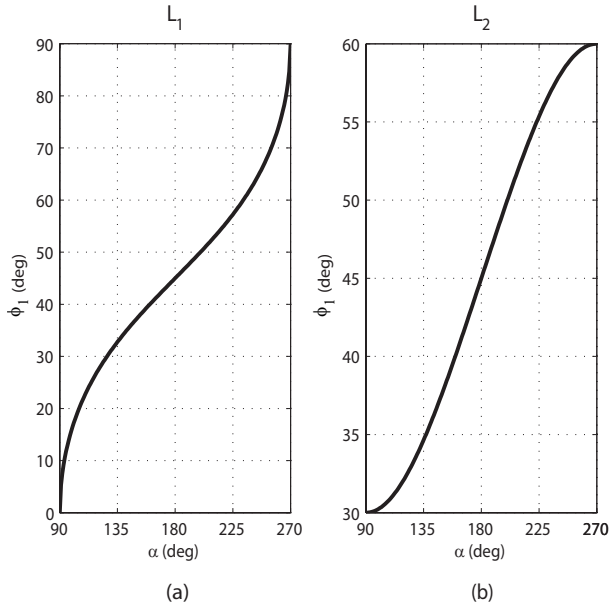

Figure 3.4: Operation curves $\phi_1(\alpha)$ for the generalized lenses $\mathbf{L}_1$(a) and $\mathbf{L}_2$ (b), corresponding to the antisymmetric FRFT setup. The operation curve $\phi_2(\alpha)$ is derived from the relation $\phi_2 = -(\phi_1 + \pi/2)$.

The variation of the transformation angle α is achieved by means of the rotation of cylindrical lenses according to Eq. (3.13) that leads to the operation curves $\phi_1(\alpha)$ for the generalized lens $\mathbf{L}_1$ and $\mathbf{L}_2$. Both operations curves are displayed in Fig. 3.4(a) and (b), respectively. Note that the operation curve $\phi_2(\alpha)$ is derived from the relation $\phi_2 = -(\phi_1 + \pi/2)$. When the angle between the cylindrical lenses is set at π a generalized lens reduces to a spherical one.

3.2 Rotator operation

It was demonstrated in chapter 2 that the rotator operation can be implemented by using four generalized lenses located at fixed positions. The rotation angle θ is changed through lens rotations given by:

$$\begin{aligned}
\mathbf{L}_1 &= -\frac{1}{2z}\begin{bmatrix} 1+\cos\theta & \sin\theta \\ \sin\theta & 1-\cos\theta \end{bmatrix} - \frac{1}{z}\begin{bmatrix} 1 & 0 \\ 0 & 2 \end{bmatrix}, \\
\mathbf{L}_2 &= -\frac{4}{z}\begin{bmatrix} 0 & 0 \\ 0 & 1 \end{bmatrix}, \\
\mathbf{L}_3 &= -\frac{1}{2z}\begin{bmatrix} 1+\cos\theta & -\sin\theta \\ -\sin\theta & 1-\cos\theta \end{bmatrix} - \frac{1}{z}\begin{bmatrix} 1 & 0 \\ 0 & 2 \end{bmatrix}, \\
\mathbf{L}_4 &= -\frac{2}{z}\begin{bmatrix} 1+\cos\theta & -\sin\theta \\ -\sin\theta & 1-\cos\theta \end{bmatrix}.
\end{aligned} \tag{3.14}$$

As mentioned, this system configuration leads to the following output complex field amplitude:

$$f_o(\mathbf{r}_o) = f_i(x_o\cos\theta - y_o\sin\theta,\ y_o\cos\theta + x_o\sin\theta). \tag{3.15}$$

The setup scheme for the rotator operation is displayed in Fig. 3.5. The first lens, $\mathbf{L}_1$, corresponds to an assembled set of three cylindrical lenses: one of them rotated at angle θ with focal distance equal to $2z$ whereas the other ones are fixed in the x and y direction with focal distances z and $z/2$, correspondingly. The generalized lens $\mathbf{L}_2$ corresponds to a cylindrical lens fixed in the x direction with focal distance $z/4$. Meanwhile, the lens $\mathbf{L}_3 = \mathbf{L}_1(-\theta)$ and $\mathbf{L}_4$ corresponds to a cylindrical lens rotated at angle θ with focal distance equal to $z/2$. Therefore eight convergent cylindrical lenses have to be used.

Let us now introduce the phase modulation functions $\Psi_n(\mathbf{r},\theta)$, associated to each generalized lens $\mathbf{L}_n$ given by Eq. (3.14):

$$\begin{aligned}
\Psi_1(\mathbf{r},\theta) &= \exp\left(-i\pi\frac{x^2+y^2-xy\sin 2\theta}{2\lambda z}\right)\exp\left(-i\pi\frac{x^2+2y^2}{\lambda z}\right), \\
\Psi_2(\mathbf{r},\theta) &= \exp\left(-i\pi\frac{4y^2}{\lambda z}\right), \\
\Psi_3(\mathbf{r},\theta) &= \Psi_1(\mathbf{r},-\theta), \\
\Psi_4(\mathbf{r},\theta) &= \exp\left(-i2\pi\frac{x^2+y^2+xy\sin 2\theta}{\lambda z}\right).
\end{aligned} \tag{3.16}$$

In Fig. 3.5, bottom panel, these functions are displayed for the rotation angle $\theta = \pi/4$.

As an example of the rotator action, a numerical simulation for the proposed optical setup is achieved for the case $\theta = \pi/4$, and π, see Fig. 3.6. This numerical simulation has been realized for the wavelength $\lambda = 532$ nm, $z = 0.5$ m, where the input image size was set at 428×256 points (with pixel size of 20 μm). These results are in good agreement with the theoretical predictions.

The proposed rotator setup corresponds to the optimal lens-based configuration since it requires the minimum number of lenses and free-space intervals, as we demonstrated in Section 2.4. For instance, other rotator lens-based setup proposed in [84] requires ten cylindrical lenses and eight free-space intervals. This setup corresponds to the cascade of two reflector systems and hence a high number of lenses and free-space intervals have to be used. Moreover, the rotation angle is reached by the rotation of the last reflector with respect the other one. Finally, other system performing the rotation operation can be constructed using two Dove prisms,

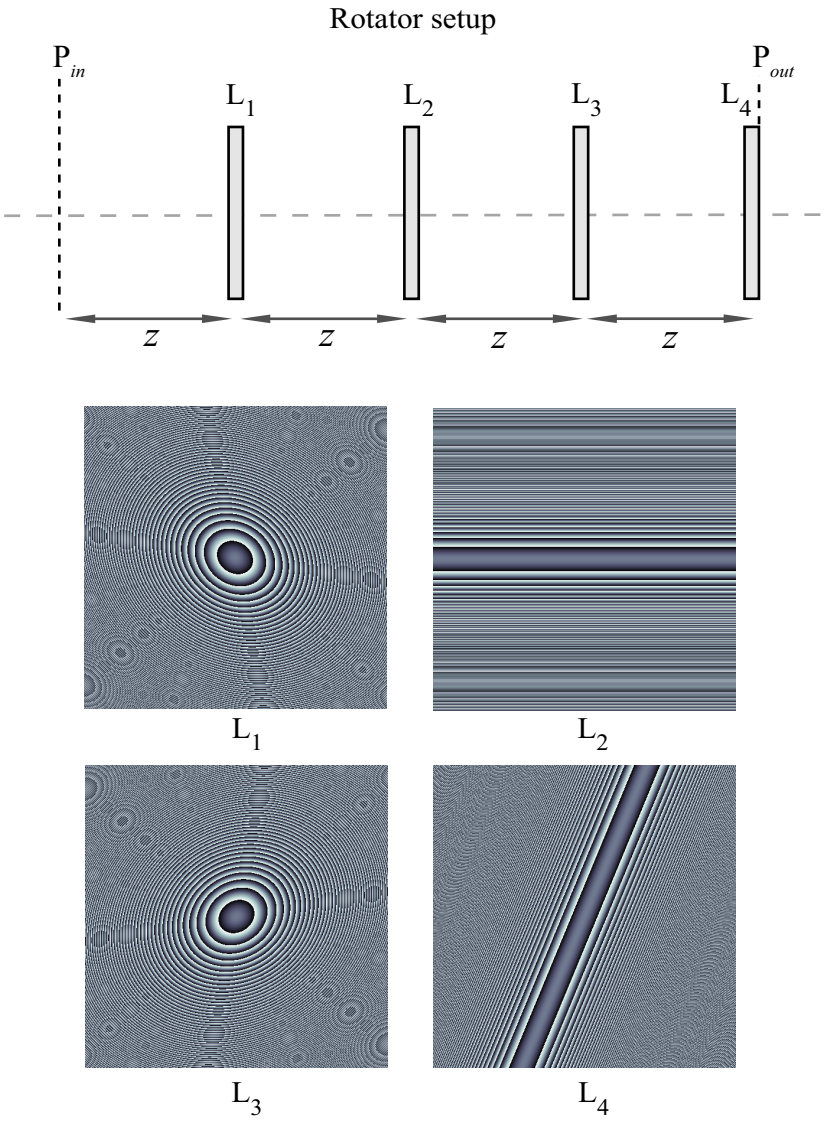

Figure 3.5: Setup scheme for the rotator operation. The phase modulation functions associated to generalized lenses $\mathbf{L}_1$, $\mathbf{L}_2$, $\mathbf{L}_3$, and $\mathbf{L}_4$ are shown below for the case $\theta = \pi/4$, where grey levels indicate the phase distribution range $[-\pi, \pi]$. These modulation functions correspond to the case: $\theta = \pi/4$, $z = 0.5$ m, and $\lambda = 532$ nm. The input plane is indicated by P_{in}, meanwhile the output plane coincides with lens $\mathbf{L}_4$ plane.

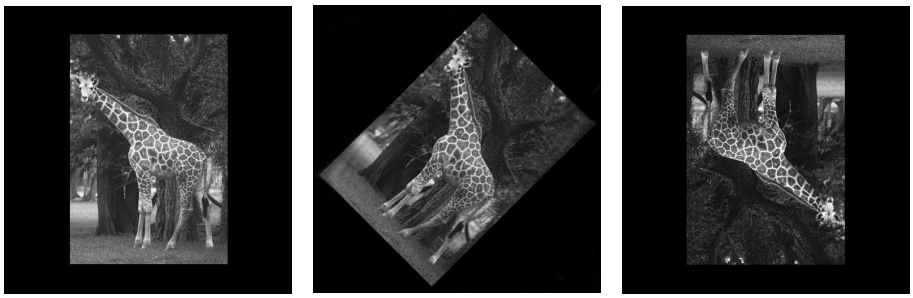

Figure 3.6: Numerical simulation of the image rotation system. Image (a) corresponds to the input image, $\theta = 0$. Output images (b) and (c) are obtained when the input image is transformed under the rotator operation at the angle $\theta = \pi/4$ and π, respectively.

as we mentioned. In contrast to lens-based systems, Dove prism introduces changes in the polarization state [108, 109] and diffraction effects that have to be compensated by using an imaging system.

3.3 Conclusions

In this chapter we have analyzed the optical implementation of the separable FRFT and rotator operation. This analysis brings us to the main setup properties that have to be considered for their experimental implementation. The transformation angle for the antisymmetric FRFT as well as for the rotator operation can be changed by the proper rotation of conventional cylindrical lenses. For arbitrary transformation angles, the separable FRFT can be achieved by a flexible setup where the lens power has to be adjusted. This setup can be implemented by using SLMs. As an example, different numerical simulations illustrating these transformations were considered and performed.

As mentioned, any ortho-symplectic system can be constructed from a separable FRFT one embedded between two rotator systems. Therefore this study, corresponding to their optical implementation, has a significant importance as being a pioneering proposal aiming to the performance of new relevant transformations.

Chapter 4

Properties of the gyrator transform

Many interesting applications based on first-order optical systems, have been proposed in the last two decades. Some of them, performing FRFT, are used for shift-variant filtering, noise reduction, and encryption [12]. Other ones serve as mode converters that permit to obtain the helicoidal vortex Laguerre-Gaussian (LG) mode after the propagation of the Hermite-Gaussian (HG) beam through these systems [98, 99, 110]. Besides LG modes, other stable modes carrying fractional orbital angular momentum [99, 111, 112] can be obtained by a generalized mode converter that can be described by the GT operation (called in [83, 84] as a cross-gyrator).

As we have demonstrated in chapter 2, GT can be performed in paraxial optics that allows its possible application for optical information processing, holography, beam characterization, mode conversion, quantum computing, etc. But in the contrast to the FRFT (see for example [12] and references there in), the GT operation is still little known for the optical community. Our goal is to establish the main properties of the GT that opens the perspective of its application for optical information processing together with FRFT.

The chapter starts introducing the GT operation, then its main properties as well as the GT of selected functions are studied in detail.

4.1 Definition of the gyrator transform

As mentioned in chapter 1, GT operation is mathematically defined as a linear canonical integral transform which produces the rotation in position−spatial frequency planes (x, q_y) and (y, q_x) [83, 84] of phase space. Thus the GT at parameter α (called below as a rotation angle) of a two-dimensional function $f_i(\mathbf{r}_i)$ associated in first-order optics with the complex field amplitude, can be written in the following form:

$$
\begin{aligned}
f_o(\mathbf{r}_o) = R^{\alpha}[f_i(\mathbf{r}_i)](\mathbf{r}_o) &= \iint f_i(x_i, y_i)\, K_{\alpha}(x_i, y_i, x_o, y_o)\, \mathrm{d}x_i \mathrm{d}y_i \\
&= \frac{1}{|\sin\alpha|} \iint f_i(x_i, y_i)\, \exp\left(i2\pi \frac{(x_o y_o + x_i y_i)\cos\alpha - (x_i y_o + x_o y_i)}{\sin\alpha} \right) \mathrm{d}x_i \mathrm{d}y_i, \qquad (4.1)
\end{aligned}
$$

where $\mathbf{r}_{i,o}^{t} = (x_{i,o}, y_{i,o})$ indicates the input and output dimensionless coordinates, respectively. Here t stands for transposition operation. For $\alpha = 0$ it corresponds to the identity transform, for $\alpha = \pi/2$ it reduces to the antisymmetric FRFT at transformation angle $\pi/2$ with rotation of the coordinates at $-\pi/2$, as it is derived from Eq. (1.23). For the transformation $\alpha = \pi$ the reverse transform described by the kernel $\delta(\mathbf{r}_o + \mathbf{r}_i)$ is obtained. For other angles α the kernel of the GT, $K_{\alpha}(x_i, y_i, x_o, y_o)$, has a hyperbolic phase structure that is shown in Fig. 4.1 for the angle $\alpha = \pi/4$ with output coordinates $x_o = y_o = 0$ [see Fig. 4.1(a)] and $2x_o = y_o = 1$ [see Fig. 4.1(b)].

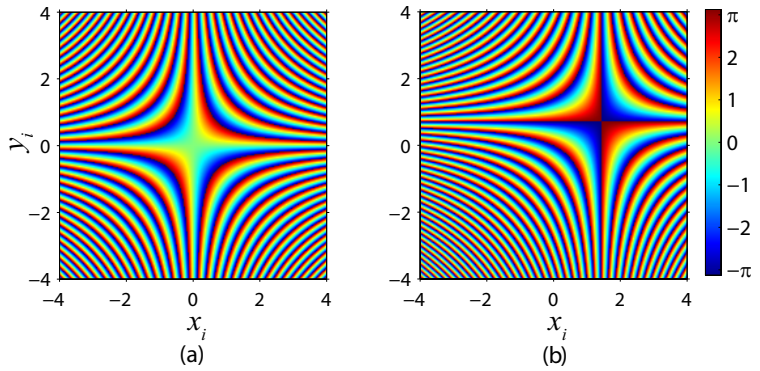

Figure 4.1: Graphical representation for the phase structure associated to the gyrator kernel for $\alpha = \pi/4$, $x_o = y_o = 0$ (a) and $2x_o = y_o = 1$ (b). These figures (a) and (b) correspond to the exponential argument of the kernel.

Let us remind that GT belongs to the class of the LCT Eq. (1.2) described by the orthogonal ray transformation matrix:

$$\mathbf{T}(\alpha) = \begin{bmatrix} \mathbf{X} & \mathbf{Y} \\ -\mathbf{Y} & \mathbf{X} \end{bmatrix}, \tag{4.2}$$

where

$$\mathbf{X} = \begin{bmatrix} \cos\alpha & 0 \\ 0 & \cos\alpha \end{bmatrix}, \quad \mathbf{Y} = \begin{bmatrix} 0 & \sin\alpha \\ \sin\alpha & 0 \end{bmatrix}. \tag{4.3}$$

The basis of the matrix formalism for first-order lossless optical systems led to a flexible system design for GT, chapter 2. This optical setup is constructed using three generalized lenses and two free-space intervals. The transformation angle α is changed by rotation of the cylindrical lenses which form the generalized lenses.

4.2 Basic properties

In order to work properly with the GT and to design the corresponding optical system for its experimental realization (chapter 6) we need to know its basic properties. As in the case of the Fourier transform (FT) or the FRFT [13] the main theorems such as scaling, shift, modulation, etc. have to be formulated. From the equations Eq. (4.1)−(4.3) it is easy to see that the GT is periodic and additive with respect to parameter α. This fact can be demonstrated directly by the multiplication of the ray transformation matrices that parameterized the kernel: $\mathbf{T}(\alpha)\,\mathbf{T}(\beta) = \mathbf{T}(\alpha+\beta)$. The inverse transformation corresponds to the GT at angle $-\alpha$. As it follows from Eq. (4.1) the inverse transform can be also written as

$$R^{-\alpha}[f_i(x_i, y_i)](x_o, y_o) = R^{\alpha}[f_i(-x_i, y_i)](-x_o, y_o), \tag{4.4}$$

and then $R^{\alpha}\left[R^{\alpha}[f_i(-x_i, y_i)](-x_o, y_o)\right](\mathbf{r}) = f_i(\mathbf{r})$.

It is known that the Parseval relation holds for entire class of the canonical integral transforms and therefore for the GT as well. As we show in Eq. (4.5), it is easy to demonstrate this relation

for the gyrator transform:

$$\begin{aligned}
&\int R^{\alpha}[f_i(\mathbf{r}_i)](\mathbf{r}_o)\,[R^{\alpha}[g_i(\mathbf{r}_e)](\mathbf{r}_o)]^{*}\,\mathrm{d}\mathbf{r}_o \\
&= \iint f_i(\mathbf{r}_i)\,\exp\left(i2\pi\frac{(x_o y_o + x_i y_i)\cos\alpha - (x_i y_o + x_o y_i)}{\sin\alpha}\right)\mathrm{d}\mathbf{r}_i \\
&\times \frac{1}{\sin^2\alpha}\int g_i^{*}(\mathbf{r}_e)\,\exp\left(i2\pi\frac{-(x_o y_o + x_e y_e)\cos\alpha + (x_e y_o + x_o y_e)}{\sin\alpha}\right)\mathrm{d}\mathbf{r}_e\mathrm{d}\mathbf{r}_o \\
&= \frac{1}{\sin^2\alpha}\int\int f_i(\mathbf{r}_i)\,g_i^{*}(\mathbf{r}_e)\exp\left(i2\pi\frac{(x_i y_i - x_e y_e)\cos\alpha}{\sin\alpha}\right) \\
&\times \int \exp\left(-i2\pi\frac{(x_i - x_e)y_o + x_o(y_i - y_e)}{\sin\alpha}\right)\mathrm{d}\mathbf{r}_o\mathrm{d}\mathbf{r}_i\,\mathrm{d}\mathbf{r}_e \\
&= \iint f_i(\mathbf{r}_i)\,g_i^{*}(\mathbf{r}_e)\exp\left(i2\pi\frac{(x_i y_i - x_e y_e)\cos\alpha}{\sin\alpha}\right)\delta(\mathbf{r}_i - \mathbf{r}_e)\mathrm{d}\mathbf{r}_i\,\mathrm{d}\mathbf{r}_e \\
&= \int f_i(\mathbf{r}_i)g_i(\mathbf{r}_i)^{*}\mathrm{d}\mathbf{r}_i. \qquad (4.5)
\end{aligned}$$

The shift of the input function $f_i(\mathbf{r})$ at vector $\mathbf{v}^t = (v_x, v_y)$, leads to the shift of its GT (for the angle α) at $\mathbf{v}\cos\alpha$ with an additional linear phase modulation:

$$R^{\alpha}[f_i(\mathbf{r}_i - \mathbf{v})](\mathbf{r}_o) = \exp\left(i\pi[v_x v_y \sin 2\alpha - 2\mathbf{r}_o^t\widetilde{\mathbf{v}}\sin\alpha]\right)R^{\alpha}[f_i(\mathbf{r}_i)](\mathbf{r}_o - \mathbf{v}\cos\alpha), \qquad (4.6)$$

where $\widetilde{\mathbf{v}}^t = (v_y, v_x)$, see appendix B for more details. From the latter equation we observe that the shift of the amplitude for the GT, $\left|R^{\alpha}[f_i(\mathbf{r}_i - \mathbf{v})](\mathbf{r}_o)\right| = \left|R^{\alpha}[f_i(\mathbf{r}_i)](\mathbf{r}_o - \mathbf{v}\cos\alpha)\right|$, is the same as for the case of two-dimensional symmetric FRFT at angle α [13].

The effect of plane wave modulation $\exp(-i2\pi\mathbf{k}^t\mathbf{r}_i)$ of the function $f_i(\mathbf{r}_i)$ under the GT action is also similar to the FRFT case. It leads to the shift of its GT (for the angle α) at $-\widetilde{\mathbf{k}}\sin\alpha$ and an additional linear phase modulation:

$$R^{\alpha}\left[f_i(\mathbf{r}_i)\exp\left(-i2\pi\mathbf{k}^t\mathbf{r}_i\right)\right](\mathbf{r}_o) = \exp\left(-i\pi[k_x k_y \sin 2\alpha + 2\mathbf{k}^t\mathbf{r}_o\cos\alpha]\right)R^{\alpha}\left[f_i(\mathbf{r}_i)\right]\left(\mathbf{r}_o + \widetilde{\mathbf{k}}\sin\alpha\right), \quad (4.7)$$

where $\mathbf{k}^t = (k_x, k_y)$ and $\widetilde{\mathbf{k}}^t = (k_y, k_x)$.

Scaling theorem is formulated in the following form (see appendix B):

$$R^{\alpha}[f_i(\mathbf{S}\mathbf{r}_i)](\mathbf{r}_o) = \frac{\sigma_\beta\cos\beta}{\sigma_\alpha\cos\alpha}\exp\left(i2\pi x_o y_o\left(1 - \left(\frac{\cos\beta}{\cos\alpha}\right)^2\right)\cot\alpha\right)R^{\beta}[f_i(\mathbf{r}_i)]\left(\frac{\cos\beta}{\cos\alpha}\mathbf{S}\mathbf{r}_o\right), \qquad (4.8)$$

where $\sigma_\alpha = \mathrm{sgn}(\sin\alpha)$, $\sigma_\beta = \mathrm{sgn}(\sin\beta)$,

$$\mathbf{S} = \begin{bmatrix} s_x & 0 \\ 0 & s_y \end{bmatrix} \text{ and } \cot\beta = \frac{\cot\alpha}{s_x s_y}. \qquad (4.9)$$

It means that the GT at angle α of the scaled function $f_i(\mathbf{S}\mathbf{r}_i)$ corresponds to the GT at angle β of the initial function $f_i(\mathbf{r}_i)$ with additional scaling of the output coordinates and hyperbolic phase modulation.

The scaling property for the GT is similar to one for the Fresnel transform or for the FRFT. Indeed, during the Fresnel diffraction the change of the aperture scale leads to the observation of the same diffraction pattern (except of the corresponding scaling and chirp phase modulation) at another propagation distance. The main difference is in the phase modulation that has a

hyperbolic form for the GT and a chirp form for Fresnel or FRFT transforms. Therefore two particular cases corresponding to scaling parameters $s_x = s = s_y^{-1}$ and $s_x = s = -s_y^{-1}$, in which the expression Eq. (4.8) is significantly reduced. Thus if $s_x = s = s_y^{-1}$ the scaling does not change the transformation angle $\beta = \alpha$, the output scaling is the same as the input one and there is no additional phase modulation:

$$R^{\alpha}[f_i(x_i s, y_i s^{-1})](\mathbf{r}_o) = R^{\alpha}[f_i(\mathbf{r}_i)](x_o s, y_o s^{-1}). \tag{4.10}$$

This scaling property will be demonstrated in section 5.1.2 as application to generation of elliptical vortex beams [113].

For the case $s_x = s = -s_y^{-1}$ the angle relation Eq. (4.9) reduces to $\cot\beta = -\cot\alpha$ (therefore $\beta = \pi - \alpha$), and Eq. (4.8) can be written as

$$R^{\alpha}[f_i(x_i s, -y_i s^{-1})](\mathbf{r}_o) = R^{\pi-\alpha}[f_i(\mathbf{r}_i)]\left(-x_o s, s^{-1} y_o\right), \tag{4.11}$$

or using the additive property of the GT as

$$R^{\alpha}[f_i(x_i s, -y_i s^{-1})](\mathbf{r}_o) = R^{-\alpha}[f_i(\mathbf{r}_i)]\left(x_o s, -s^{-1} y_o\right). \tag{4.12}$$

In particular when the scaling parameter is set at $s = 1$ we obtain an expression similar to Eq. (4.4):

$$R^{\alpha}[f_i(x_i, -y_i)](\mathbf{r}_o) = R^{-\alpha}[f_i(\mathbf{r}_i)]\left(x_o, -y_o\right), \tag{4.13}$$

which turns out to be an inverse transformation.

4.3 Gyrator transform of selected functions

As in the well-known case of the Fourier transform, the GT of only some selected functions can be expressed analytically. The fundamental functions: Dirac delta, 1, hyperbolic wave, plane wave, spherical wave, Gaussian and Hermite-Gaussian mode and their corresponding GTs are displayed in Table 4.3. The following notations are used along this Table: shift vector $\mathbf{v}^t = \left(v_x, v_y\right)$, wavevector $\mathbf{k}^t = 2\pi\left(k_x, k_y\right)$, $a > 0$, b and c are real numbers, and $\mathfrak{R}^{-\frac{\pi}{4}}$ is the operator for coordinate rotation at angle $-\pi/4$.

Let us consider in detail some particular cases from Table 4.3 (see appendix B for intermediate calculations). The first row of Table 4.3 shows that the GT for $\delta(\mathbf{r}_i - \mathbf{v})$ corresponds to the gyrator kernel as the output function, $K_{\alpha}(\mathbf{r}_i = \mathbf{v}, \mathbf{r}_o)$, and therefore to product of hyperbolic and plane waves. Correspondingly the GT of a hyperbolic wave (see row 2, Table 4.3) transforms to Dirac delta function for angle such that $\cot\alpha = -c$. This is an important result because it means that GT can be used for localization of waves with hyperbolic phase front. For $c = \tan\alpha$ the plane wavefront, $f_o(\mathbf{r}_o) = |\sin\alpha|^{-1}$, is obtained at the output of the GT system. For other angles the hyperbolic wave transforms to the hyperbolic one. We underline only two particular cases, when the expressions for the GT of hyperbolic wave are simplified. Thus for the values of parameter $c = \cot\alpha$ and $c = (1 + \cot\alpha) / (\cot\alpha - 1)$ we obtain $f_o(\mathbf{r}_o) = \exp\left(i\pi\left(\cot\alpha - \tan\alpha\right) x_o y_o\right) / |\sin\alpha|$ and $f_o(\mathbf{r}_o) = \exp\left(i2\pi x_o y_o\right) / |\sin\alpha|$, respectively. Note that for $c = 0$, and hence $f_i(\mathbf{r}_i) = 1$, its GT also corresponds to a hyperbolic wavefront as it is indicated at the third row of the Table 4.3.

$f_i(\mathbf{r}_i)$	$f_o(\mathbf{r}_o) = R^{\alpha}[f_i(\mathbf{r}_i)](\mathbf{r}_o)$
$\delta(\mathbf{r}_i - \mathbf{v})$	$\frac{1}{\lvert\sin\alpha\rvert}\exp\left(i2\pi\frac{\left(x_o y_o + v_x v_y\right)\cos\alpha - \left(v_x y_o + x_o v_y\right)}{\sin\alpha}\right)$
$\exp\left(i2\pi c x_i y_i\right)$	$\frac{1}{\lvert\sin\alpha\rvert}\exp\left(i2\pi\frac{c\cot\alpha - 1}{c + \cot\alpha}x_o y_o\right),\ (c \neq -\cot\alpha)$
1	$\frac{1}{\lvert\sin\alpha\rvert}\exp\left(-i2\pi x_o y_o\tan\alpha\right)$
$\exp\left(-i\mathbf{k}^t\mathbf{r}_i\right)$	$\frac{1}{\lvert\sin\alpha\rvert}\exp\left(-i2\pi\left(x_o y_o + k_x k_y\right)\tan\alpha\right)\exp\left(-\frac{i}{\cos\alpha}\mathbf{k}^t\mathbf{r}_o\right)$
$\exp\left(-i\pi b\mathbf{r}_i^2\right)$	$\frac{1}{\sqrt{\cos^2\alpha - b^2\sin^2\alpha}}\exp\left(-i\pi\frac{\left(1+b^2\right)\sin 2\alpha}{\cos^2\alpha - b^2\sin^2\alpha}x_o y_o\right)\exp\left(\frac{-i\pi b\mathbf{r}_o^2}{\cos^2\alpha - b^2\sin^2\alpha}\right)$
$\exp\left(-\pi a\mathbf{r}_i^2\right)$	$\frac{1}{\sqrt{\cos^2\alpha + a^2\sin^2\alpha}}\exp\left(i\pi\frac{\left(a^2-1\right)\sin 2\alpha}{\cos^2\alpha + a^2\sin^2\alpha}x_o y_o\right)\exp\left(\frac{-\pi a\mathbf{r}_o^2}{\cos^2\alpha + a^2\sin^2\alpha}\right)$
$\mathrm{HG}_{m,n}\left(\mathfrak{R}^{-\frac{\pi}{4}}\mathbf{r}_i; 1\right)$	$e^{i\alpha(n-m)}\mathrm{HG}_{m,n}\left(\mathfrak{R}^{-\frac{\pi}{4}}\mathbf{r}_o; 1\right)$

Table 4.3. Selected functions and their gyrator transforms

The gyrator transform of a plane wave (row 4, Table 4.3) corresponds to a product of the plane wave, with spatial frequency scaled by $1/\cos\alpha$ and the hyperbolic wave. For the spherical wavefront (row 5, Table 4.3) its GT corresponds to a product of the spherical wave, affected by the scaling factor and the hyperbolic wave. The hyperbolic contribution cancels for angles corresponding to $\alpha = 0$ and $\alpha = \pi/2$: $f_o(\mathbf{r}_o) = \exp\left(i\pi\mathbf{r}_o^2/b\right)/ib$ and $f_o(\mathbf{r}_o) = \exp\left(-i\pi b\mathbf{r}_o^2\right)$ for $\alpha = \pi(2n+1)/2$ and $\alpha = \pi n$ (where n is an integer), correspondingly.

The GT of a Gaussian function (row 6, Table 4.3) corresponds to the Gaussian function with hyperbolic phase modulation. For the case $a = 1$ the additional phase shift vanishes and output function corresponds to the input function $\exp\left(-\pi\mathbf{r}_o^2\right)$. This result indicates that $\exp\left(-\pi\mathbf{r}_o^2\right)$ is an eigenfunction of the GT for any transformation angle α. As we have mentioned in the previous chapter, the GT at angle α can be represented as a FRFT at angles $(\alpha, -\alpha)$ with rotation of the input and output coordinates $\mathbf{r}_o$ at $\pi/4$ and $-\pi/4$, correspondingly. Thus the eigenfunctions for the GT are the eigenfunctions of the FRFT rotated at angle $-\pi/4$, see reference [114].

The Hermite-Gaussian modes:

$$\mathrm{HG}_{m,n}(\mathbf{r}; w) = 2^{1/2}\frac{H_m\left(\sqrt{2\pi}\frac{x}{w}\right)H_n\left(\sqrt{2\pi}\frac{y}{w}\right)}{\sqrt{2^m m!w}\,\sqrt{2^n n!w}}\exp\left(-\frac{\pi}{w^2}\mathbf{r}^2\right), \tag{4.14}$$

where H_m is the Hermite polynomial and w is the beam waist, form the complete orthogonal set of eigenfunctions for the separable FRFT ($w = 1$). In Fig. 4.2 (a) and (c) the $\mathrm{HG}_{1,0}$ and $\mathrm{HG}_{3,1}$ are displayed, respectively. Therefore the HG modes rotated at $-\pi/4$ form the set of the orthogonal eigenfunctions for the GT (row 7, Table 4.3). Notice that for $\alpha = \pm\pi/4$ the kernel of the GT is reduced to

$$K_{\pm\pi/4}(x_i, y_i, x_o, y_o) = \sqrt{2}\exp\left(\pm i2\pi\left[x_o y_o + x_i y_i - \sqrt{2}\left(x_i y_o + x_o y_i\right)\right]\right). \tag{4.15}$$

Moreover, $\mathrm{HG}_{m,n}(\mathbf{r}; w)$ mode for $w = 1$ transforms under the GT at angles $\alpha = \pm\pi/4$ into the helicoidal LG mode [99, 112]:

$$\mathrm{LG}_{p,l}^{\pm}(\mathbf{r}; w) = w^{-1}\sqrt{\frac{\min(m,n)!}{\max(m,n)!}}\left(\sqrt{2\pi}\left(\frac{x}{w} \pm i\frac{y}{w}\right)\right)^l L_p^l\left(\frac{2\pi}{w^2}\mathbf{r}^2\right)\exp\left(-\frac{\pi}{w^2}\mathbf{r}^2\right), \tag{4.16}$$

where L_p^l is the Laguerre polynomial, $p = \min(m,n)$ and $l = |m-n|$. The topological charge $\pm l$ corresponds to the phase variation (in units of 2π) of the field along a loop encircling the optical axis, where the sign $-$ corresponds to clockwise circulation.

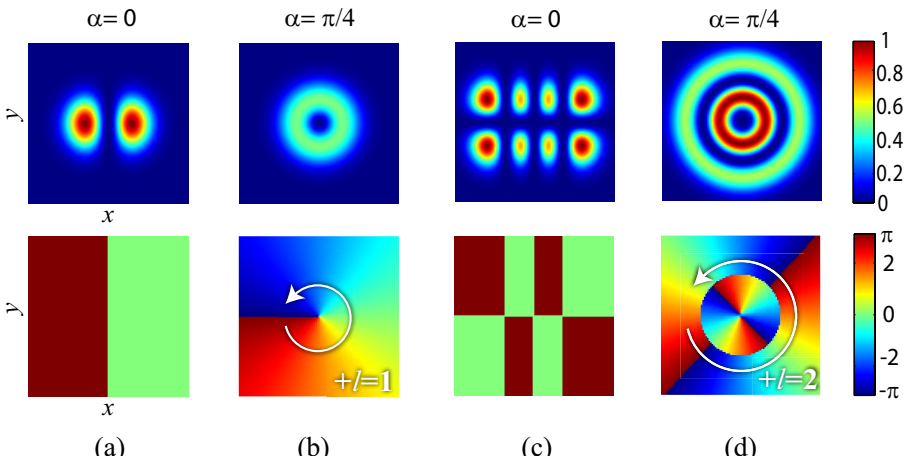

Figure 4.2: Intensity (up row) and phase (low row) distribution of the GT of $HG_{1,0}$(a) and $HG_{3,1}$(c), into $LG^{+}_{0,1}$ (b) and $LG^{+}_{1,2}$ (d), correspondingly. Note that transformation angle $\alpha = 0$ corresponds to the identity transformation. The phase distribution of the LG mode corresponds to a helicoidal structure, where the phase singularity introduces a dark hole (zero intensity) in the center of the mode. In this case the topological charge is $+l$ with $l = 1$ and $l = 2$ phase singularities (number of twists) for the case (b) and (d), respectively.

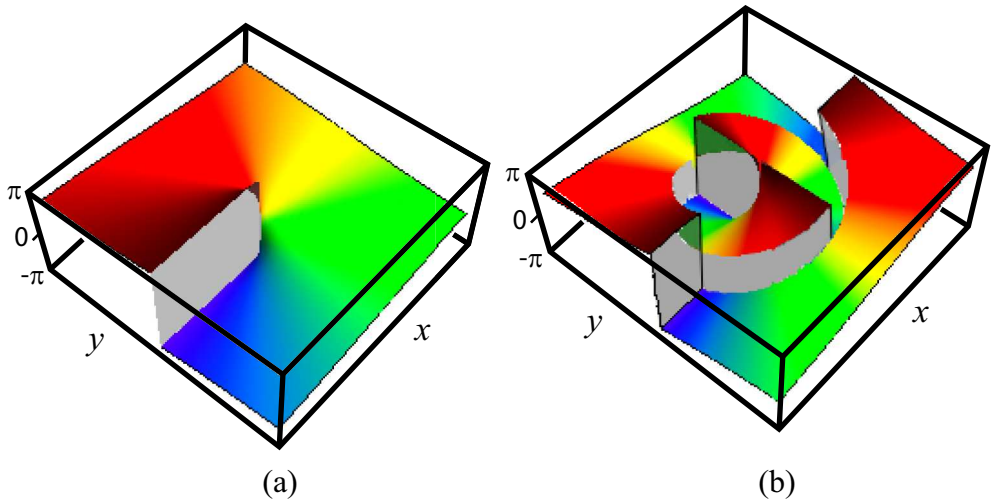

Figure 4.3: The 3D graphical representation for the phase distribution corresponding to $LG^{+}_{0,1}$ and $LG^{+}_{1,2}$, (a) and (b) respectively. The helicoidal structure reveals the phase dislocations associated to $l = 1$ and $l = 2$, which can be also seen in Fig. 4.2.

As an example, the mode transformation of HG into the LG is displayed in Fig. 4.2 for the case $HG_{1,0}$ (a) and $HG_{3,1}$ (c). The phase distribution associated to $LG^{+}_{0,1}$ and $LG^{+}_{1,2}$ is displayed in Fig. 4.2 (b) and (d), respectively. A 3D graphical representation of the phase distribution associated to these LG modes, is displayed in Fig. 4.3.

The LG mode with $l \neq 0$ is an optical vortex [115, 116] that looks as a set of $p+1$ concentric rings with a dark hole in the center. Moreover, the LG mode mode carry an orbital angular momentum (OAM) $\pm l\hbar$ per photon [117, 118]. Nowadays, LG modes are commonly used in relevant fields such as quantum computing [119], optical particle micromanipulation (trapping) [120], phase contrast imaging [121], etc. We consider LG modes as an example in order to demonstrate the GT action. In general, optical vortices have had a strong impact in different research fields.

Intermediate modes, also known as gyrating modes [112], are obtained when we apply the GT to the HG modes for the rest of transformation angles. This we will be demonstrated in the next chapter. Thus GT can be understood as a tunable generalized mode converter. In contrast to other systems performing mode conversion [99, 110], GT does not introduce additional rotation into the signal. In addition, as it follows from Eq. (4.4) and Eq. (4.11), for the transformation angle $\alpha = 3\pi/4, 5\pi/4$ the $HG_{m,n}(\mathbf{r};1)$ mode transforms to $-LG^{-}_{p,l}(\mathbf{r};1)$ and $-LG^{+}_{p,l}(\mathbf{r};1)$, respectively. Note that both mode types, LG and HG mode, are stable during its free-space propagation.

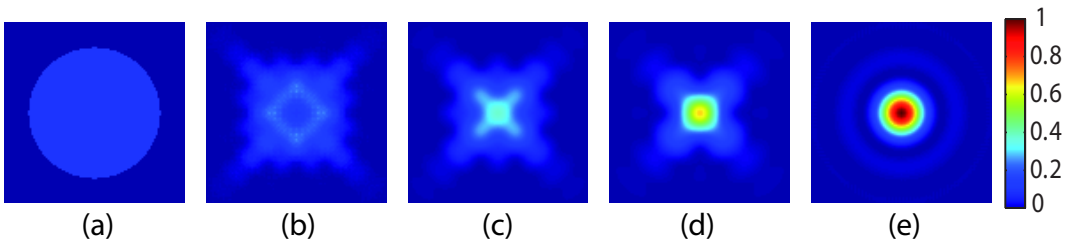

Figure 4.4: Intensity distributions corresponding to the GT of the circle function are displayed for different transformation angles $\alpha = 0$ (a), $7\pi/36$ (b), $\pi/4$ (c), $11\pi/36$ (d), and $\pi/2$ (e). Note that for $\alpha = \pi/2$ the antisymmetric FRFT at transformation angle $\pi/2$ with rotation of the coordinates at $-\pi/2$ is obtained.

Interesting results are also found when periodic functions are transformed under the GT action. It is well-known that a periodic function $f_i(\mathbf{r}_i)$ with periods k_x^{-1}, k_y^{-1} can be represented as a Fourier expansion

$$f_i(\mathbf{r}_i) = \sum_{n,m} a_{n,m} \exp\left(-i2\pi\left(x_i k_x n + y_i k_y m\right)\right). \tag{4.17}$$

Then the GT of a periodic function can be written as follows:

$$f_o(\mathbf{r}_o) = R^{\alpha}[f_i(\mathbf{r}_i)](\mathbf{r}_o) = \sum_{n,m} a_{n,m} R^{\alpha}\left[\exp\left(-i2\pi\left(x_i k_x n + y_i k_y m\right)\right)\right](\mathbf{r}_o). \tag{4.18}$$

Using the expression for the GT of a plane wave (row 4, Table 4.3) we derive that

$$\begin{aligned} f_o(\mathbf{r}_o) \quad = \quad & \frac{\exp\left(-i2\pi x_o y_o \tan\alpha\right)}{|\sin\alpha|} \\ & \times \sum_{n,m} a_{n,m} \exp\left(-i2\pi n m k_x k_y \tan\alpha\right) \exp\left(-i2\pi \frac{n k_x x_o + m k_y y_o}{\cos\alpha}\right). \end{aligned} \tag{4.19}$$

Thus for angles which satisfy the relation $l = k_x k_y \tan\alpha_l$, where l is an integer, the Eq. (4.19) is reduced to

$$f_o(\mathbf{r}_o) = \frac{\exp\left(-i2\pi x_o y_o \tan\alpha_l\right)}{|\sin\alpha_l|}\, f_i\left(\mathbf{r}_o/\cos\alpha_l\right), \tag{4.20}$$

which can be considered as a Talbot effect [102] for the gyrator transform. In contrast to the conventional Talbot effect, the latter expression corresponds to the input function (with scaling $1/\cos\alpha_l$) modulated by the hyperbolic wave $\exp\left(-i2\pi x_o y_o \tan\alpha_l\right)/|\sin\alpha_l|$.

Finally as an example, Fig. 4.4 shows the squared moduli (intensity distribution in the case of optical realization) of the GT for the circle function $\mathrm{circ}(\mathbf{r}_i/\rho)$ (with $\rho = 1.6$) for different transformation angles: $\alpha = 0$, $7\pi/36$, $\pi/4$, $11\pi/36$, and $\pi/2$, (a)–(e) respectively. This image sequence demonstrates the evolution from the input function Fig. 4.4(a) to its rotated Fourier transform obtained for $\alpha = \pi/2$, Fig. 4.4(e). We observe how the rotational symmetry in the position ($\alpha = 0$) and FT domain ($\alpha = \pi/2$) changes to the rectangular one for other angles.

4.4 Conclusions

The main properties of the GT such as shift, scaling, plane wave modulation, Parseval theorem, and other relevant properties have been formulated. The GT of the selected functions have been found. Gyrator operation promises to be a useful tool in image processing, holography, beam characterization, quantum information, new mode generation, etc. The results presented in this chapter were reported in [122].

Chapter 5

Applications of the gyrator transform

In this chapter we study the application of the GT operation as a tunable optical mode converter and for image processing: noise reduction, filtering and encryption. As mentioned, fractional transformations such as FRFT have been used for signal processing tasks such as space-variant filtering, noise reduction, watermarking, encryption, etc. The above mentioned properties of the GT make it a useful tool for optical information processing. Indeed, GT provides an image representation in a new phase-space domain which was not explored yet for signal analysis and synthesis. For instance, it can be used for hyperbolic wave detection, shift-variant filtering, encryption, beam characterization, and generation of stable modes with specific properties.

The numerical simulation of the GT setup has been implemented in order to illustrate these applications. The numerical approach is based on the Fresnel integral calculation (see appendix A) and phase modulation functions that correspond to free-space intervals and generalized lenses, respectively. This algorithm has the same complexity as the one for the FRFT [12].

5.1 Gyrator transform as optical mode converter

Here we will consider the mode transformation under the GT, in particular for the case of Hermite-Gaussian modes. There is a double interest to these modes. First of all they appear as natural modes in laser resonators with rectangular symmetry and propagating in free-space without changing their spatial intensity distribution. On the other hand the HG modes form a complete orthonormal set and therefore are often used as a basis for image representation. The GT of the HG modes generates other stable modes, that also propagate in free-space without changing their intensity distribution, and thus the knowledge of these modes allows to represent any image in the corresponding GT domain.

5.1.1 Hermite-Gaussian mode evolution under the gyrator transform

Let us first consider the evolution of the HG mode, Eq. (4.14), under the GT. As we have demonstrated in chapter 2, the GT for different transformation angles can be performed by an optical system constructed by using three generalized lenses (assembled set of cylindrical lenses) and two fixed free-space intervals. Then the numerical simulations of the GT can follow this recipe. Note that while the free-space propagation implies the Fresnel diffraction integral calculation, phase modulation functions are associated to the generalized lenses. Details about the algorithm used for the Fresnel integral calculation are found in appendix A. This approach

allows to realize a fast an accurate numerical simulation of the GT. The parameters used in these numerical simulations are the following: wavelength $\lambda = 532$ nm, $w = 0.73$ mm, and spatial resolution of 20 μm.

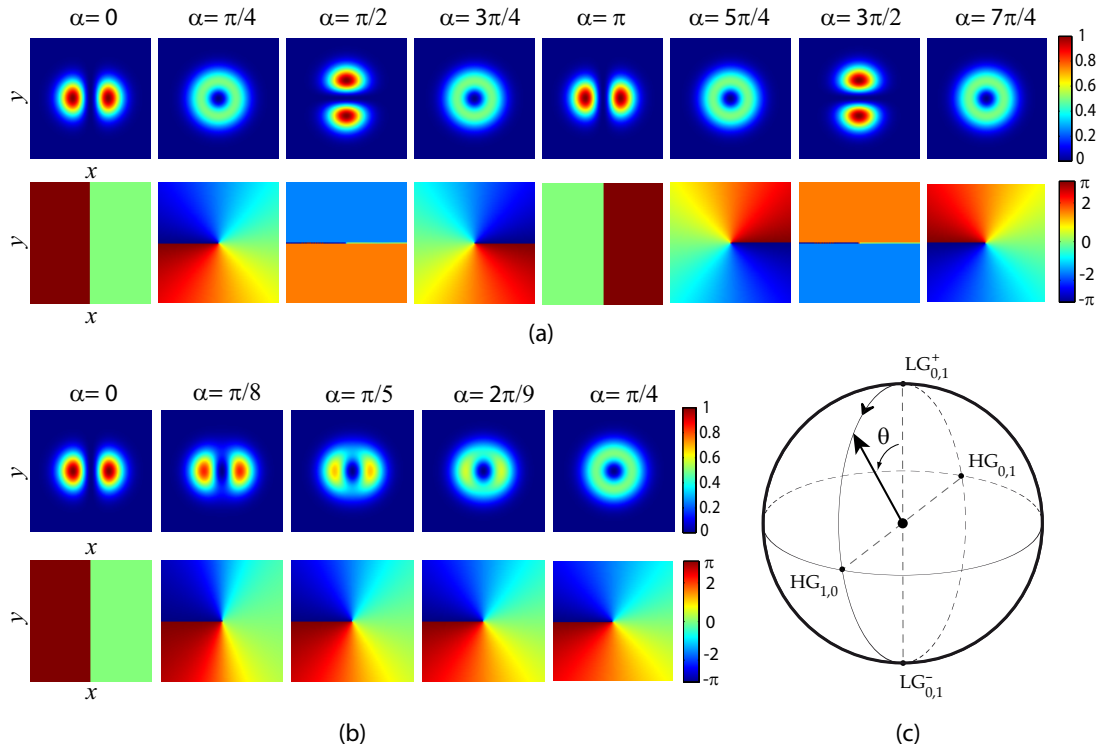

Figure 5.1: Intensity (up row) and phase (low row) of the GT of $HG_{1,0}$ mode for different angles α. Figure (a) corresponds to transformation angle $\alpha = 0, \pi/4, \pi/2, 3\pi/4, \pi, 5\pi/4, 3\pi/2, 7\pi/4$. (b) Intermediate modes for angles between $\alpha = 0$ and $\alpha = \pi/4$ are displayed. The GT operation is associated with the movement along the main meridian of the orbital Poincaré sphere, which is schematized in (c) for the case $HG_{1,0}$. Note that $\theta = 2\alpha + \pi/2$.

During last decade various optical schemes were proposed for the generation of the vortex beams which carry OAM. Mostly the conversion of Hermite-Gaussian modes of different orders ($HG_{m,n}$) to the helicoidal Laguerre-Gaussian ($LG_{p,l}$) ones were considered [98]. It was also shown that it is possible to generate the stable modes with fractional OAM [99, 111]. In contrast to other optical mode converters, the GT can be seen as a tunable and flexible mode converter able to generate intermediate modes with fractional OAM: $L_z = l\hbar \sin 2\alpha$, [112]. In the previous chapter, we mentioned that the mode conversion of $HG_{m,n}$ into $LG_{p,l}$ is achieved under the GT action when $\alpha = \pi/4 + n\pi/2$ (n integer) whereas intermediate modes are obtained for the rest of angle values if $\alpha \neq \pi n/2$. In Fig. 5.1 the mode conversion from $HG_{m=1,\ n=0}$ mode to helicoidal $LG_{p=0,\ l=1}$ is displayed for different values of angle α. The first and the second rows correspond to the intensity and phase distribution, respectively. Note that the intensity distribution is normalized to the maximum intensity value of the input signal ($\alpha = 0$), and phase values are represented for $[-\pi, \pi]$ region. Mode conversion from $HG_{1,0}$ ($\alpha = 0$) to $LG^{\pm}_{0,1}$ is obtained for $\alpha = \pi/4,\ 3\pi/4,\ 5\pi/4, 7\pi/4$, as it has been explained in the latter chapter. For $\alpha = \pi/2,\ \pi,\ 3\pi/2$ the output mode corresponds to $HG_{1,0}$ rotated at $\pi/2,\ \pi, 3\pi/2$ with an additional phase shift $\exp(i2\alpha)$, correspondingly. Therefore the mode conversion from $HG_{1,0}$ to $HG_{0,1}$ is obtained for $\alpha = \pi/2,\ 3\pi/2$.

In Fig. 5.1(b) the intermediate modes obtained by the GT of $HG_{1,0}$ for $\alpha \in (0,\ \pi/4)$ are

displayed. The modes corresponding to every particular angle are stable and possess fractional OAM, [111, 112]. In general the action of the GT operation is associated with the movement along the main meridian of the orbital Poincaré sphere [111], see Fig. 5.1(c).

5.1.2 Influence of scaling and shift properties to mode transformation

Let us now consider how the scaling of the input HG mode affects on the mode generation. Based on the scaling theorem Eq. (4.8), and choosing scaling parameters $s_x = s = s_y^{-1}$ in order to avoid the change of the transformation angle and additional phase modulation, we observe (see Fig. 5.2) that for $\alpha = \pi/4$ the transformation of the rotational symmetric intensity distribution typical for the LG mode into elliptical one Fig. 5.2 (c) and (f). Figures 5.2 (a) and (d) correspond to the input signal $HG_{1,0}$ scaled by $s = 1/2$ and $s = 2$, respectively. Figures 5.2 (b), (c), (e), and (f) are the corresponding output modes for $\alpha = \pi/5$ and $\alpha = \pi/4$. Therefore the GT of scaled HG mode is an alternative for generation of the elliptic LG beams [113].

When the input function is not centered at the optical axis we can apply the shifting theorem, Eq. (4.6), to obtain the output function. Notice that if the input signal is shifted at $\mathbf{v}^t = (v_x, v_y)$ the output signal is shifted at $\mathbf{v}^t \cos\alpha$ and affected by an additional linear phase modulation. The GT at angle $\alpha = \pi/5$ and $\alpha = \pi/4$ of $HG_{1,0}$ for different shifting parameters is displayed in Fig. 5.3. Figures 5.3 (b), (c), (e), and (f) are the output modes obtained from the $HG_{1,0}$ mode shifted by $\mathbf{v}^t = (1\text{ mm}, 0)$ [Fig. 5.3(a)] and $\mathbf{v}^t = (1\text{ mm}, -1\text{ mm})$ [Fig. 5.3(c)], correspondingly.

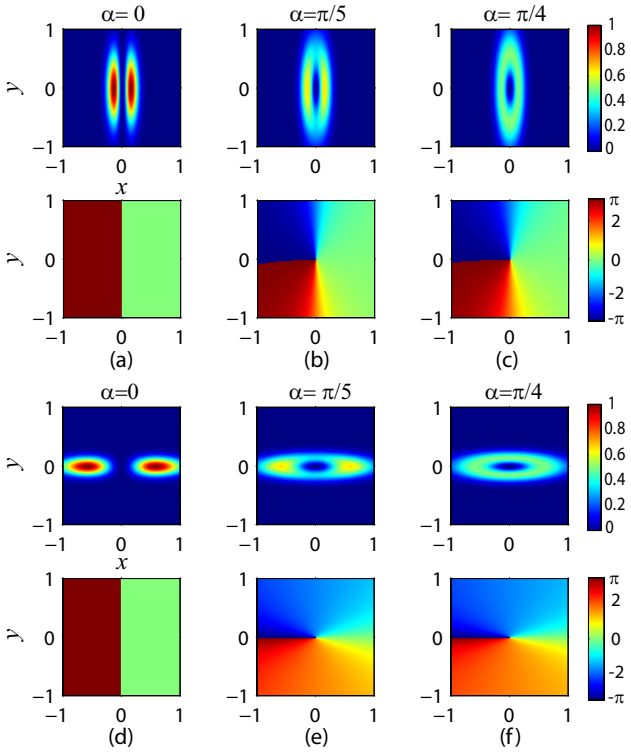

Figure 5.2: Intensity (up row) and phase (low row) for different angles of the GT of $HG_{1,0}$ affected by scaling factors $s_x = s = s_y^{-1}$: $s = 1/2$ (a, b, c) and $s = 2$ (d, e ,f), respectively.

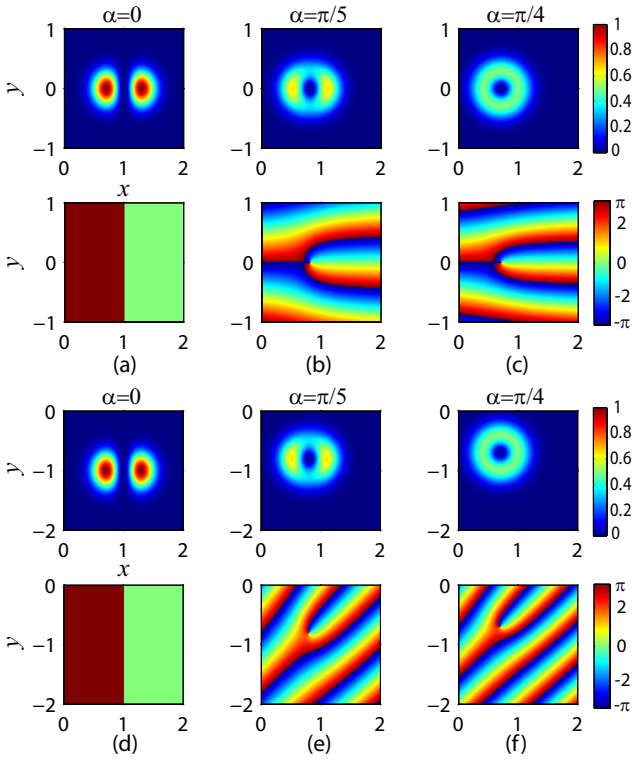

Figure 5.3: Intensity (up row) and phase (low row) of the GT (for the angle α) of $HG_{1,0}$ mode shifted by $\mathbf{v}^t = (1mm, 0)$ (a, b, c) and $\mathbf{v}^t = (1mm, -1mm)$ (d, e, f).

5.1.3 Gyrator transform of HG modes composition

Up till now we have considered the transformation of only one type of HG modes. Nevertheless the composition of HG modes of the same order ($n + m$ =const) also produces a stable mode configuration after gyrator transformation.

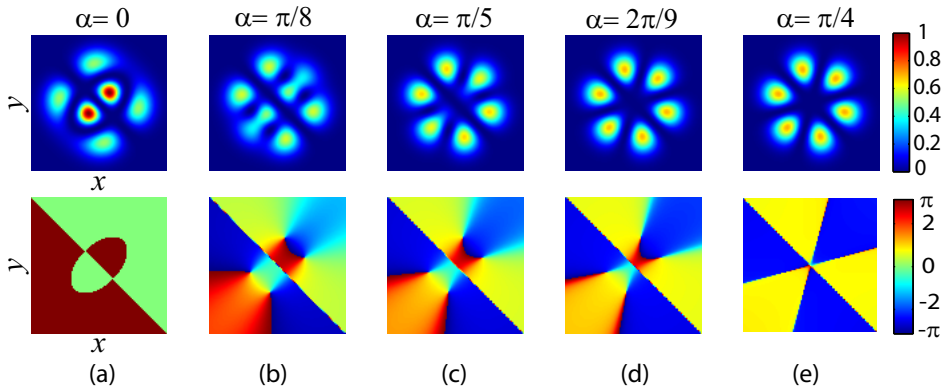

Figure 5.4: Intensity (up row) and phase (low row) distributions for GT of the $HG_{3,0}$ + $HG_{0,3}$ input mode are displayed for different angles α = 0 (input mode), $\pi/8$, $\pi/5$, $2\pi/9$, $\pi/4$ ($LG^{+}_{0,3}$ + $LG^{-}_{0,3}$ mode).

Thus for example the combination $HG_{3,0} + HG_{0,3}$ [Fig. 5.4(a)] leads for $\alpha = \pi/4$ to the odd Laguerre-Gaussian beams, which is the sum of two helicoidal LG modes with opposite OAM values: $LG^{+}_{0,3} + LG^{-}_{0,3}$ [Fig. 5.4(e)]. For other angles $\alpha = \pi/8,\ \pi/5,\ 2\pi/9$ the intermediate modes are obtained [Fig. 5.4 (b)−(d)].

5.2 Filtering in gyrator domain

One of the main goals of the signal processing is to recover useful information concerning to an object from the related signal. The encoded information may be partially localized or spread over the entire signal domain. It may be represented by a specific pattern, which has to be detected, or may be hidden due to the noise that has to be eliminated. Therefore the signal processing methods need to be adjusted to the specific tasks and signal characteristics.

In contrast to the FRFT, the GT can only be applied for two-dimensional signals, as we can see from Eq. (4.1). Therefore here we will analyze the GT of two-dimensional real signals (images). Since the kernel of the GT is a complex function we first need to analyze the information associated to the GT spectrum (phase and the amplitude distribution) for different angles. Notice that the angle range can be reduced to $[0, \pi/2]$ since for the real signals $f_i(\mathbf{r}_i)$ we have the following relations

$$R^{-\alpha}[f_i(\mathbf{r}_i)](\mathbf{r}_o) = \left[R^{\alpha}[f_i(\mathbf{r}_i)](\mathbf{r}_o)\right]^{*}, \tag{5.1}$$

$$R^{\pi-\alpha}[f_i(\mathbf{r}_i)](\mathbf{r}_o) = \left[R^{\alpha}[f_i(\mathbf{r}_i)](-\mathbf{r}_o)\right]^{*}. \tag{5.2}$$

The GT at $\alpha = 0$ and at $\alpha = \pi/2$ will be further mentioned as image and Fourier domains respectively.

In our case the test image, $f_i(x_i, y_i)$ input function, corresponds to Lena picture of 256×256 pixels Fig. 5.5, embedded on a square empty matrix with 1024×1024 points (numerical window size).

Figure 5.5: Test image corresponding to Lena picture with 256×256 pixels.

To begin, let us consider the reconstruction of the test image from phase-only or amplitude-only components of its GT for different angles α. Thus if we introduce the following notation

$$R^{\alpha}[f_i(\mathbf{r}_i)](\mathbf{r}_o) = F_{\alpha}(\mathbf{r}_o)\exp(i\varphi_{\alpha}(\mathbf{r}_o)), \tag{5.3}$$

where $F_{\alpha}(\mathbf{r}_o) > 0$ is the amplitude, and $\varphi_{\alpha}(\mathbf{r}_o)$ is the phase distribution corresponding to field transformed under GT action at angle α, the considered operations are expressed as $R^{-\alpha}[F_{\alpha}(\mathbf{r}_o)](\mathbf{r})$ and $R^{-\alpha}[\exp(i\varphi_{\alpha}(\mathbf{r}_o))](\mathbf{r})$.

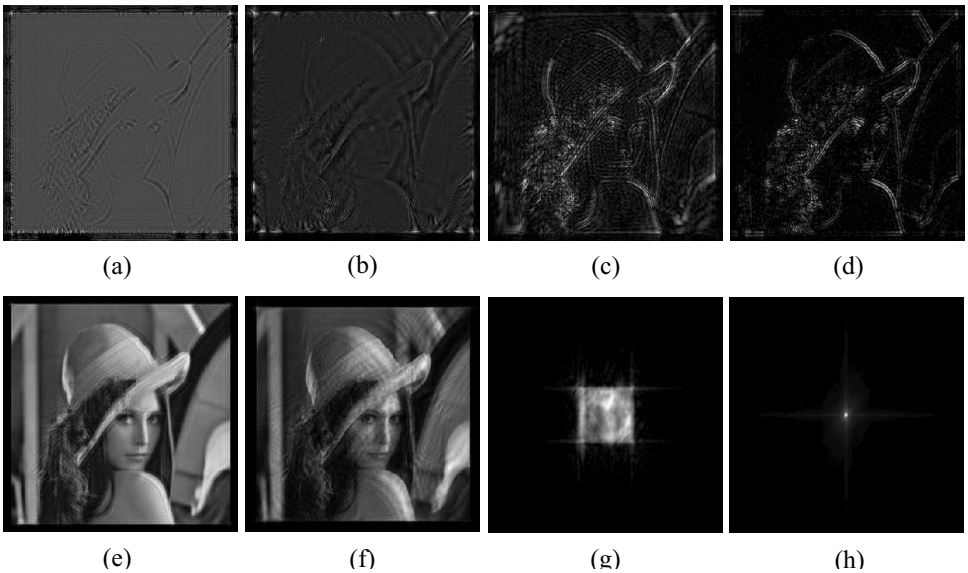

Figure 5.6: Amplitude of the image reconstructed from the phase-only data (a, b, c, d) and the amplitude-only data (e, f, g, h) of the GT of the Lena image for different values of the transformation angle α: (a, e) $\alpha = 2^o$, (b, f) $\alpha = 10^o$, (c, g) $\alpha = 60^o$, (d, h) $\alpha = 90^o$.

Figure 5.6 displays the amplitudes corresponding to the image reconstructed from the phase-only data (a)−(d) and the amplitude-only data (e)−(h) associated to GT of the Lena image. In this example we consider different values for the transformation angle: (a, e) $\alpha = 2^o$, (b, f) $\alpha = 10^o$, (c, g) $\alpha = 60^o$, (d, h) $\alpha = 90^o$. As it is observed, the amplitude of the GT transform contains essential information concerning to the image structure, only for relatively small values of parameter α. Meanwhile, the GT phase preserves the information about the image edges almost for all range of α. To this respect, we can conclude that the gyrator transform is similar to the FRFT [123, 124]. This was expected from Eq. 5.1 and the fact that the GT can be represented as an antisymmetric FRFT embedded between two rotator systems, as we mentioned in chapter 1. These results demonstrate that the phase information of the GT spectrum is more relevant than the amplitude one, excluding rather exotic images whose GT are real for a certain transformation angle ($\varphi_\alpha(\mathbf{r}_o) = 0$). This conclusion underlines that phase-only filters can be applied for pattern detection and recognition in the gyrator domain. It has a particular significance for analogue optical implementation of the filtering in the gyrator domain.

Another example illustrates how the reconstructed image changes if we apply the same filter but in the different GT domains. For this analysis we have considered two binary amplitude filters corresponding to a circular aperture operating as a high-pass (H) and low-pass (L) filters, if they are located in the Fourier domain ($\alpha = \pi/2$). These filters, H and L, are observed in Fig. 5.7(a) and Fig. 5.8(a) respectively, where results of filtering in the image domain ($\alpha = 0$) are displayed. Both figures represent the amplitude of the image filtered in the α−GT domain:

$$A(\mathbf{r}_o) = \left| R^{-\alpha} \left[G(\mathbf{r}) R^{\alpha} \left[f_i(\mathbf{r}_i)(\mathbf{r}) \right] \right] (\mathbf{r}_o) \right|, \tag{5.4}$$

where $G(\mathbf{r})$ is a filter function corresponding to the filters H (Fig. 5.7) or L (Fig. 5.8), respectively.

It is remarkable that filtering is not shift invariant if angle α differs from $\pi/2$. The application of the H-filter in the GT domain leads to the local high frequency pass filtering. The area of its action depends on the filter size and the parameter α. In particular such type of filters can be used for selective edge enhancement. However L-filter (Fig. 5.8) produces image cutting

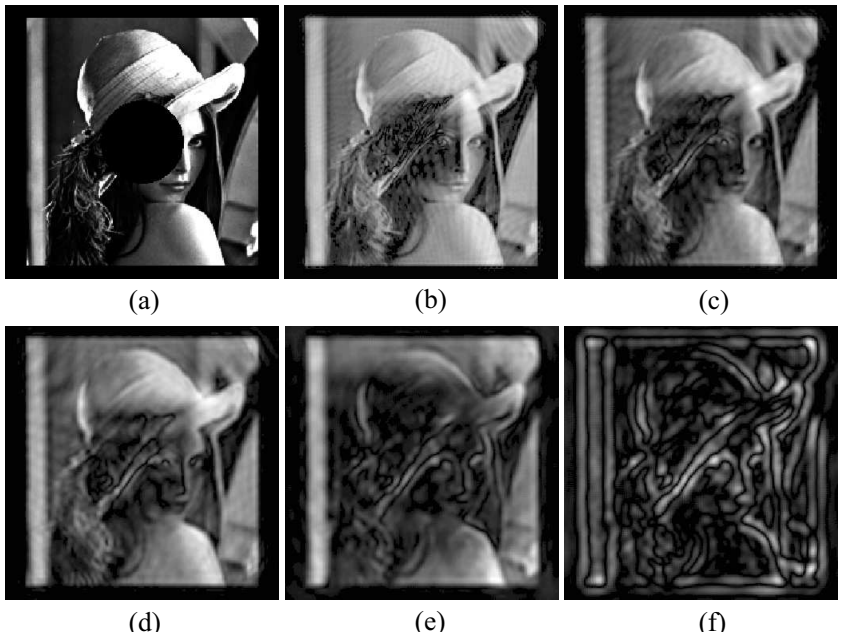

Figure 5.7: Image sequence corresponding to the H-filtering in the gyrator domains for the angles $\alpha = 0^o,\ 20^o,\ 35^o,\ 45^o, 65^o,\ 90^o$, (a-f) respectively.

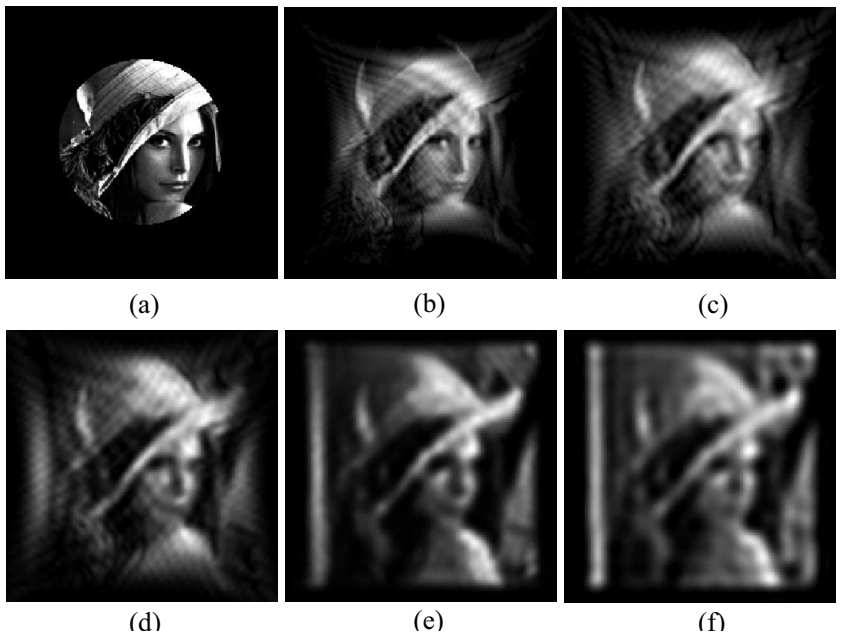

Figure 5.8: Image sequence corresponding to the L-filtering in the gyrator domains for the angles $\alpha = 0^o,\ 20^o,\ 35^o,\ 45^o, 65^o,\ 90^o$, (a-f) respectively.

together with smoothing as expected. The area in which the image is observed as well as the degree of smoothing are enlarged with increasing of angle α.

These results demonstrate the tendency of the filtering procedure in the GT domain as a function of the parameter α. More sophisticated filters have to be design for a concrete image processing task.

5.3 Hyperbolic noise reduction

Noise reduction procedures generally require noise spatial localization by the application of appropriate signal transformations with its further elimination or at least reduction, and the performance of the inverse transformation. For optimized cases the noise localization does not overlap with the signal. Thus for example the plane waves (or more general periodic noise) are localized in the Fourier domain. While the spherical waves (also known as chirp functions) can be localized in the appropriated fractional Fourier domains [12].

Here we demonstrate that the additive hyperbolic type noise, expressed by $A\cos(2\pi cxy) = A\left(\exp\left(-i2\pi cxy\right) + \exp\left(i2\pi cxy\right)\right)/2$ can be removed by filtering in the corresponding gyrator domains. The test image $s(x, y)$ corrupted by the additive hyperbolic noise:

$$f(x, y) = s(x, y) + A\cos(2\pi c(x - v_x)(y - v_y)), \tag{5.5}$$

is displayed in Fig. 5.9(a) for the case $c = 1/\tan(10\pi/9)$.

It is easy to derive from the shift theorem (see Table 4.3, page 31) that the GT of a hyperbolic wave $\exp\left(i2\pi c(x - v_x)(y - v_y)\right)$ becomes the Dirac delta function for $c = \cot\alpha$:

$$\begin{aligned} &R^{\mp\alpha}[\exp\left(\pm i2\pi\cot\alpha(x - v_x)(y - v_y)\right)](\mathbf{r}_o) \\ &= \delta(\mathbf{r}_o \pm \mathbf{v}\cos\alpha)\exp\left(\pm i\pi v_x v_y \sin 2\alpha\right), \end{aligned} \tag{5.6}$$

where $\mathbf{v}^t = (v_x, v_y)$ is a spatial shift. Therefore analyzing the gyrator spectra (squared moduli of the GT) of $f(x, y)$ at angles $\pm\alpha$ we observe the peaks (δ functions) corresponding to the hyperbolic noise localization. These terms can be eliminated by a simple blocking mask. After that the signal is recovered by applying the inverse gyrator transform.

In Fig. 5.9(b) the GT spectrum of the test image is displayed for the angle $\alpha = \arctan(1/c)$. Notice that the noise is localized in the white spot area associated to the function $\delta(\mathbf{r}_o + \mathbf{v}\cos\alpha)$, Eq. (5.6). After application of blocking mask filter in this region, the GT at angle -2α is performed and we again observe the noise localization associated to the function $\delta(\mathbf{r}_o - \mathbf{v}\cos\alpha)$. Repeating the filtering procedure and applying the GT at α, the input signal without noise is finally recovered as it is shown in Fig. 5.9(c). Therefore the filtering procedure requires performing three gyrator transforms (at angles α, -2α and α) and two blocking mask applications in order to eliminate the hyperbolic noise components $\exp\left(\pm i2\pi c(x - v_x)(y - v_y)\right)$. One can appreciate the significant improvement of the denoised image with respect to the one corrupted by the hyperbolic noise.

5.4 Image encryption in gyrator domains

Recently many algorithms for optical image encryption based on random phase masks filtering and fractional Fourier transforms have been proposed [125, 126]. In general the main advantage of these algorithms is that for the correct image decryption we have to know the random phase masks together with the corresponding FRFT domains where they have been located along the encryption procedure. In the other words, the fractional domains also play the role of

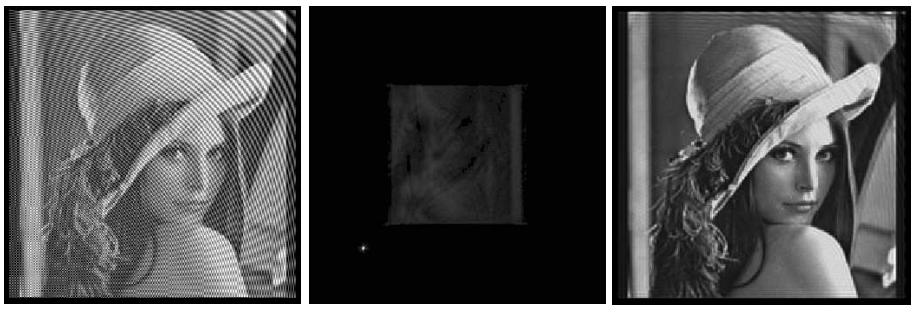

(a) (b) (c)

Figure 5.9: (a) Test image corrupted by an additive hyperbolic noise, (b) the associated spectrum obtained applying the first GT for the angle α and (c) the denoised image.

encoding parameters or keys. Based on a certain similarity between the FRFT and the GT, these techniques can be generalized on the gyrator domains.

The proposed encryption/deccryption procedure consists in a cascade of N operations: gyrator transform at angle α_n with further result multiplication at random phase mask $\exp(i\phi_n)$ for $n = 1, 2...N$. This procedure can be summarized as

$$F(\mathbf{r}) = \exp(i\phi_N)R^{\alpha_N}\left[...\left[\exp(i\phi_2)R^{\alpha_2}\left[\exp(i\phi_1)R^{\alpha_1}\left[f(\mathbf{r})\right]\right]\right]\right]. \tag{5.7}$$

The decryption procedure is written correspondingly as

$$f(\mathbf{r}) = \exp(-i\phi_1)R^{-\alpha_1}\left[...\left[\exp(-i\phi_{N-1})R^{-\alpha_{N-1}}\left[R^{-\alpha_N}\left[\exp(-i\phi_N)F(\mathbf{r})\right]\right]\right]\right]. \tag{5.8}$$

For the latter equations we are using a simplified notation: $R^{\alpha}\left[f(\mathbf{r})\right] = R^{\alpha}\left[f(\mathbf{r}_i)\right](\mathbf{r})$ and $\phi_n = \phi_n(\mathbf{r})$. This encryption/decryption approach for the cascade of two steps ($N = 2$) has been applied to the Lena image. One of the corresponding random phase mask $\phi_n(\mathbf{r})$ (key) is shown in Fig. 5.10(a). The encrypted image in two gyrator domains for $\alpha_1 = 100^o$, $\alpha_2 = 10^o$ is displayed in Fig. 5.10(b). The decryption using the correct random phase masks and the inverse transforms for right keys (α_1, and α_2) leads to the reconstruction of the test image Fig. 5.10(c). Meanwhile the reconstruction with the correct random phase masks but wrong transformation angles (wrong keys) produces unrecognizable image, Fig. 5.10(d).

(a) (b) (c) (d)

Figure 5.10: A random phase mask (key), encrypted image for $\alpha_1 = 100^o$, $\alpha_2 = 10^o$, and the image reconstruction applying the correct and wrong key (transformation angles) are displayed in (a-d), respectively.

Similar results not displayed here are obtained for other transformation angles (α_1, α_2) demonstrating the GT feasibility for encryption techniques.

5.5 Conclusions

In this chapter we have demonstrated some applications of the GT related to mode conversion and image processing. The GT operation can be considered as a tunable mode converter, since it allows the generation of all essentially different structurally stable Gaussian modes, which can be obtained from the HG modes by the integral canonical transforms [112].

The applications of the GT for hyperbolic noise reduction, image filtering and encryption have been shown, which deal with the theoretical predictions. More sophisticated filters have to be developed for every particular case as well as a further research has to be done in order to make a wide comparison with other available image processing tools. However it is demonstrated that the GT operation opens new perspectives in optical and digital information processing. These results were reported in [122] and [127].

Chapter 6

Gyrator transform: experimental implementation

Here we introduce the first flexible optical experimental setup that performs the GT for a wide range of transformation parameters. The action of this experimental setup is demonstrated by choosing the example of the transformation of the Hermite-Gaussian (HG) modes into the helicoidal Laguerre-Gaussian (LG) ones passing through intermediates modes [99, 112] for other values α. The evolution of the complex field amplitude during the propagation through this system is derived analytically. It permits to obtain the operation curves associated to the generalized lenses. Besides an optical system based on two assembled spatial light modulators (SLMs) used for the optical implementation of the input signal (HG modes) is introduced. The experimental results are in excellent agreement with the theoretical predictions that proves the feasibility of the proposed setup.

6.1 Optical implementation

Let us first remind that the GT at parameter α of a function $f_i(\mathbf{r}_i)$, is defined as

$$\begin{aligned} f_o(\mathbf{r}_o) &= R^{\alpha}[f_i(\mathbf{r}_i)](\mathbf{r}_o) \\ &= \frac{1}{|\sin\alpha|}\iint f_i(x_i, y_i)\, \exp\left(i2\pi \frac{(x_o y_o + x_i y_i)\cos\alpha - (x_i y_o + x_o y_i)}{\sin\alpha}\right) \mathrm{d}x_i \mathrm{d}y_i, \end{aligned} \tag{6.1}$$

where $\mathbf{r}_{i,o} = (x_{i,o}, y_{i,o})^t$ are the input and output dimensionless coordinates, respectively.

To study the feasibility of the GT for optical information processing we need an optical setup performing this operation for different transformation angles α. Based on the matrix formalism for the first-order lossless optical systems, it has been designed (chapter 2) a symmetric coherent optical system able to perform the GT for a large range of angles α. This setup contains three generalized lenses with fixed equal distances z between them, see Fig. 6.1(a).

Every generalized lens corresponds to the combination of two convergent thin cylindrical lenses of the same power, Fig. 6.1 (b). Note that the GT at angle α is reached by rotation of these lenses. The generalized lens implies the action of a quadratic (chirp) phase modulation, over an input complex field $g_i(\mathbf{r}_i)$, written as

$$g_o(x_o, y_o) = \exp\left(-i\pi \frac{x_o^2 + y_o^2 - 2x_o y_o \sin 2\varphi}{\lambda f}\right) g_i(x_o, y_o), \tag{6.2}$$

where λ is the wavelength, f is the focal distance of a cylindrical lens, and angle φ indicates the position of the corresponding symmetry axis associated to the cylindrical lenses. Thus

the axis of the cylindrical lenses form angle $\phi_1 = -\varphi$ and $\phi_2 = \varphi - \pi/2$ with the vertical axis OY, respectively [87, 92] [see Fig. 6.1(b)]. The first and third generalized lenses are identical and will be further denoted as $\mathbf{L}_1$. Their focal distance f_1 equals the distance z between two consecutive generalized lenses of the setup, Fig. 6.1(a). The second generalized lens $\mathbf{L}_2$ has a focal distance $f_2 = z/2$. As an example, the phase modulation functions associated to each generalized lenses for the GT at angle $\alpha = 3\pi/4$ ($z = 0.5$ m and $\lambda = 532$ nm) are also shown in Fig. 6.1(a).

The evolution of the complex field amplitude $g_i(x_i, y_i)$ during the propagation through this system is derived by means of the Fresnel diffraction integral and the phase modulation functions associated to generalized lens $\mathbf{L}_1$ and $\mathbf{L}_2$. Using Eq. (6.2) for lens $\mathbf{L}_1$ we obtain the expression for the complex field just before the second generalized lens $\mathbf{L}_2$:

$$g_1(x_1, y_1) = \frac{1}{i\lambda z} \exp\left(i\pi \frac{x_1^2 + y_1^2}{\lambda z}\right) \iint g_i(x_i, y_i) \times \exp\left(-i2\pi \frac{x_1 x_i + y_1 y_i - x_i y_i \sin 2\varphi_1}{\lambda z}\right) \mathrm{d}x_i \mathrm{d}y_i. \tag{6.3}$$

After the corresponding modulation by the second lens transfer function and the propagation through a free-space interval z we derive

$$g_2(x_2, y_2) = -\frac{1}{\left|2\lambda z \sin 2\varphi_2\right|} \exp\left(i\pi \frac{x_2^2 + y_2^2}{\lambda z}\right) \iint g_i(x_i, y_i) \times \exp\left(i\pi \frac{2x_i y_i \sin 2\varphi_1 - (x_2 y_i + x_i y_2 + x_i y_i + x_2 y_2)/\sin 2\varphi_2}{\lambda z}\right) \mathrm{d}x_i \mathrm{d}y_i. \tag{6.4}$$

The action of the third lens, $\mathbf{L}_1$, leads to the final expression for the complex field amplitude at the output plane of the GT system:

$$g_o(x_o, y_o) = -\frac{1}{\left|2\lambda z \sin 2\varphi_2\right|} \iint g_i(x_i, y_i) \times \exp\left(i2\pi \frac{(x_o y_o + x_i y_i)(2 \sin 2\varphi_1 \sin 2\varphi_2 - 1) - (x_o y_i + x_i y_o)}{2\lambda z \sin 2\varphi_2}\right) \mathrm{d}x_i \mathrm{d}y_i. \tag{6.5}$$

This equation coincides, except to a constant phase factor, with the definition of the gyrator transform at angle α with normalization $s^2 = \lambda z$, [Eq. (6.1)] if it holds:

$$\begin{aligned} \sin 2\varphi_1 &= \cot(\alpha/2), \\ \sin 2\varphi_2 &= (\sin \alpha)/2. \end{aligned} \tag{6.6}$$

Notice that the rotation angles φ_1 and φ_2 correspond to the generalized lenses $\mathbf{L}_1$ and $\mathbf{L}_2$, respectively. It is easy to see from the later relation that this setup performs the GT only for the angles $\alpha \in [\pi/2,\ 3\pi/2]$. Nevertheless since $R^{\alpha+\pi}[f_i(\mathbf{r}_i)](\mathbf{r}_o) = R^{\alpha}[f_i(\mathbf{r}_i)](-\mathbf{r}_o)$ we can cover all the interval $\alpha \in [0,\ 2\pi]$ if it is necessary.

The variation of the transformation angle α is achieved only by means of the rotation of cylindrical lenses according to the operation curves. The operation curve is a graphical representation of the rotation angle ϕ_1 of one of the cylindrical lenses (which composes a given generalized lens) as a function of the transformation angle α. In Fig. 6.2 the operation curves $\phi_1(\alpha)$ for the generalized lens $\mathbf{L}_1$(a) and $\mathbf{L}_2$ (b) are displayed. Notice that $\phi_2(\alpha)$ is derived from the relation $\phi_2 = \phi_1 - \pi/2$. In addition, when the angle between the cylindrical lenses is $\pi/2$ then a generalized lens reduces to a spherical one.

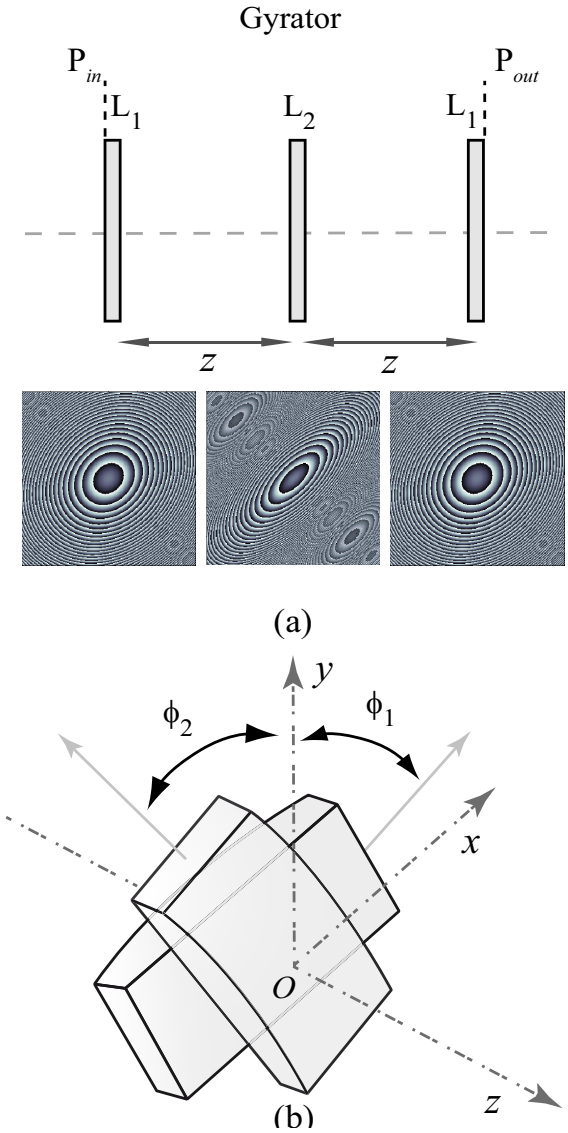

Figure 6.1: Setup scheme associated to the gyrator transform, (a). The phase modulation functions (for the case $z = 0.5m$ and $\lambda = 532nm$) associated to each generalized lenses when the set up performs the GT at angle $\alpha = 3\pi/4$ are shown below, where the grey levels indicate the phase distribution range $[-\pi, \pi]$. An assembled set of two cylindrical lens, which forms the generalized lenses $\mathbf{L}_1$and $\mathbf{L}_2$ is displayed in (b).

It is remarkable that for $\alpha = \pi$, occurring when the generalized lenses $\mathbf{L}_1$ and $\mathbf{L}_2$ are reduced to the spherical lenses, the common 4-f system (a cascade of two Fourier transforming systems) is obtained. Therefore the proposed gyrator system can be considered as a generalization of the well-known optical processing 4-f system to the case of the generalized lenses.

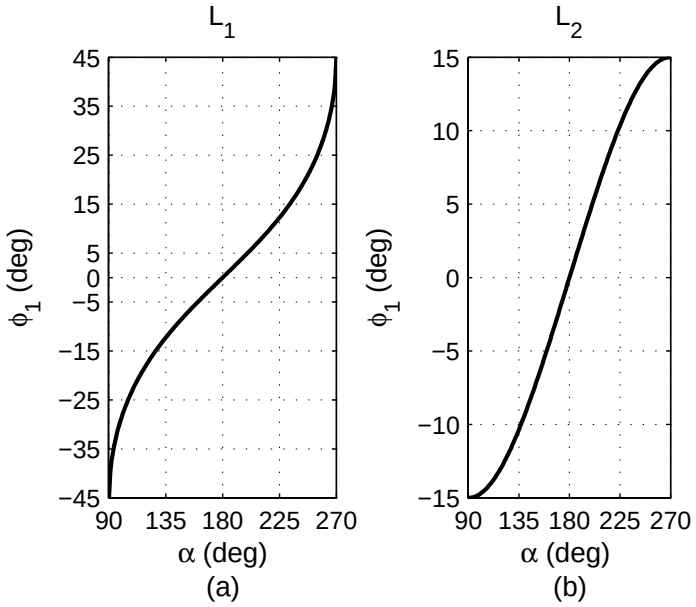

Figure 6.2: Operation curves $\phi_1(\alpha)$ for the generalized lenses $\mathbf{L}_1$(a) and $\mathbf{L}_2$ (b). The operation curve $\phi_2(\alpha)$ is derived from the relation $\phi_2 = \phi_1 - \pi/2$.

In Fig. 6.3 a detailed scheme of the GT optical experimental setup is displayed. The input complex field amplitude is generated by the two coupled spatial light modulators (SLMs). This optical configuration is known as a hybrid hologram [128] because the amplitude and phase components of the input signal are separately implemented on each SLM. The amplitude component is projected by means of a 4-f lens system on the second SLM, which introduces the appropriate phase modulation. The second 4-f lens system is used in order to remove the nonzero diffraction orders in the Fourier plane, arising due to the discrete structure of the SLMs. The further spatial filtering of the nonzero order diffraction components ensures a good agreement with the theoretical results as we will see in the next Section.

The main disadvantage of this hybrid hologram scheme concerns the alignment accuracy between the SLM displays. Nevertheless, position stages for the SLMs are not required because the alignment between amplitude and phase components are digitally achieved by means of a PC. Therefore the alignment accuracy is limited by the pixel size, which is 20 μm in our case (Holoeye LCR-2500 SLM). The signal quality is also limited by the spatial resolution and in addition by the dynamic range of the SLM (8 bits). The application of the SLMs for an input signal generation allows to perform an almost real time information processing. The distance between generalized lenses in our experimental setup is $z = 0.5$ m. An extended discussion about this particular setup for the complex field generation is found in appendix C.

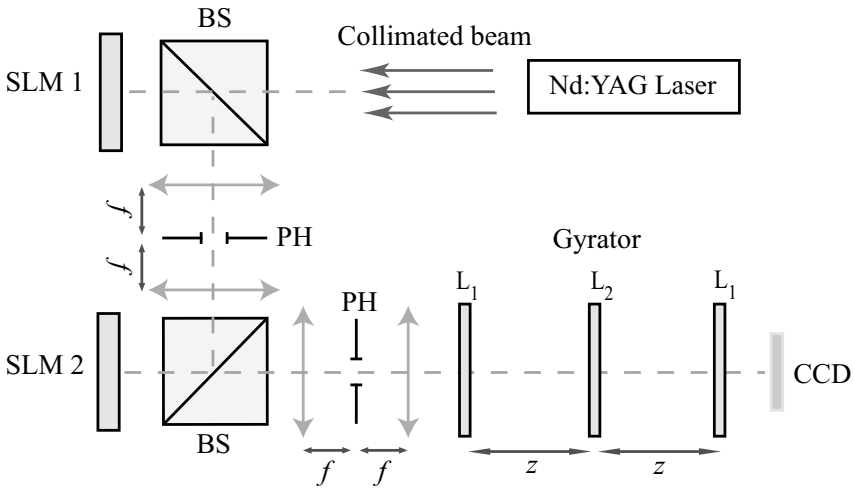

Figure 6.3: Detailed scheme for the experimental optical system configuration. Two SLMs (Holoeye LCR-2500) are used for the input signal (HG mode) generation. BS is a beam splitter. A pin-hole PH is placed at the Fourier plane of the 4-f system. The GT at angle α is performed by three generalized lenses. The parameter α is changed by the proper rotation of the cylindrical lenses which form every generalized lens. The output signal is registered using a CCD camera (Sony XCD-X710).

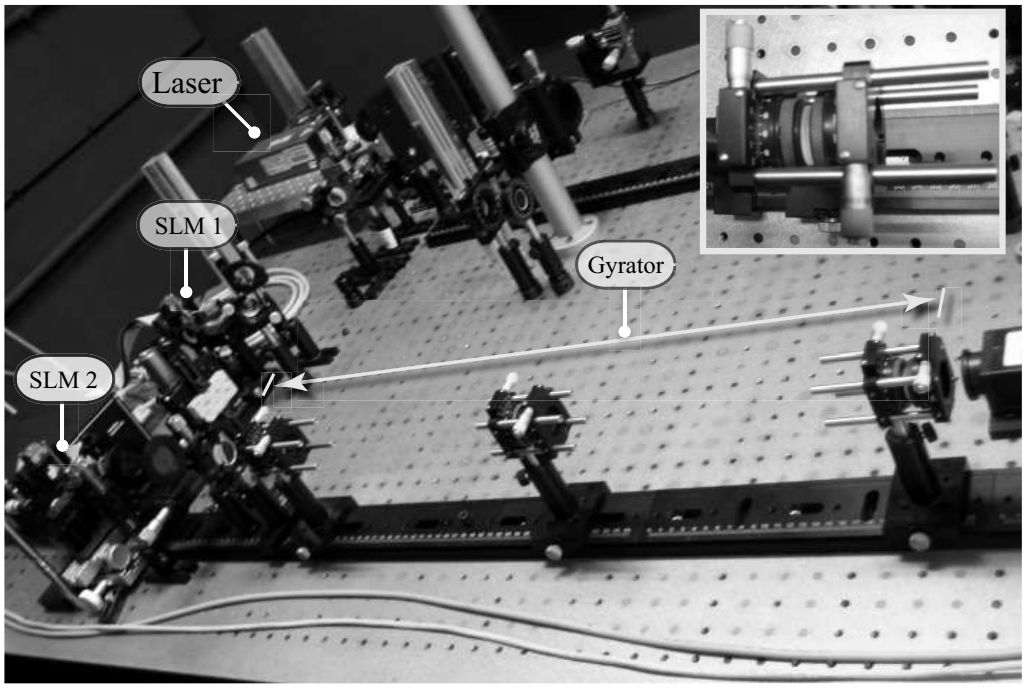

Figure 6.4: Picture corresponding to the experimental optical system configuration. The optical system based on two SLMs for the input field generation as well as the gyrator system, are shown. Inset displays a generalized lens corresponding to an assembled set of two convergent cylindrical lenses. More details in Fig. C.1, appendix C.

6.2 Experimental results

To demonstrate the experimental implementation of the GT we use HG modes of various orders as input signals. As mentioned, a HG mode is given by the following expression:

$$\mathrm{HG}_{m,n}(\mathbf{r};w) = 2^{1/2}\frac{H_m\left(\sqrt{2\pi}\frac{x}{w}\right)H_n\left(\sqrt{2\pi}\frac{y}{w}\right)}{\sqrt{2^m m!w}\sqrt{2^n n!w}}\exp\left(-\frac{\pi}{w^2}\mathbf{r}^2\right), \tag{6.7}$$

where H_m is the Hermite polynomial and w is the beam waist. The beam waist is set at $w = 0.73$ mm for the HG modes considered in this work. The HG modes $\mathrm{HG}_{m,n}(\mathbf{r};w)$ are generated experimentally by the complex amplitude modulation of a collimated Nd:YAG laser beam ($\lambda = 532$ nm) thanks to the coupled SLMs setup discussed above. As an example, the intensity distribution of the $\mathrm{HG}_{7,4}$ mode and its phase structure in the form of the interferogram with a collimated beam are demonstrated in Fig. 6.5(a) and (b), respectively. Inset in Fig. 6.5(b) shows the dislocation among the interference fringes due to the phase shift π. The images were registered by CCD camera, Sony XCD-X710.

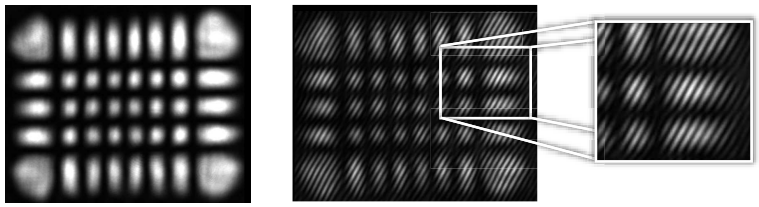

(a) (b)

Figure 6.5: Hermite-Gaussian mode $\mathrm{HG}_{7,4}$ obtained using the hybrid hologram. The image (a) corresponds to $HG_{7,4}$ intensity distribution and (b) is an interference pattern which reveals the $\mathrm{HG}_{7,4}$ phase distribution. Inset in (b) shows the dislocation among the interference fringes due to the phase shift π.

The rest of the results shown in Figs. 6.6–6.8 are related to the functioning of the gyrator transform setup. As previously mentioned the $\mathrm{HG}_{m,n}(\mathbf{r};w)$ modes are transformed under the GT action, at angles $\alpha = (2k+1)\pi/4$ (k is an integer), into the helicoidal LG modes:

$$\mathrm{LG}^{\pm}_{p,l}(\mathbf{r};w) = w^{-1}\sqrt{\frac{\min(m,n)!}{\max(m,n)!}}\left(\sqrt{2\pi}\left(\frac{x}{w}\pm i\frac{y}{w}\right)\right)^l L^l_p\left(\frac{2\pi}{w^2}\mathbf{r}^2\right)\exp\left(-\frac{\pi}{w^2}\mathbf{r}^2\right), \tag{6.8}$$

where L^l_p is the Laguerre polynomial, $p = \min(m,n)$ and $l = |m-n|$. In particular for the angle $\alpha = 3\pi/4$ the $\mathrm{HG}_{8,6}$, $\mathrm{HG}_{3,2}$, and $\mathrm{HG}_{3,3}$ modes are transformed into $\mathrm{LG}^{+}_{6,2}$, $\mathrm{LG}^{+}_{2,1}$, and $\mathrm{LG}_{3,0}$. The experimental results of this transformation are shown in Fig. 6.6. Moreover an interference pattern of the LG mode with a collimated wave that reveals its helicoidal phase distribution, in the from of a fork-like structure, is displayed in Fig. 6.6(a)–(c). We remark that the mode transformation is not affected by additional scaling and phase modulation because the beam waist w as well as the wavelength are such that $w = s = \sqrt{\lambda z}$.

It should be noted that for $\alpha = \pi k/2$ the output mode corresponds to $\mathrm{HG}_{m,n}$ rotated at angle α with an additional phase shift. For the rest of the transformation angles the intermediate modes (or gyrating modes [112]) carry fractional OAM, as we mentioned in the previous chapter. In particular in Fig. 6.7 the modes generated from the input mode $\mathrm{HG}_{5,3}$ [Fig. 6.7(a)] by the GT for the angles $\alpha \in [3\pi/4,\ \pi]$ are displayed. The first and the second rows show the numerical simulation of the intensity and phase distributions of these modes, respectively. The third row

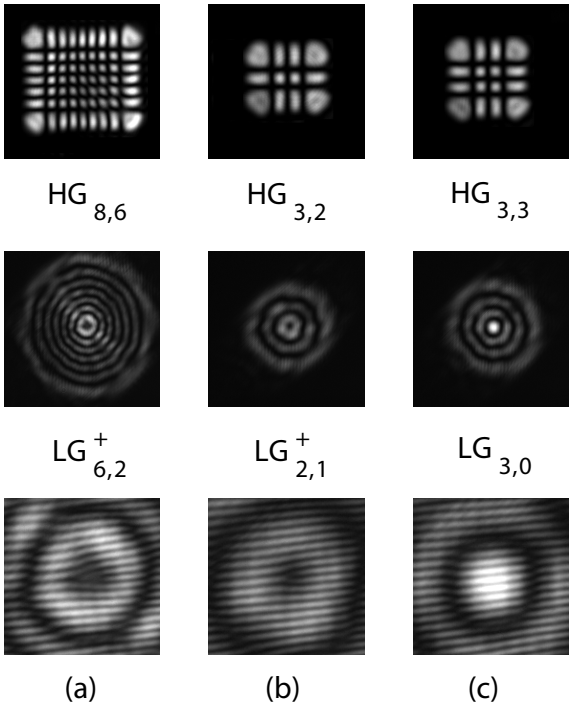

Figure 6.6: Input HG modes $HG_{8,6}$, $HG_{3,2}$ and $HG_{3,3}$ are transformed by the GT at $\alpha = 3\pi/4$ into LG modes $LG^{+}_{6,2}$, $LG^{+}_{2,1}$ and $LG_{3,0}$, respectively. The interferograms for these LG modes with a plane wave are displayed in (a-c), correspondingly. Images (a) and (b) reveal a fork-like structure, typical for the associated helicoidal phase distribution, which is not present for the case of $LG_{3,0}$ (c).

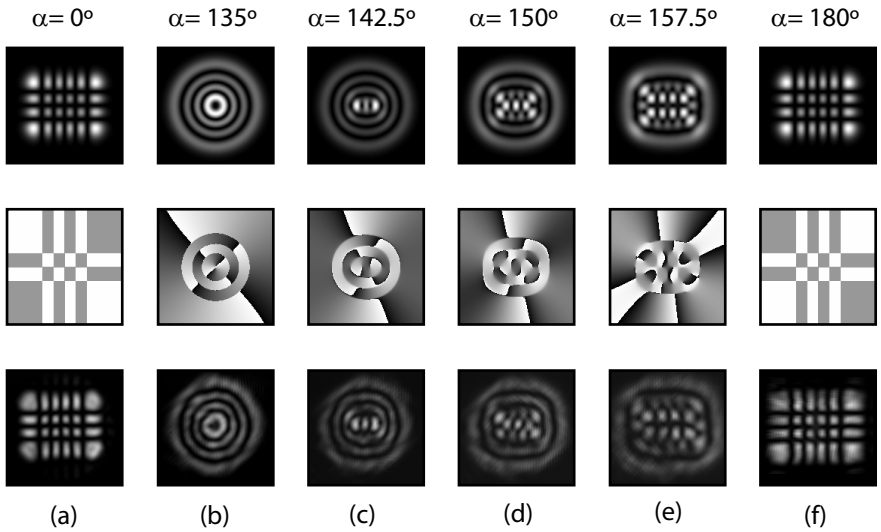

Figure 6.7: Intermediate modes obtained by the GT of the input mode $HG_{5,3}$ (a) for the angles $\alpha = [3\pi/4, \pi]$, (b-f). The first and second rows correspond to the intensity and phase distributions (grey levels indicate the phase range $[-\pi, \pi]$), respectively, obtained by numerical simulations of the GT. The experimental intensity distributions are shown in the third row. The input mode ($\alpha = 0$) generated by the SLMs is also displayed at the third row, (a).

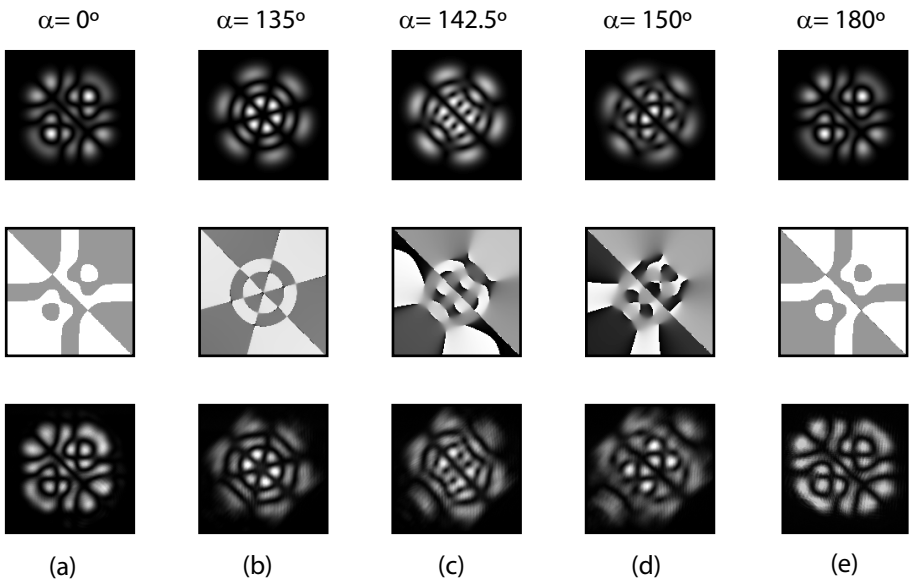

Figure 6.8: Intermediate modes obtained by the GT of the HG modes composition $HG_{5,2} + HG_{2,5}$ (a) for the angles $\alpha = [3\pi/4, \pi]$, (b-e). The first and second rows correspond to the intensity and phase distributions (grey levels indicate the phase range $[-\pi, \pi]$), respectively, obtained by numerical simulations of the GT. The experimental intensity distributions are shown in the third row. The input mode ($\alpha = 0$) generated by the SLMs is also displayed at the third row, (a).

in Fig. 6.7(a)−(f) corresponds to the experimental intensity distribution registered by means of the CCD camera.

Furthermore, a composition of the HG modes of the same order ($n + m$ =const) also produces a structurally stable mode under the GT action. For instance, the mode composition $HG_{5,2} + HG_{2,5}$ [Fig. 6.8(a)] leads for $\alpha = 3\pi/4$ to the odd LG mode corresponding to the sum of two helicoidal LG modes with opposite OAM values: $LG^{+}_{2,3} + LG^{-}_{2,3}$ [Fig. 6.8(b)]. The intermediate modes are displayed in Fig. 6.8(c) and (e). We remark that due to the input mode symmetry it is an eigenfunction for GT at the angle $\alpha = \pi$, which is a simple π−angle rotation [see Fig. 6.8(e)]. The first and second rows again show the numerical simulation of the intensity and phase distributions of these modes. While the third row Fig. 6.8(a)−(e) corresponds to the experimental intensity distribution.

6.3 Conclusions

The experimental results obtained by the proposed GT setup are in excellent agreement with the theoretical predictions demonstrating its feasibility. We remark the image fidelity and lack of noise. Indeed, the flexible structure of this scheme, which means fixed distances between the generalized lenses and the manipulation of the transformation angle by means of lens rotation, makes the setup useful for numerous applications. In particular the proposed experimental setup is able to generate, almost in real time, a wide spectrum of modes applicable for beam design purposes, optical trapping, quantum information, etc. In addition, is also demonstrated the feasibility of the proposed setup based on two coupled SLMs for the input (HG modes) complex field generation. These results were reported in [129].

Moreover, regarding the promising results related to the application of the GT for filtering, noise reduction, and encryption, this setup can be used for optical image processing.

Chapter 7

Fresnel diffraction effects in Fourier-transform AWG spectrometer

In this chapter we present an optimized design for a Fourier-transform (FT) microspectrometer based on two interleaved arrayed waveguide gratings (AWG), referred to as FT-AWG. This optical design is derived from the analysis of the near-field diffraction effects arising in a FT-AWG microspectrometer operating in transmission geometry. The retrieval of spectral information is reached by Fourier analysis of the interference pattern, which is generated by the light emerging from AWG arrays. In contrast to conventional AWG devices where an image of the input waveguide is formed dispersively in the focal region, thus operating in Frauhoffer (far-field) diffraction regime, our device does not involve focusing and operates in Fresnel diffraction regime. In this work we solve the near-field diffraction problem for this AWG device. It allows us to find a compact and flexible microspectrometer design that permits the retrieval of spectral information with a high crosstalk suppression. The proposed scheme is flexible since it does not requiere a measurement of the interference pattern in a fixed plane.

7.1 Fundamentals

The retrieval of the spectral information can be reached by using spectrometers based on first-order optical systems. High resolution spectroscopies (e.g., Raman or Fourier transform infrared) are needed for the development of new detection devices in genomics and health-related applications. Nowadays, the optoelectronic technology offers miniature spectrometers devices which are being considered as a promising candidates for such applications.

In order to reach high spectral resolution demanded by some applications, several miniature microspectrometers based on AWGs have been recently developed, [130, 131]. Such devices comprises many channels (wavelengths) with a high spectral resolution by using high index contrast (HIC) silicon-on-insulator (SOI) waveguides. This spectrometer concept operates in interferometric configuration, which can be further generalized to include various waveguide configurations in transmissive and reflective geometries [132]. For instance, by simultaneously using multiple input apertures the optical throughput of the microspectrometer is largely increased [133]. As an example, a scanning electron microscope (SEM) image corresponding to a deep etched HIC-AWG is displayed in Fig. 7.1; refractive index $n_{cladding}(SiO_2) \sim 1.5$ and $n_{core}(Si) \sim 3.5$.

In this work we propose a microspectrometer design based on this concept. In particular, our device is constructed by using two interleaved AWGs. As in the previous devices, the interferometric configuration results in interference fringes with a wavelength-dependent period. Therefore, the spectral retrieval can be reached by Fourier analysis of the interference pattern. Compared to a conventional AWG which is a generalized multi-path Mach-Zehnder interferometer, our FT-AWG, as a Michelson type device [132], allows for a markedly larger input aperture with a correspondingly increased optical throughput. Furthermore, unlike a conventional FT-Michelson spectrometer which requires moving parts (a scanning mirror), the FT-AWG is a static device obviating the need for scanning elements.

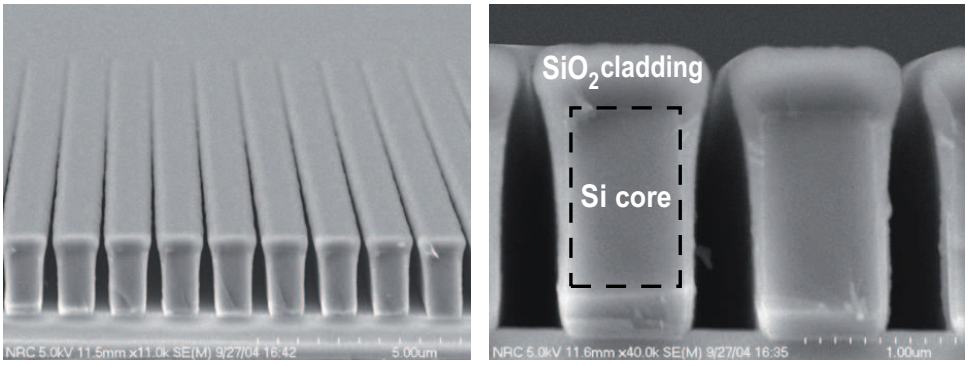

(a) (b)

Figure 7.1: SEM image of deep etched waveguides. An AWG device is displayed in (a). Detail cross-section view of a waveguide (b). Images courtesy of Optoelectronic Devices Group, Institute for Microstructural Sciences, National Research Council of Canada.

FT-AWG device operates in transmission geometry splitting an input wavefront (collimated beam) in two colineal wavefronts tilted in opposite directions. Each output wavefront corresponds to a superposition of gaussian-like modes because each waveguide only guides its fundamental mode. This can be understood as sampling of the input wavefront by means of the discrete device structure. On the other hand, the periodic structure associated to each AWG introduces diffraction effects which have to be studied in order to characterize the device performance. In the near-field diffraction regime these effects correspond to well-known Talbot effect as it will be demonstrated.

The superposition of Talbot patterns associated to each AWG yields a distinct spatial modulation of the interference pattern referred to as the Moiré-Talbot effect. We explain the effect analytically and also study it numerically, including its influence in the performance of the FT-AWG spectrometer device. Besides we study the retrieval of spectral information in a FT-AWG spectrometer in the presence of the Moiré-Talbot effect. We propose a FT-AWG device that comprises two interleaved waveguide arrays each with 180 waveguides and the interference order of 40. It is designed with a Rayleigh spectral resolution of $R = 0.1$ nm and 8 nm bandwidth at wavelength $\lambda = 1.5$ μm. We also demonstrate, by numerical simulations of this FT-AWG microspectrometer, a crosstalk reduction from -20 dB to -40 dB by Gaussian apodization.

7.2 FT-AWG device design and performance in presence of Talbot effect

The scheme of an FT-AWG device is shown in Fig. 7.2(a). The input field is sampled by a multiple waveguide aperture followed by an array of splitters which couple light into two interleaved waveguide arrays AWG_p ($p = 1, 2$) with respective interference orders m_p [132]. The required linear optical path increment between the adjacent waveguides of each AWG are obtained with bend waveguide sections acting as phase shifters, as indicated in Fig. 7.2 (a) and (b). The bend waveguide sections are commonly used in planar waveguide devices. All parts of the device, including bend waveguide sections, are contained within the waveguide plane (Fig. 7.2, plane xz). The waveguide pairs of the two AWGs can be recombined by an array of 3 dB couplers, forming a multiple waveguide output aperture terminated in the slab waveguide combiner region followed by the free-space propagation region (air). As it is shown in Fig. 7.2(a), the interference fringes are intercepted directly by a photodetector array located at the chip edge. The sampling effects arising from the discrete photodetector array are discussed at the end of this chapter.

The FT-AWG device can be implemented on different planar waveguide platforms, including low and high index contrast waveguides platforms. In this work we show a design example for a SOI waveguide platform which was previously used for fabricating compact AWG devices [132, 134].

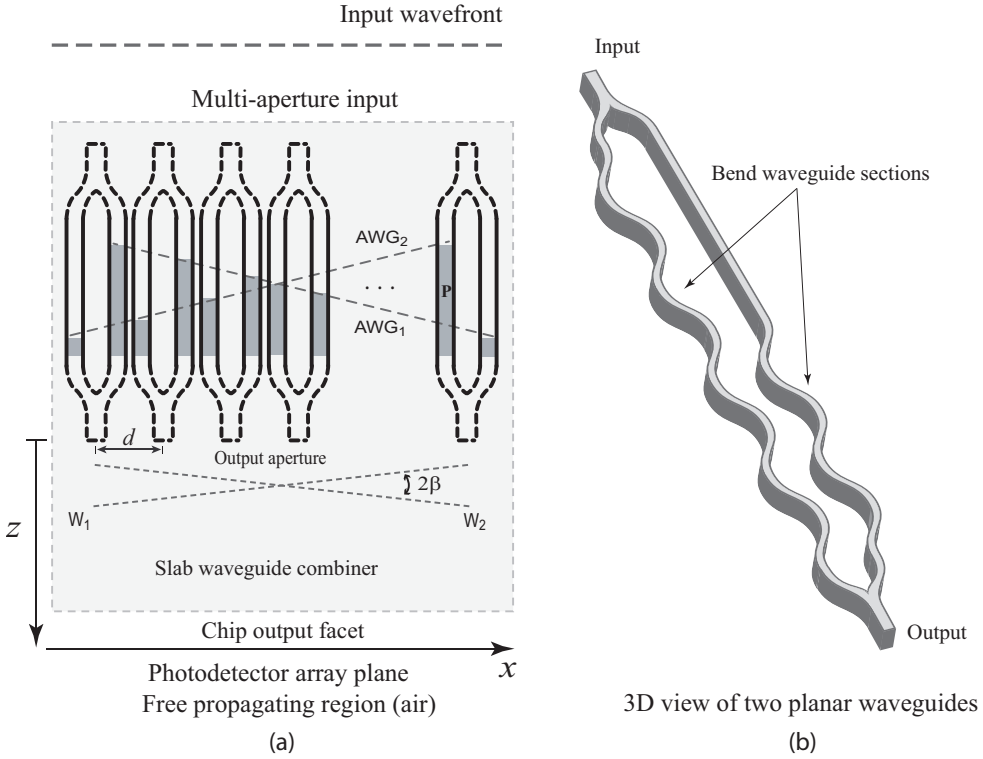

Figure 7.2: (a) General schematics of a FT-AWG microspectrometer with two interleaved AWGs. Wavefronts W_1 and W_2 originating from AWG_1 and AWG_2 propagate with a wavelength dependent tilt angle $\beta(\lambda)$ and $-\beta(\lambda)$, respectively. The phase shifters are indicated by the grey region P, which can be constructed by using bend waveguide sections. An example of bend waveguide sections corresponding to this device schematic is displayed in (b).

For interleaved AWGs with inverted interference orders ($m_1 = -m_2 = m$), as the wavelength changes, the two wavefronts emerging at the output aperture of the respective waveguide arrays tilt in the opposite direction according to the AWG dispersion relation, see Fig. 7.2(a): W_1 and W_2. This superposition results in interference fringes with a wavelength-dependent period in the combiner free-space propagation region where the two wavefronts overlap. In the combiner region, wavefront W_p originating from AWG$_{p=1,2}$ propagates with a wavelength dependent tilt angle $\beta(\lambda)$. The latter is a function of the phase shift $\Delta\phi_p(\lambda)$ between the waves originating in the two adjacent waveguides of an AWG that can be written as [135, 136]:

$$\Delta\phi_p = \frac{2\pi m_p n_g (\lambda - \lambda_L)}{n_0 \lambda_L} \tag{7.1}$$

From this expression it is easy to derive that the wavefront tilt angle β is given by:

$$\sin\beta = (\lambda - \lambda_L)\frac{n_g m_p}{d\, n_0 n_{eff}}, \tag{7.2}$$

where λ_L is the Littrow wavelength [$\beta(\lambda_L) = 0$], n_g is the group index of the arrayed waveguides, n_0 is the fundamental waveguide mode effective index, n_{eff} is the effective index in the combiner region, and d is the AWG pitch [131].

The scalar field distribution in proximity of the waveguide array can be obtained by solving the diffraction problem in the Fresnel regime for the periodic waveguide grating structure. The field at the interface between the waveguide array and the combiner region can be represented by the periodic signal $t(x)$ with a tilted phase front:

$$T_p(x) = t(x)\exp(-i2\pi\alpha_p x), \tag{7.3}$$

where

$$t(x) = \sum_{q=-\infty}^{+\infty} a_q \exp\left(i2\pi\frac{qx}{d}\right) \tag{7.4}$$

is one dimensional Fourier expansion and $\alpha_p = \sin(\beta)/\lambda$. For a device with interleaved AWGs, $\alpha_1 = -\alpha_2 = \alpha$ and $T_1(x) = T_2^*(x) = T(x)$. The field distribution at a distance z from the waveguide array aperture is given by the Fresnel integral Eq. (1.10):

$$\begin{aligned} W_p(x,\ z) &= \frac{\exp(ikn_{eff}z)}{\sqrt{i\lambda z}}\int_{-\infty}^{\infty} T_p(x_i)\exp\left(i\frac{\pi n_{eff}}{\lambda z}(x-x_i)^2\right)dx_i \\ &= \Phi(z)\exp(-i2\pi\alpha_p x)t(x,z,\alpha_p), \end{aligned} \tag{7.5}$$

where

$$\Phi(z) = \exp(ikn_{eff}z)\exp\left(-i\pi\lambda z\alpha_p^2/n_{eff}\right), \tag{7.6}$$

and

$$t(x,z,\alpha_p) = \sum_{q=-\infty}^{+\infty} a_q \exp\left(i2\pi\frac{qx}{d}\right)\exp\left(-i\pi\lambda z\frac{q^2}{d^2 n_{eff}}\right)\exp\left(i2\pi\lambda z\alpha_p\frac{q}{dn_{eff}}\right). \tag{7.7}$$

Therefore the interference pattern at the propagation distance z is given by:

$$\begin{aligned} I(x,z) &= |W_1(x,z) + W_2(x,z)|^2 = \left|t\,(x,z,\alpha) + t\,(x,z,-\alpha)\exp(i2\pi 2\alpha x)\right|^2 \\ &= |t\,(x,z,\alpha)|^2 + |t\,(x,z,-\alpha)|^2 + 2t\,(x,z,\alpha)\,t\,(x,z,-\alpha)\cos(2\pi 2\alpha x). \end{aligned} \tag{7.8}$$

At the propagation distance $z_l = z_T l$ ($l = 1, 2\ldots$), Eq. (7.5) is reduced to:

$$\begin{aligned} W_p(x,z_l) &= \Phi(z_l)t\left(x + 2d^2 l\alpha_p\right)\exp(-i2\pi\alpha_p x) \\ &= \Phi(z_l)T_p\left(x + 2d^2 l\alpha_p\right)\exp\left(i2\pi 2\left(d\alpha_p\right)^2 l\right), \end{aligned} \tag{7.9}$$

which is associated to the well-known Talbot effect, also known as self-imaging phenomenon, where $z_T = 2n_{eff}d^2/\lambda$ is the Talbot distance [102]. For the case corresponding to fractional Talbot distances $z_T\eta/\zeta$, where η and ζ are integers and $\eta < \zeta$, the field distribution is given by (ζ even):

$$W_p(x, z_T\eta/\zeta) = \Phi(z_T\eta/\zeta) \sum_{a=0}^{\zeta/2-1} B(a, \eta, \zeta) T_p\left(x - \frac{d}{2} + \frac{2\eta a}{\zeta}d + \frac{2\eta}{\zeta}d^2\alpha_p\right), \tag{7.10}$$

where

$$B(a, \eta, \zeta) = \frac{2}{\zeta} \sum_{b=0}^{\zeta/2-1} \exp\left(i2\pi\frac{2ba}{\zeta}\right) \exp\left(-i\pi\left(2\frac{b^2\eta}{\zeta} + b\right)\right) \tag{7.11}$$

are the Talbot coefficients. Equation Eq. (7.10) is a generalization of the expression obtained in [137] for small oblique angle of illumination (β). Analogously a relation for odd fractional orders ζ can be also found, [138].

7.2.1 Retrieval of spectral information

In this section the retrieval of the spectral information in presence of the Talbot effect is analyzed. Let us start considering the case corresponding to $z = z_T$, in which the expression Eq. (7.8) is reduced to

$$\begin{aligned} I(x, z_T l) &= |W_1(x, z_T l) + W_2(x, z_T l)|^2 = \left|t\left(x + 2d^2 l\alpha\right) + t\left(x - 2d^2 l\alpha\right)\exp(i2\pi 2\alpha x)\right|^2 \\ &= \left|t\left(x + 2d^2 l\alpha\right)\right|^2 + \left|t\left(x - 2d^2 l\alpha\right)\right|^2 + 2t\left(x + 2d^2 l\alpha\right)t\left(x - 2d^2 l\alpha\right)\cos(2\pi 2\alpha x). \end{aligned} \tag{7.12}$$

The expression Eq. (7.12) contains various terms with wavelength dependent spatial frequencies of 2α, $f_d \pm 2\alpha j$ and $2f_d \pm 2\alpha j$, where $j = 0$ or 1, and $f_d = 1/d$ is the spatial frequency of the single waveguide array. Indeed, analyzing Eq. (7.12) one conclude that spatial frequencies f_d and $2f_d$ are associated to the first and second terms of this expression, meanwhile the rest of frequencies correspond to the third term.

The nature of the terms with different spatial frequencies in Eq. (7.12) is illustrated in the following example. Let us consider an interleaved FT-AWG device, with 180 waveguides in each of the array, hence total $N = 360$ waveguides, and interference order $m_1 = -m_2 = 40$. The pitch at the arrayed waveguide aperture is $d = 4$ μm, and the effective width of the waveguide fundamental mode is $w = 4.8$ μm. In this case z_T (1500 nm) = 73 μm, for a silicon ($n_{eff} = 3.44$) slab waveguide combiner region. The total number of waveguides (N) and the interference order (m) were chosen to provide the specified spectral resolution ($\Delta\lambda = 0.1$ nm at Rayleigh limit). As it is demonstrated in [131], for a Fourier transform arrayed waveguide spectrometer the wavelength resolution is $\Delta\lambda = \lambda/(mN)$, which is equivalent to a diffraction grating based device with N grating facets and the interference order m. The waveguide pitch d and the effective width of the waveguide mode was chosen based on previous experimental work on AWGs fabricated in SOI waveguide platform with a 2.2 μm-thick Si waveguide core layer [132, 134], see Fig. 7.1(b). However, the pitch can be modified to provide a specific value of the FT-AWG dispersion, according to Eq. (7.12). Its influence on the interference pattern is analytically included in Eq. (7.12) through the terms d and α, which also is a function of d.

Since $\alpha(\lambda_L) = 0$, there is obviously no spatial interference effect at the Littrow wavelength, which has been set here to $\lambda_L = 1500$ nm. Fig. 7.3 shows the interference pattern represented by Eq. (7.12) and its Fourier spectrum calculated by means of the FFT algorithm (Fast Fourier Transform) for the wavelength of 1502 nm. The spatial spectrum reveals seven peaks which correspond to the spatial frequencies of 2α (a), $f_d \pm 2\alpha j$ (b, c, d), and $2f_d \pm 2\alpha j$ (e, f, g), as they are identified in the bottom panel of Fig. 7.3. The terms corresponding to the peaks (a), (b),

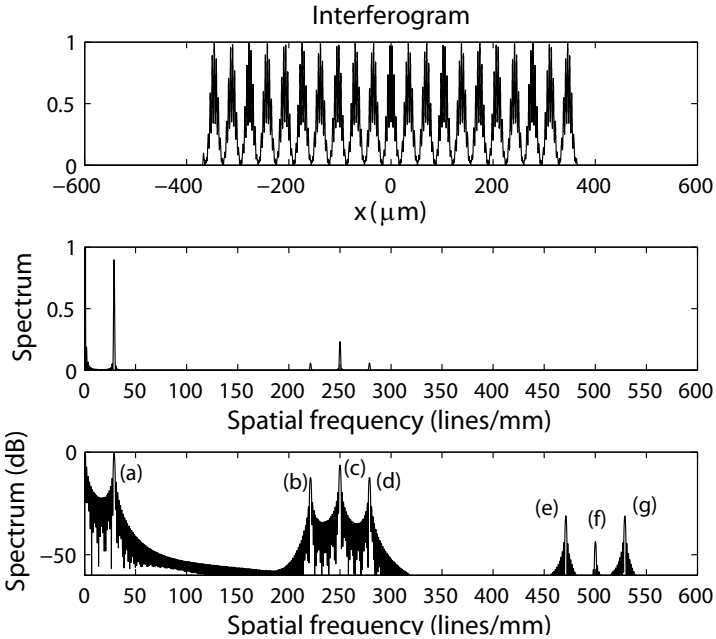

Figure 7.3: Interferogram (top) at a Talbot plane and its Fourier spectrum (center and bottom, in linear and logarithmic scales, respectively). Wavelength $\lambda = 1502$ nm. The peaks (a-g) correspond to the spatial frequencies of 2α (a), $f_d \pm 2\alpha j$ (b-d) and $2f_d \pm 2\alpha j$ (e-g).

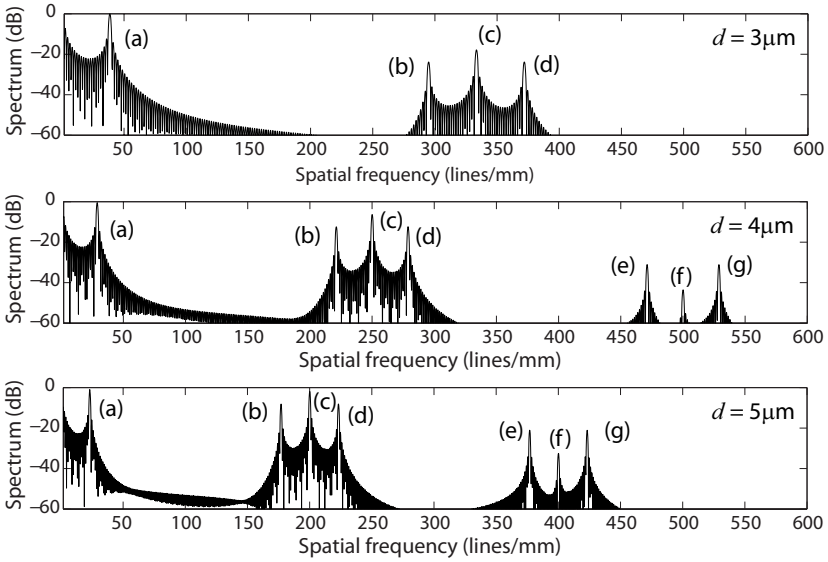

Figure 7.4: The waveguide pitch influence on spectral retrieval. The waveguide pitch 3 μm (top), 4 μm (center), and 5 μm (bottom). The terms (a)-(g) of Eq. (7.12) are identified to help visualize the effect of varying pitch on different spatial frequencies.

(d), (e), and (g) carry the spectral information, whereas the terms (c) and (f) represents the Talbot effect. It is important to clearly distinguish between these different terms since, if not correctly understood, they can be misinterpreted as spurious spectral lines. In this particular example the higher order terms (b)−(g) appear at rather high spatial frequencies thus would be automatically filtered when reading out the fringe pattern by a conventional photodetector array. However, in designs with the higher order terms (b)−(g) at lower spatial frequencies, these would need to be carefully considered to avoid a false spectral interpretation.

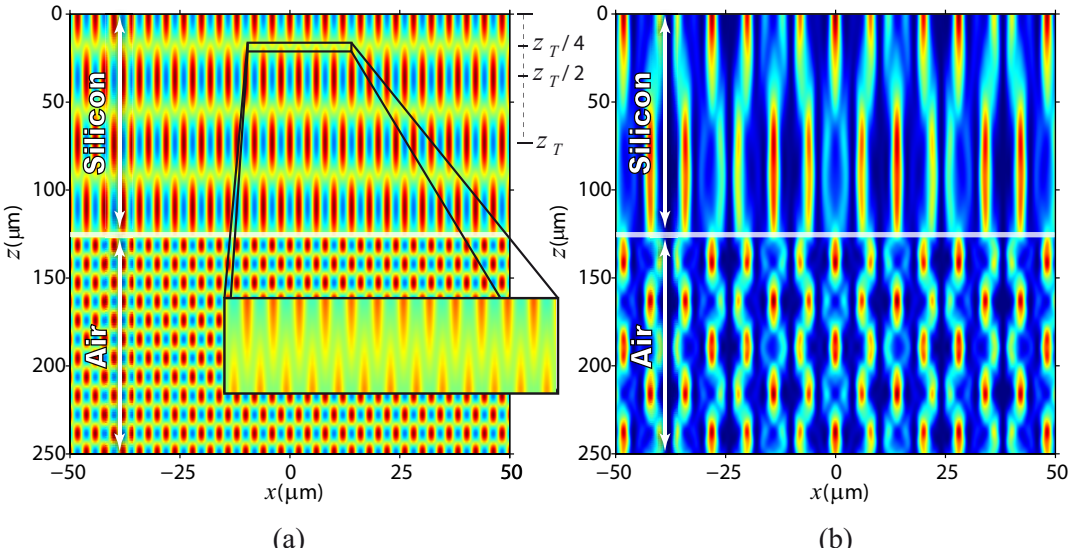

Figure 7.5: Light interference in the combiner region (silicon) and the free propagation (air) regions. (a) Talbot effect at Littrow wavelength $\lambda_L = 1500$ nm; (b) Moiré-Talbot effect at $\lambda = 1508$ nm. The silicon-air interface (spectrometer chip edge) is located at $z = 125$ μm, as it is indicated by the grey line in (a) and (b). Inset in figure (a) shows the intensity distribution at the fractional Talbot plane $z_T/4$.

Figure 7.4 shows the influence of the pitch d on spectral retrieval for three device, with values: 3 μm, 4 μm, and 5 μm, respectively. It is observed that as the pitch decreases, device dispersion increases, as in a conventional AWG. The terms (a)−(g) of Eq. (7.12) are also identified in Fig. 7.4 to help visualize the effect of varying pitch on different spatial frequencies in the Fourier spectrum.

The interference effect in the combiner region and the free propagation regions is shown in Fig. 7.5, representing a scalar optical field calculated from the Fresnel integral using the angular spectrum method, see appendix A. This method offers a fast and an accurate approximation to the Fresnel integral for generalized device geometry. The wavefront propagation simulation starts at the arrayed waveguide output aperture ($z = 0$) and terminates at $z = 250$ μm. We remark that the combiner region is a silicon slab waveguide with $n_{eff} = 3.44$ for $0 < z < 125$ μm. The combiner region (silicon) is followed by a free-propagation one (air) with $n_{eff} = 1$ for 125 μm $< z <$ 250 μm.

Fig. 7.5(a) shows the interference fringes at the Littrow wavelength of $\lambda_L = 1500$ nm, yielding the conventional Talbot effect. The inset shows the well-known frequency doubling effect at the fractional Talbot plane $z = z_T/4$. Fig. 7.5(b) shows the Moiré superposition of two Talbot effects for a wavelength of $\lambda = 1508$ nm, see Eq. (7.12).

Finally, we calculate interferogram and spectrum for a FT-AWG device with the parameters described above, for the input light comprising six monochromatic spectral lines (wavelengths): 1502 nm, 1502.3 nm, 1504 nm, 1505 nm, 1506 nm and 1508 nm. We underline that the

interference pattern

$$I(x,z) = \sum_{q=1}^{6} I\left(x, z, \lambda_q\right), \tag{7.13}$$

is sampled with a maximum spatial resolution of 130 lines/mm. Figure 7.6 and 7.7 show the interference pattern for $z = z_T$ (top panel) calculated from Eq. (7.12) and its Fourier spectrum (central and bottom panels) for unapodized and Gaussian apodized input fields, respectively. The Gaussian apodization window has a width of $w_0 = 250$ μm.

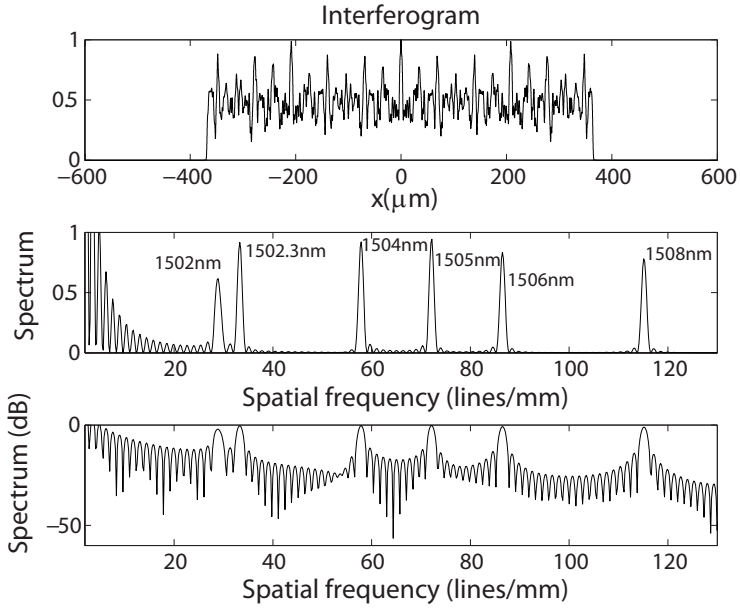

Figure 7.6: Interferogram and calculated spectrum for an FT AWG device. Unapodized input field. The interferogram at the Talbot plane $z = z_T$ (top), is calculated from Eq. (7.12). Calculated spectrum (using the FFT algorithm) for wavelengths: 1502 nm, 1502.3 nm, 1504 nm, 1505 nm, 1506 nm and 1508 nm in linear (center) and logarithmic (bottom) scales.

It is observed that the two spectral lines separated by $\Delta\lambda = 0.3$ nm are resolved well beyond the Rayleigh criterion. The Rayleigh spectral resolution is $\Delta\lambda = \lambda/R = \lambda/mN$ where m is interference order and N is the total number of interleaved waveguides, that in our device yields $\Delta\lambda \sim 0.1$ nm. The calculated spectra show that the microspectrometer crosstalk is reduced from −20 dB to −40 dB by Gaussian aperture apodization.

Similar results are obtained when the interferogram is registered at the fractional Talbot distances $z_T\eta/\zeta$. In particular, the field distribution at the fractional Talbot distance $z_T/2$ corresponds to

$$W_p(x, z_T/2) = \Phi(z_T/2) T_p\left(x - d/2 + d^2\alpha_p\right), \tag{7.14}$$

whereas for the distance $z_T/4$ the field W_p is written as follows:

$$\begin{aligned} W_p(x, z_T/4) &= \Phi(z_T/4) \sum_{a=0}^{1} B(a,1,4) T_p\left(x - \frac{d}{2} + \frac{a}{2}d + \frac{1}{2}d^2\alpha_p\right) \\ &= \frac{\Phi(z_T/4)}{\sqrt{2}}\left(\exp\left(i\pi/4\right) T_p\left(x - \frac{d}{2} + \frac{d^2\alpha_p}{2}\right) + \exp\left(-i\pi/4\right) T_p\left(x + \frac{d^2\alpha_p}{2}\right)\right). \end{aligned} \tag{7.15}$$

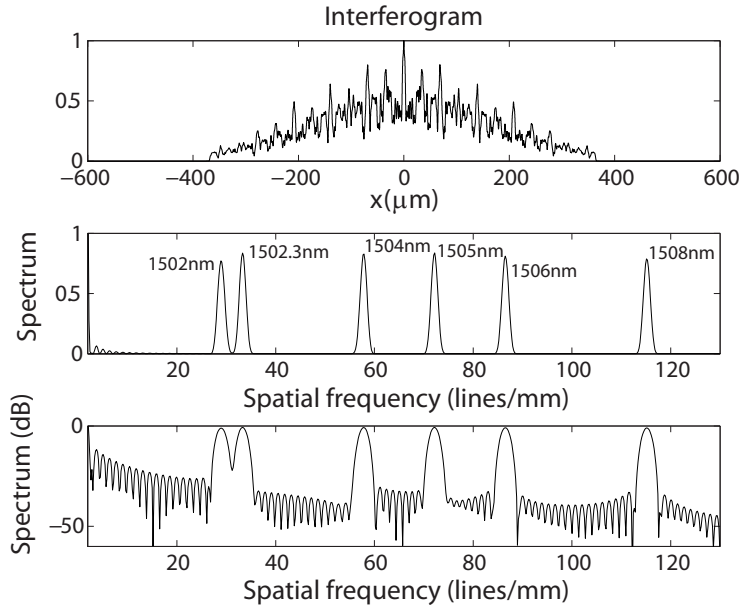

Figure 7.7: Interferogram and calculated spectrum for FT AWG device. Gaussian apodized input field. The interferogram at Talbot plane $z = z_T$ (top), is calculated from Eq. (7.12). Calculated spectrum (using the FFT algorithm) for wavelengths: 1502 nm, 1502.3 nm, 1504 nm, 1505 nm, 1506 nm and 1508 nm in linear (center) and logarithmic (bottom) scales.

Equation (7.14) corresponds to the self-image of the array grating shifted by half period ($d/2$), thus the same conclusions previously explained for Eq. (7.9) are obtained. On the other hand, Eq. (7.15) corresponds to a frequency doubling effect which is shown in the inset of Fig. 7.5 (a) for the Littrow wavelength ($\alpha(\lambda_L) = 0$).

The interferogram at this fractional Talbot distance is given by the expression:

$$\begin{aligned} I(x, z_T/4) &= \frac{1}{2}\left|\exp(i\pi/4)\left[T_1\left(x - \frac{d}{2} + \frac{d^2\alpha}{2}\right) + T_2\left(x - \frac{d}{2} - \frac{d^2\alpha}{2}\right)\right]\right. \\ &\quad \left. + \exp(-i\pi/4)\left[T_1\left(x + \frac{d^2\alpha}{2}\right) + T_2\left(x - \frac{d^2\alpha}{2}\right)\right]\right|^2 . \end{aligned} \tag{7.16}$$

In our case the condition $\alpha < 1/d$ is satisfied, which is applied into the expression Eq. (7.16) obtaining:

$$I(x, z_T/4) = (1 + \cos(2\pi 2\alpha x)) \times$$
$$\left|\exp(i\pi/4)\, t\left(x - \frac{d}{2}\right)[\cos(d\pi\alpha) + \tan(2\pi\alpha x)\sin(d\pi\alpha)] + \exp(-i\pi/4)\, t(x)\right|^2 . \tag{7.17}$$

The expression Eq. (7.17) corresponds to an interferogram containing various terms with wavelength dependent spatial frequencies of 2α, $f_d \pm 2\alpha$ and $2f_d \pm 2\alpha j$, $j = 0$ or 1, see Fig. 7.8. In contrast to the previous case described by Eq. (7.12), the interferogram represented by Eq. (7.17) does not contain the spatial frequency f_d since $\sin(d\pi\alpha) \approx d\pi\alpha$ holds for $\alpha < 1/d$ and therefore $\cos(d\pi\alpha) + \tan(2\pi\alpha x)\sin(d\pi\alpha) \approx 1 + d\pi\alpha\tan(2\pi\alpha x)$. This fact is appreciated comparing Fig. 7.8 with Fig. 7.3 (1502 nm). Figure 7.9 shows the interference pattern for $z = z_T/4$ (top panel) calculated from Eq. (7.17) and its Fourier spectrum (central and bottom panels)

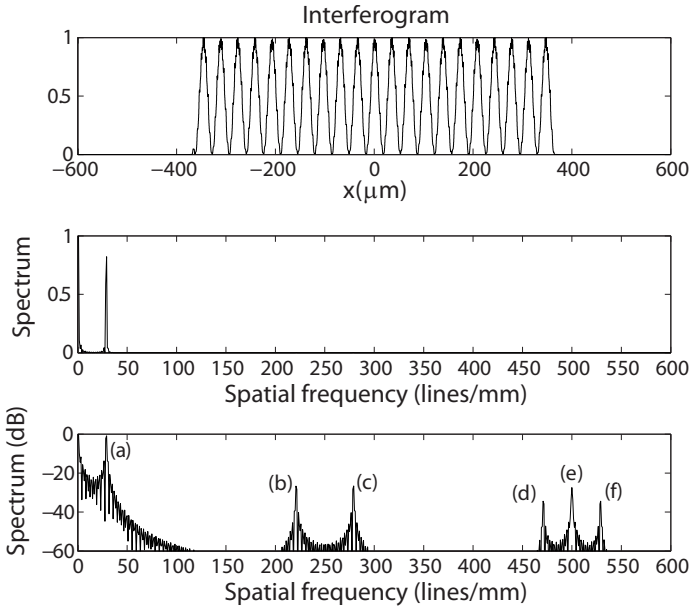

Figure 7.8: Interferogram (top) at the fractional Talbot plane $z_T/4$ calculated from Eq. (7.17) and its Fourier spectrum (center and bottom, in linear and logarithmic scales, respectively). Unapodized input field. Wavelength λ = 1502 nm. The peaks (a-f) correspond to the spatial frequencies of 2α (a), $f_d \pm 2\alpha$ (b,c) and $2f_d \pm 2\alpha j$ (d-f).

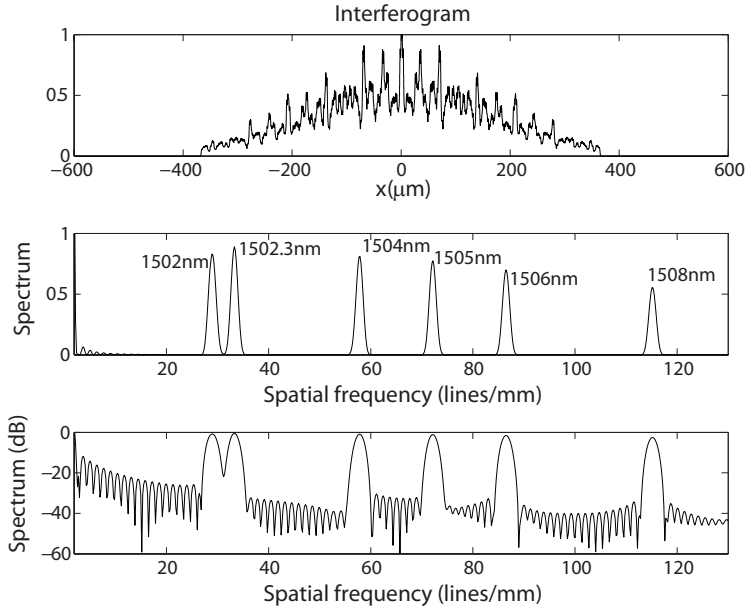

Figure 7.9: Interferogram and calculated spectrum for FT AWG device. Gaussian apodized input field. The interferogram at Talbot plane $z = z_T/4$ (top), is calculated from Eq. (7.17). Calculated spectrum (using the FFT algorithm) for wavelengths: 1502 nm, 1502.3 nm, 1504 nm, 1505 nm, 1506 nm and 1508 nm in linear (center) and logarithmic (bottom) scales.

for Gaussian apodized input field, comprising several wavelengths: 1502 nm, 1502.3 nm, 1504 nm, 1505 nm, 1506 nm and 1508 nm. The crosstalk as well as the spectral line resolution $\Delta\lambda$ demonstrated in Fig. 7.9, are similar to the result obtained previously for the non fractional Talbot distance, displayed in Fig. 7.7.

It should be noted that the distance z_T is a function of wavelength. If the interferogram is evaluated for example at Talbot plane $z = z_{T,L}$ at λ_L, at other wavelengths this position deviates by $\Delta z = z_{T,L}\ (\lambda - \lambda_L)\ /\ \lambda$. For the interleaved FT-AWG device considered in this work, the maximum spatial shift is $\Delta z_{\max} = 0.4\ \mu$m which corresponds to the wavelength $\lambda = 1508$ nm and $n_{eff} = 3.44$ (silicon region). Because the Talbot distance $z_T(\lambda_L)$ is proportional to the effective index, this factor is reduced to $\Delta z_{\max} = 0.12\ \mu$m when the interferogram is registered in the air region, that is a comparatively small value: $\Delta z_{\max}/z_{T,L} \sim 0.1\%$. According to the previous calculations, the influence of this Talbot plane shift with wavelength on spectral retrieval is negligible, as it is evident comparing the spectra in Fig. 7.7 and Fig. 7.9. The two spectra are virtually identical, but they correspond to rather different positions, namely at z_T (Fig. 7.7) and $z_T/4$ (Fig. 7.9).

7.2.2 Interferogram sampling effects

Because it is not required for understanding of the FT-AWG device performance, here we will briefly consider the effect of interferogram sampling as an example. Using an photodetector array (e.g., infrared CCD chip) is a convenient way to sample the interferogram.

Figure 7.10 shows the influence of the interferometer sampling frequency on the spectral retrieval for an interference pattern sampled by a photodetector array with periods 4 μm, and 5 μm, respectively. No deterioration of the calculated spectrum is noticed at the sampling period of 4 μm which corresponds to the minimun pixel size of commonly used CCD sensor. For the sampling period of 5 μm, four satellite peaks appear in the calculated spectrum as the result of undersampling.

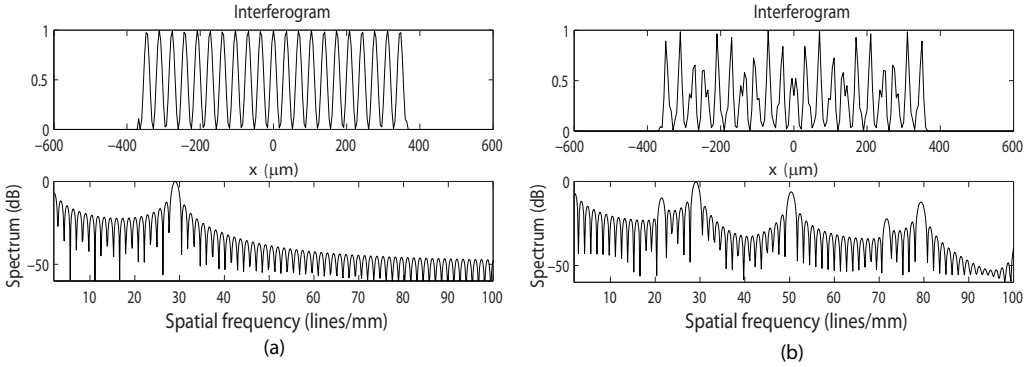

Figure 7.10: Influence of interferogram sampling on spectrum retrieval. Gaussian unapodized input field. The interferogram (top) at Talbot plane $z = z_T$. Calculated spectra for the wavelength of 1502 nm and different sampling frequencies (bottom); sampling periods 4 μm (a), 5 μm (b).

Thus, for this device example, a spatial sampling period of 4 μm suffices for accurate spectral retrieval. Another techniques can also be used for sampling the interferogram. For example, the AWG device dispersion can be designed such that the interferogram maximum spatial frequency is still resolved by the photodetector array. The AWG dispersion can be controlled by modifying the interference order m or waveguide pitch d, see Eq. (7.2). Alternatively, imaging optics at the chip output can be used to match the interference pattern to the pitch of the photodetector array.

7.3 Conclusions

We have presented an optimized FT-AWG microspectrometer operating in transmission geometry. The device performance as well as the interference effects were explained by an analytical formalism and were confirmed by numerical simulations. The retrieval of spectral information in a FT-AWG device with Rayleigh resolution of $\Delta\lambda = 0.1$ nm, 8 nm bandwidth, and a Littrow wavelength of $\lambda = 1500$ nm, was also illustrated by numerical simulations. A spectral resolution $\Delta\lambda = 0.3$ nm and a crosstalk level reduction to -40 dB were also obtained for a Gaussian apodized input field. These results demonstrate a significant crosstalk supression as well as the device feasibility. This work was reported in [139].

Conclusions

1. On the basis of matrix formalism, we have designed a flexible optical system able to perform three basic ortho-symplectic transformations in phase space. Several useful equations that connect the parameters of the transformation matrix for a general and anamorphic first-order optical system, have been derived. The optical setup performing such transformations; image rotation, separable FRFT and GT, is constructed by the combination of generalized lenses (assembled set of cylindrical lenses) and free-space intervals. We have demonstrated that the separable FRFT as well as GT corresponds to a symmetric setup constructed by three generalized lenses and two free-space intervals, whereas the rotator setup is achieved by a nonsymmetric setup constructed by four lenses and four space-intervals. The transformation parameters are reached by the proper rotation of the cylindrical lenses or varying their lens power, where the free-space intervals are fixed. Their optical implementation has been studied in detail as well.

2. Main properties of the GT such as shift, scaling, plane wave modulation, Parseval theorem and the GT of the selected functions, have been derived.

3. The application of GT operation as a mode converter of a wide spectrum of stable modes and for image processing: shift-variant filtering, hyperbolic noise reduction and image encryption, have been demonstrated.

4. We have implemented two optical setups: one for interactive complex field generation based on two coupled SLMs, and another one for the GT operation. Both systems operate almost at real time. The experimental implementation of GT has been demonstrated for the mode transformation of Hermite-Gaussian (generated by using the proposed SLM setup) into Laguerre-Gaussian modes. The experimental results are in excellent agreement with the theoretical predictions attesting the feasibility of both setups. These systems promises to be a useful tool for optical processing applications. To the best of our knowledge it is the first time that these systems are achieved.

5. Several programs have been developed by us for the numerical simulation of these first-order systems. The numerical results deal with the theoretical predictions.

6. Finally, we have presented an optimized Fourier-transform AWG microspectrometer design operating in transmission geometry. The device performance as well as the interference effects were explained by an analytical formalism and was confirmed by numerical simulations. This optical design for parameters such as Rayleigh resolution of $\Delta\lambda = 0.1$ nm, 8 nm bandwidth, and a Littrow wavelength of $\lambda = 1500$ nm, lead to the retrieval of spectral information with a spectral resolution $\Delta\lambda = 0.3$ nm and a crosstalk level reduction to -40 dB. The results demonstrate high crosstalk supression as well as the device feasibility.

Appendix A

Numerical approach for the Fresnel diffraction integral calculation

This appendix is devoted to discuss briefly the numerical approach for the Fresnel integral calculation, that has been used for the numerical simulations considered in this work. Let us first remind the Fresnel integral:

$$f_o(\mathbf{r}_o; z) = \frac{\exp\,(ikz)}{i\lambda z} \iint f_i(x_i, y_i; z = 0) \exp\left(i\pi \frac{(x_o - x_i)^2 + (y_o - y_i)^2}{\lambda z}\right) \mathrm{d}x_i \mathrm{d}y_i, \tag{A.1}$$

where $f(\mathbf{r}; z)$ is the complex field amplitude, $\mathbf{r}^t_{i,o} = (x_{i,o}, y_{i,o})$ are the input−output spatial coordinates, z is the propagation distance, and λ is the wavelength. As it is well-known Eq. (A.1) corresponds to the convolution between the input filed $f_i(\mathbf{r}_i; z = 0)$ and a spherical wave, and it can be evaluated applying different techniques [140]. In the case corresponding to the near-field diffraction regime, the most suitable technique is the angular spectrum method which permits a fast an accurate calculation. Thus instead of directly calculating of this integral, whose integrant for short distance z is rapidly oscillanting, one can calculate the product of the Fourier transforms (angular spectrum) of $f_i(\mathbf{r}_i; z = 0)$ and $\exp\left(i\pi(x^2 + y^2)/\lambda z\right)$, and finally perform the inverse Fourier transform to obtain the output field. This computation algorithm is achieved by using the fast Fourier transform (FFT) technique which leads to both a fast and accurate approximation. In other words this procedure is written as follows:

$$f_o(\mathbf{r}_o; z) = \mathrm{IFFT}\left\{\mathrm{FFT}\left\{f_i(\mathbf{r}_i; z = 0)\right\} \mathrm{H}(u, v)\right\}, \tag{A.2}$$

where

$$\mathrm{H}(u, v) = C \exp\left(-i\pi(u^2 + v^2)\lambda z\right), \tag{A.3}$$

is the Fourier transform of $\exp\left(i\pi(x^2 + y^2)/\lambda z\right)$, C is a complex constant, and u and v are the spatial frequencies.

It is well-known that the angular spectrum method must be applied for short propagation distances given by the condition $z < z_c$, whereas a direct evaluation of the Fresnel integral is suitable for distances $z \geq z_c$, where $z_c = 2\delta a/\lambda$ [140, 141], δ is the finest detail and a is the aperture size, both corresponding to the input filed. If $z \geq z_c$ the direct Fresnel integral approach have to be used, which is given by

$$f_o(\mathbf{r}_o; z) = C \exp\left(-i\pi(x_o^2 + y_o^2)/\lambda z\right) \mathrm{FFT}\left\{f_i(\mathbf{r}_i; z = 0) \exp\left(i\pi(x_i^2 + y_i^2)/\lambda z\right)\right\}. \tag{A.4}$$

For a given number of points or pixels, N, the computing effort is $2N \log N + N$ and $N \log N + 2N$ for the angular spectrum and the direct evaluation approaches, respectively.

Notice that, for both regions, the computing effort is smaller than other numerical methods of evaluating Fresnel-type integrals. To increase the accuracy, the space propagation interval z can be achieved by m steps such as $z/m << z_c$.

We have developed a numerical application that allows us to simulate the light propagation for both regimes. Its feasibility have been demonstrated in different applications. This numerical approach has been used for the simulation of the FT-AWG microspectrometer device proposed in the latter chapter. Moreover the combination of free-space propagation together with phase field modulation, which simulate the lens action, permits to describe the light propagation at almost any first-order optical system. In particular, this algorithm has been used for the numerical simulation of the optical systems corresponding to the separable FRFT, image rotation and GT operations.

Appendix B

Gyrator transform properties

In this appendix we provide the intermediate calculations corresponding to the gyrator transform properties discussed in chapter 4.

B.0.1 Shift theorem for gyrator transform

As we have mentioned the GT is a linear canonical integral transformation described by orthogonal and symplectic ray transformation matrix. In particular the gyrator transform [Eq. (4.1)] can be rewritten as follows:

$$\begin{aligned} f_o(\mathbf{r}_o) &= R^{\alpha}[f_i(\mathbf{r}_i)](\mathbf{r}_o) \\ &= \frac{1}{|\sin\alpha|}\int f_i(\mathbf{r}_i)\,\exp\left(i\pi\left[\mathbf{r}_i^t\mathbf{Y}^{-1}\mathbf{X}\mathbf{r}_i - 2\mathbf{r}_i^t\mathbf{Y}^{-1}\mathbf{r}_o + \mathbf{r}_o^t\mathbf{X}\mathbf{Y}^{-1}\mathbf{r}_o\right]\right)\mathrm{d}\mathbf{r}_i, \end{aligned} \tag{B.1}$$

where $\mathbf{X}$ and $\mathbf{Y}$ are defined by Eq. (1.17). Here t stands for transposition operation, and α is the transformation angle.

The shift theorem can be easily demonstrated thanks to the latter equation, where the input complex field amplitude $f_i(\mathbf{r}_i)$ is shifted at $\mathbf{v}^t = (v_x, v_y)$. Let us start considering the following relation

$$\begin{aligned} f_o(\mathbf{r}_o) &= \frac{1}{|\sin\alpha|}\int f_i(\mathbf{r}_i-\mathbf{v})\,\exp\left(i\pi\left[\mathbf{r}_i^t\mathbf{Y}^{-1}\mathbf{X}\mathbf{r}_i - 2\mathbf{r}_i^t\mathbf{Y}^{-1}\mathbf{r}_o + \mathbf{r}_o^t\mathbf{X}\mathbf{Y}^{-1}\mathbf{r}_o\right]\right)\mathrm{d}\mathbf{r}_i \\ &= \frac{1}{|\sin\alpha|}\int f_i(\mathbf{u})\,\exp\left(i\pi\left[(\mathbf{u}+\mathbf{v})^t\,\mathbf{Y}^{-1}\mathbf{X}\,(\mathbf{u}+\mathbf{v}) - 2\,(\mathbf{u}+\mathbf{v})^t\,\mathbf{Y}^{-1}\mathbf{r}_o + \mathbf{r}_o^t\mathbf{X}\mathbf{Y}^{-1}\mathbf{r}_o\right]\right)\mathrm{d}\mathbf{u} \\ &= \frac{1}{|\sin\alpha|}\int f_i(\mathbf{u})\,\exp\left(i\pi\phi\right)\mathrm{d}\mathbf{u}. \end{aligned} \tag{B.2}$$

in which the kernel $\exp\left(i\pi\phi\right)$ is simplified to

$$\begin{aligned} \exp\left(i\pi\phi\right) = \exp\Big(i\pi(\mathbf{v}^t\mathbf{Y}\mathbf{X}\mathbf{v} + \mathbf{r}_o^t[(\mathbf{X}\mathbf{Y}^{-1}\mathbf{X} - (\mathbf{Y}^{-1})^t - \mathbf{Y}]\mathbf{v})\Big) \\ \times\exp\Big(i\pi\left(\mathbf{r}_i^t\mathbf{Y}^{-1}\mathbf{X}\mathbf{r}_i - 2\mathbf{r}_i^t\mathbf{Y}^{-1}\,(\mathbf{r}_o-\mathbf{X}\mathbf{v}) + (\mathbf{r}_o-\mathbf{X}\mathbf{v})^t\,\mathbf{X}\mathbf{Y}^{-1}\,(\mathbf{r}_o-\mathbf{X}\mathbf{v})\right)\Big), \end{aligned} \tag{B.3}$$

where $\mathbf{u} = \mathbf{r}_i - \mathbf{v}$, and $\mathbf{I}$ is a unity 2×2 matrix. The following relations

$$\begin{aligned} \mathbf{v}^t\mathbf{Y}^{-1}\mathbf{X}\mathbf{u} = \mathbf{u}^t\left(\mathbf{Y}^{-1}\mathbf{X}\right)^t\mathbf{v} = \mathbf{u}^t\mathbf{X}^t\left(\mathbf{Y}^{-1}\right)^t\mathbf{v}, \\ \mathbf{X}\mathbf{Y}^t = \mathbf{Y}\mathbf{X}^t, \\ \mathbf{X}^t\mathbf{X} + \mathbf{Y}^t\mathbf{Y} = \mathbf{I}. \end{aligned} \tag{B.4}$$

are satisfied. The Eq. (B.3) can be written as a product of two exponential functions: the first one corresponds to an additional phase factor that can be extracted from the integral in Eq. (B.2), and the second one corresponds to the gyrator kernel where the coordinate $\mathbf{r}_o$ is replaced by $\mathbf{r}_o - \mathbf{Xv}$. Doing this we obtain the shift theorem as it was formulated in Eq. (4.6):

$$\begin{aligned} f_o(\mathbf{r}_o) &= R^{\alpha}[f_i(\mathbf{r}_i - \mathbf{v})](\mathbf{r}_o) \\ &= \exp\left(i\pi(\mathbf{v}^t\mathbf{YXv} + \mathbf{r}_o^t[(\mathbf{XY}^{-1}\mathbf{X} - (\mathbf{Y}^{-1})^t - \mathbf{Y}]\mathbf{v})\right) R^{\alpha}[f_i(\mathbf{r}_i)](\mathbf{r}_o - \mathbf{Xv}) \\ &= \exp\left(i\pi(v_x v_y \sin 2\alpha - 2\mathbf{r}_o\widetilde{\mathbf{v}}\sin\alpha)\right) R^{\alpha}[f_i(\mathbf{r}_i)](\mathbf{r}_o - \mathbf{v}\cos\alpha), \end{aligned} \tag{B.5}$$

where $\widetilde{\mathbf{v}} = (v_y, v_x)$.

In other words, we conclude that the shift of the input function $f_i(\mathbf{r})$ at vector $\mathbf{v}^t = (v_x, v_y)$ leads to the shift of its GT at $\mathbf{v}\cos\alpha$ and an additional linear phase modulation.

B.0.2 Scaling theorem for gyrator transform

For the case of the scaling theorem the input function is affected by a scaling factor, $f_i(\mathbf{Sr}_i) = f_i(s_x x_i, s_y y_i)$. Therefore applying a change of variables $x_i' = s_x x_i$, $y_i' = s_y y_i$ for Eq. (4.1), we obtain:

$$\begin{aligned} f_o(\mathbf{r}_o) = R^{\alpha}[f_i(\mathbf{Sr}_i)](\mathbf{r}_o) = \frac{\exp\left(i2\pi x_o y_o \cot\alpha\right)}{s_x s_y\,|\sin\alpha|} \iint f_i(x_i', y_i') \\ \times \exp\left(i2\pi\left(x_i' y_i' \frac{\cot\alpha}{s_x s_y} - \frac{1}{\sin\alpha}\left(\frac{x_i' y_o}{s_x} + \frac{x_o y_i'}{s_y}\right)\right)\right) \mathrm{d}x_i' \mathrm{d}y_i'. \end{aligned} \tag{B.6}$$

The next step is to define $\cot\beta = \cot(\alpha)/\left(s_x s_y\right)$, then the latter equation is rewritten as it follows:

$$\begin{aligned} f_o(\mathbf{r}_o) &= \frac{\exp\left(i2\pi x_o y_o \cot\alpha\right)}{s_x s_y\,|\sin\alpha|} \iint f_i(x_i', y_i') \\ &\times \exp\left(i2\pi\left(x_i' y_i' \cot\beta - \frac{1}{\sin\alpha}\left(\frac{x_i' y_o}{s_x} + \frac{x_o y_i'}{s_y}\right)\right)\right) \mathrm{d}x_i' \mathrm{d}y_i' \\ &= \frac{\exp\left(i2\pi x_o y_o \cot\alpha\right)\left|\sin\beta\right|}{s_x s_y\,|\sin\alpha|} \exp\left(-i2\pi\cot\beta\frac{y_o x_o \sin^2\beta}{s_x s_y \sin^2\alpha}\right) \\ &\times R^{\beta}[f_i(\mathbf{r}_i)]\left(\frac{x_o\sin\beta}{s_y\sin\alpha}, \frac{y_o\sin\beta}{s_x\sin\alpha}\right) \\ &= \frac{\sigma_\beta\cos\beta}{\sigma_\alpha\cos\alpha} \exp\left(i2\pi x_o y_o\cot\alpha\left(1 - \left(\frac{\cos\beta}{\cos\alpha}\right)^2\right)\right) R^{\beta}[f_i(\mathbf{r}_i)]\left(\frac{\cos\beta}{\cos\alpha}\mathbf{Sr}_i\right), \end{aligned} \tag{B.7}$$

where $\sigma_\alpha = \mathrm{sgn}(\sin\alpha)$, $\sigma_\beta = \mathrm{sgn}(\sin\beta)$. Therefore we conclude that the GT at angle α of a scaled input function, $f_i(\mathbf{Sr}_i)$, corresponds to the GT at angle β of the initial function $f_i(\mathbf{r}_i)$ with an additional scaling of the output coordinates and hyperbolic wave modulation.

B.0.3 Gyrator transform of selected functions, Table 4.3

Here we present the intermediate calculations for the GT of selected functions, shown in Table 4.3. We remark that the GT of the Dirac delta function (row 1, Table 4.3) is obtained directly applying the properties of the δ-function.

GT of hyperbolic phase function

The GT of hyperbolic phase function (row 2, Table 4.3) and the constant function 1 (row 3, Table 4.3) are obtained from

$$R^{\alpha}[\exp(i2\pi c x_i y_i)](\mathbf{r}_o) = \frac{\exp(i2\pi x_o y_o \cot\alpha)}{|\sin\alpha|} g(\mathbf{r}_o), \tag{B.8}$$

where the function $g(\mathbf{r}_o)$ is calculated as it follows:

$$\begin{aligned} g(\mathbf{r}_o) &= \iint \exp\left(i2\pi\left(x_i y_i (c+\cot\alpha) - \frac{1}{\sin\alpha}(x_i y_o + x_o y_i)\right)\right) \mathrm{d}x_i \mathrm{d}y_i \\ &= \int \exp\left(-i2\pi \frac{x_o y_i}{\sin\alpha}\right) \mathrm{d}y_i \int \exp\left(i2\pi x_i \left(y_i (c+\cot\alpha) - \frac{y_o}{\sin\alpha}\right)\right) \mathrm{d}x_i \\ &= \int \exp\left(-i2\pi \frac{x_o y_i}{\sin\alpha}\right) \delta\left(y_i (c+\cot\alpha) - \frac{y_o}{\sin\alpha}\right) \mathrm{d}y_i \\ &= \exp\left(-i2\pi \frac{x_o y_o}{(c+\cot\alpha)\sin^2\alpha}\right). \end{aligned} \tag{B.9}$$

In the latter calculation, the expression

$$\delta(v) = \int \exp(i2\pi v x)\ \mathrm{d}x, \tag{B.10}$$

has been used. Applying trigonometric relations, the Eq. (B.8) is finally reduced to

$$R^{\alpha}[\exp(i2\pi c x_i y_i)](\mathbf{r}_o) = \frac{1}{|\sin\alpha|} \exp\left(i2\pi \frac{c\cot\alpha - 1}{c+\cot\alpha} x_o y_o\right). \tag{B.11}$$

A change of variable: $x'_o = x_o + k_y \sin\alpha$, and $y'_o = y_o + k_x \sin\alpha$ together with the Eq. (B.10) allow to calculate the GT of a plane wave (row 4, Table 4.3).

GT of spherical wavefront and a Gaussian function

The GT of a spherical wavefront and a Gaussian function, (row 5 and 6 in Table 4.3, respectively) can be derived as particular cases of the GT of $\exp\left(\gamma \mathbf{r}_i^2\right)$, which is given by

$$f_o(x_o, y_o) = \frac{1}{|\sin\alpha|} \exp(i2\pi x_o y_o \cot\alpha)\, g_o(x_o, y_o), \tag{B.12}$$

where

$$\begin{aligned} g_o(x_o, y_o) &= \iint \exp\left(\gamma \mathbf{r}_i^2\right) \exp\left(i2\pi\left(x_i y_i \cot\alpha - \frac{1}{\sin\alpha}(x_i y_o + x_o y_i)\right)\right) \mathrm{d}x_i \mathrm{d}y_i \\ &= \int \exp\left(x_i^2\gamma\right) \exp\left(-i2\pi \frac{x_i y_o}{\sin\alpha}\right) \mathrm{d}x_i \int \exp\left(y_i^2\gamma\right) \exp\left(i2\pi\left(x_i\cot\alpha - \frac{x_o}{\sin\alpha}\right) y_i\right) \mathrm{d}y_i \\ &= \sqrt{\frac{\pi}{-\gamma}} \int \exp\left(x_i^2\gamma\right) \exp\left(\frac{\pi^2}{\gamma}\left(x_i\cot\alpha - \frac{x_o}{\sin\alpha}\right)^2\right) \exp\left(-i2\pi \frac{x_i y_o}{\sin\alpha}\right) \mathrm{d}x_i, \end{aligned} \tag{B.13}$$

$\gamma = -\pi(a + ib)$, and $a \geq 0$. It should be noted that Eq. (B.13) has been obtained by using [142]

$$\int \exp\left(\mu x^2 + \beta x\right) dx = \sqrt{\frac{\pi}{-\mu}} \exp\left(-\frac{\beta^2}{4\mu}\right), \tag{B.14}$$

for the integral calculation with respect to y_i, where $\mathrm{Re}(\mu) \leq 0$. It implies that the condition $\mathrm{Re}(\gamma) \leq 0$ must be satisfied. Moreover, the integral calculation with respect to x_i can be realized by using a change of variable $t = x_i\sqrt{\gamma}$, and applying again the Eq. (B.14). It permits to reduce the Eq. (B.13) to:

$$g_o(x_o, y_o) = \sqrt{\frac{\pi^2}{\gamma^2 d}} \exp\left(\frac{\pi^2}{\gamma d \sin^2\alpha}\left(x_o^2 + y_o^2\right)\right) \exp\left(-i2\pi \frac{\pi^2}{d\gamma^2 \sin^2\alpha} x_o y_o \cot\alpha\right), \tag{B.15}$$

where $d = 1 + \left(\pi \cot(\alpha)/\gamma\right)^2$.

Therefore the GT of $\exp\left(\gamma \mathbf{r}_i^2\right)$ is written as follows

$$\begin{aligned} f_o(\mathbf{r}_o) &= R^{\alpha}[\exp\left(\gamma \mathbf{r}_i^2\right)](\mathbf{r}_o) \\ &= \frac{1}{\sqrt{\cos^2\alpha + (\gamma/\pi)^2 \sin^2\alpha}} \exp\left(i2\pi\left(1 - \frac{1}{\cos^2\alpha + (\gamma/\pi)^2 \sin^2\alpha}\right) x_o y_o \cot\alpha\right) \\ &\quad \times \exp\left(\frac{\gamma \mathbf{r}_o^2}{\cos^2\alpha + (\gamma/\pi)^2 \sin^2\alpha}\right). \end{aligned} \tag{B.16}$$

The GT of the spherical wave and Gaussian function (row 5 and 6 in Table 4.3) are derived from this expression for the case $\gamma = -i\pi b$ and $\gamma = -\pi a$, correspondingly.

Appendix C

System for optical field generation based on two coupled SLMs

A spatial light modulator (SLM) is an optical device that modulates a beam of light almost at real time. In general, a SLM only modulates the intensity or phase distribution of a coherent beam.

SLM-LC, that means SLM based on the liquid crystal display (LCD) technology, is being extensively used for prototyping in industrial development and research; in particular for optical information processing, holography, optical trapping, etc. It is due to the significant improvements of the LCD technology that allows to design high resolution devices at low cost. A SLM-LC is an electrically addressed device that modulates the phase or intensity distribution of a coherent light beam as a function of its polarization state. In contrast to transmission SLM-LC devices, the reflection SLM-LCOS (LC on Silicon chip) offers a high energy-efficiency as well as fill factor close to 95% which are demanded in many optical applications. Notice that a high fill factor implies negligible pixelation effects. Therefore SLM-LCOS device promises to be an useful and versatile tool, that is also being widely adopted by the optical community.

An optical setup for complex field generation based on two coupled SLM-LCOS (Holoeye LCR-2500) was introduced in chapter 6. This optical configuration is known as a hybrid hologram [128] since the amplitude and phase components of the input signal are separately implemented on each SLM, see Fig. C.1. The amplitude component is projected by means of a 4-f lens system on the second SLM, which introduces the appropriate phase modulation. Meanwhile, the second 4-f lens system is used in order to remove in the Fourier plane the non-zero diffraction orders, arising due to the discrete structure of the SLMs. We remark that the optical path among the Fourier lens L with the SLM equals its focal distance f. In this configuration, each SLM is operating in amplitude or phase modulation depending on the polarization state of the incident beam, which is set by using $\lambda/2$ wave-plates (WP) and analyzers. In particular, the first and second SLM operate in amplitude and phase-only, correspondingly.

Position stages for these SLMs are not required because the alignment between amplitude and phase components are digitally achieved by means of a PC, which simplifies significantly the optical setup. The alignment accuracy is limited by the pixel size, which is 20 μm in our case (Holoeye LCR-2500 SLM, see Table C). The signal quality is also limited by the spatial resolution and in addition by the dynamic range of the SLM (8-bits). This setup permits to generate a complex filed amplitude at almost real time, which plays an important role in optical information processing.

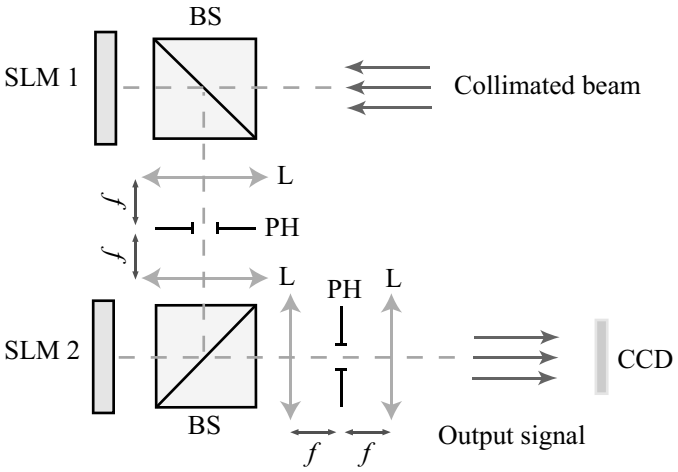

(a)

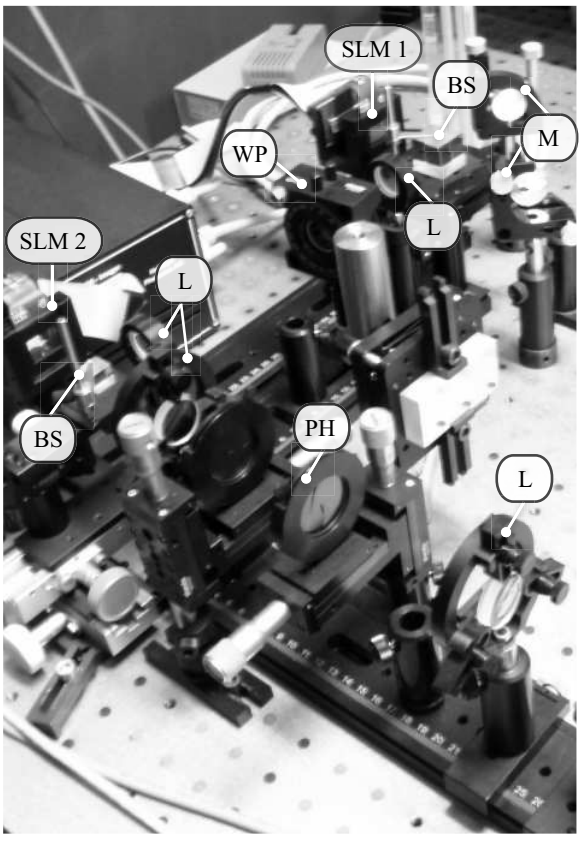

(b)

Figure C.1: Optical setup scheme (a) corresponing to the experimetal setup (b) based on two SLMs (Holoeye LCR-2500) for an arbitrary complex field generation. BS is a beam splitter. A pin-hole PH is placed at the Fourier plane of the 4-f system, where L is a Fourier lens. WP denotes a $\lambda/2$ wave-plate while M is a dichroic mirror.

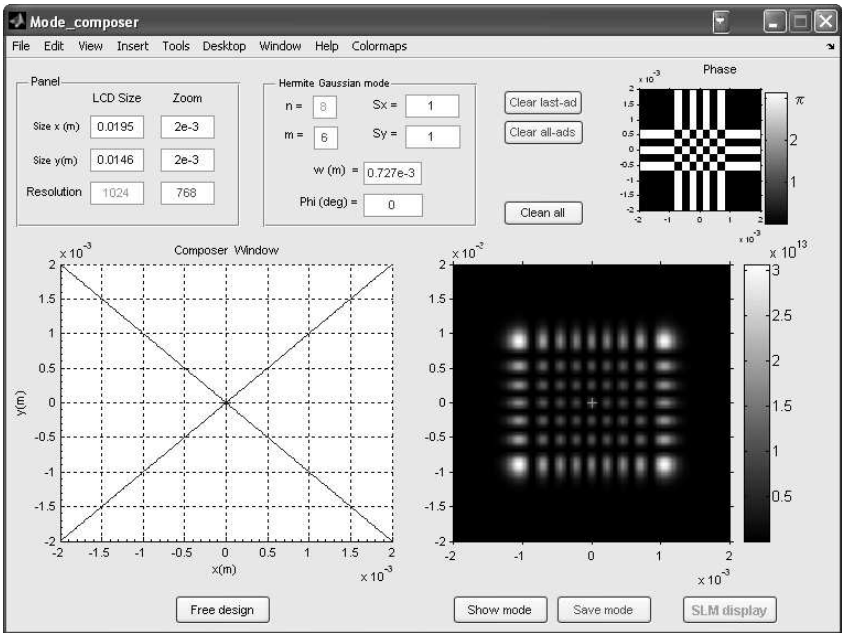

(a)

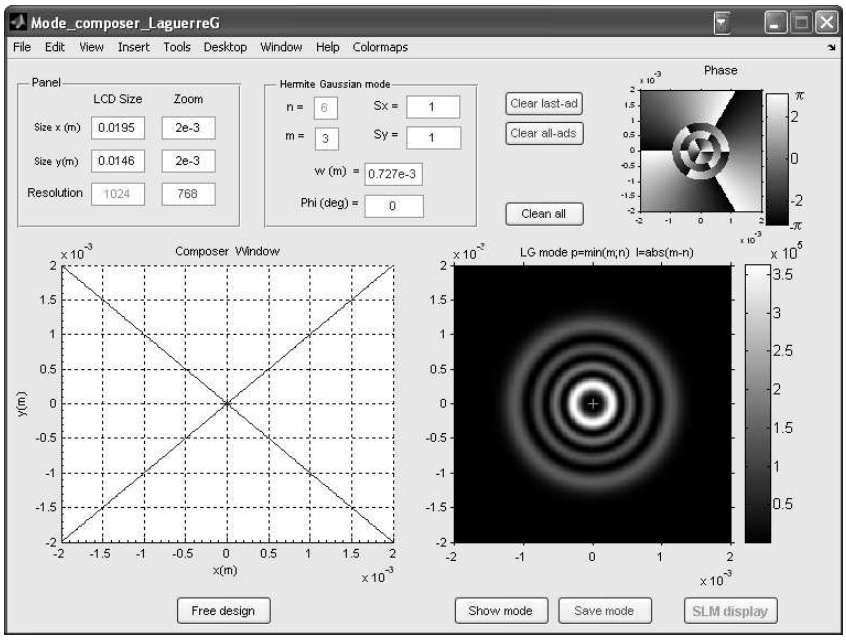

(b)

Figure C.2: Graphical user interface applications. This software permits the implementation of the Hermite-Gauss (a) and Laguerre-Gauss (b) modes for different parameters: mode indices, scaling, beam waist, rotation angle. Complex mode compositions can be also achieved which are designed interactively trough the composer window.

Number of pixels	Pixel Pitch	Fill factor	Active area	Frame rate
1024×768	19 μm	93%	9.5×14.6 mm	72 Hz

Table C. SLM: 2π phase shift between 400 and 700 nm and intensity contrast ratio of 1000:1 at 532 nm

For the optical implementation of the complex field, we have developed a particular numerical application based on Matlab and Java code. This software permits to sent a RGB video signal in DVI format (video interface standard), manipulate digitally an arbitrary signal, SLM response correction (gamma-correction, etc.), and other basic operations. As an example, in Fig. C.2 the graphical user interface application (developed by us) is shown for the case of the Hermite-Gaussian (a) and Laguerre-Gaussian (b) modes, correspondingly. This application allows us to realize different operations such as digital alignment and varying several parameters: mode index, beam waist, nonsymmetric scaling, rotation, as well as to draw complex mode composition, see Fig. C.2 and Fig. C.3. Note that the SLM display resolution can be adjusted for the corresponding SLM model, see for example Fig. C.3 (first control panel).

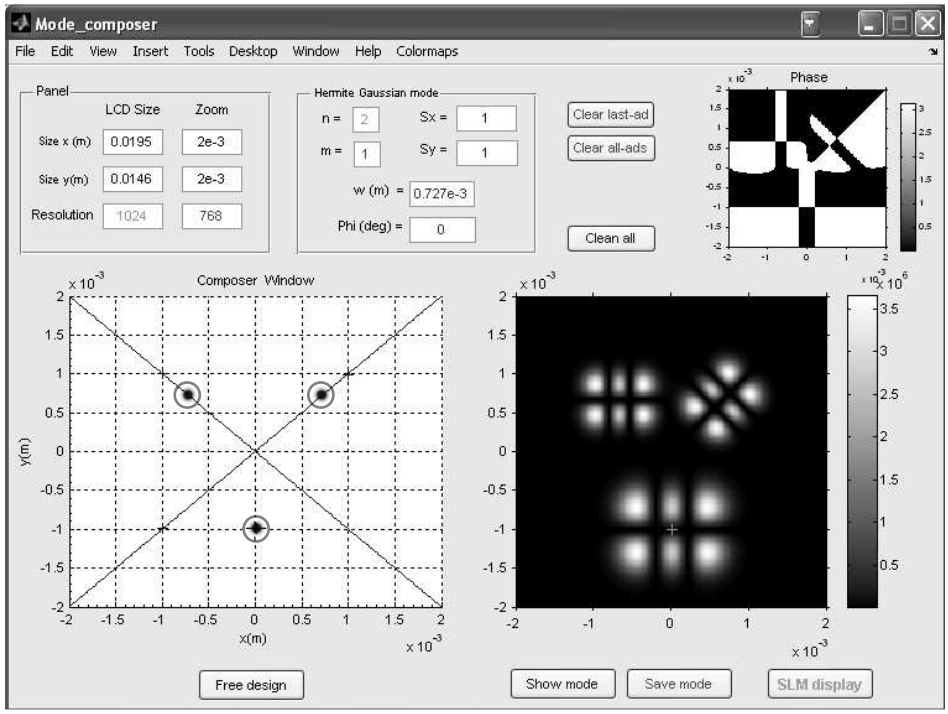

Figure C.3: Example of array composition for the case of $HG_{2,1}$. As it is observed each mode has been placed in different positions by using the composer window panel. The composition consists of the $HG_{2,1}$ modes rotated at angle $\pi/4$ and scaled by a $\times 2$ factor, as it is observed.

We remark that in contrast to other setup configurations, the alignment among the amplitude and phase distribution of the signal is implemented digitally. This alignment operation is achieved by centering the matrices corresponding to each signal component: green and red channel for the amplitude and phase distributions, respectively. This idea is illustrated in Fig. C.4 for two particular examples of SLMs misalignment. This approach is part of the calibration procedure which is achieved by using this software.

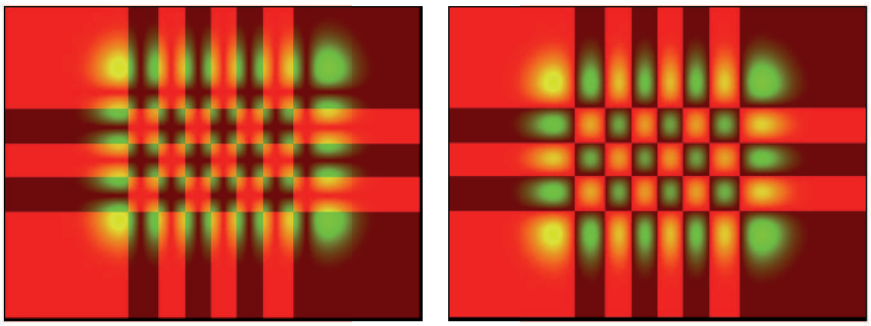

(a) (b)

Figure C.4: Examples illustrating the alignment among signal components associated to $HG_{7,4}$ mode. As mentioned, this digital alignment is achieved by varying the centering of both DVI color channels: green and red for the amplitude and phase distributions (matrices), respectively. The misalignment among the SLMs is compensated by adjusting these matrices as it is displayed in (a) and (b) for two particular cases.

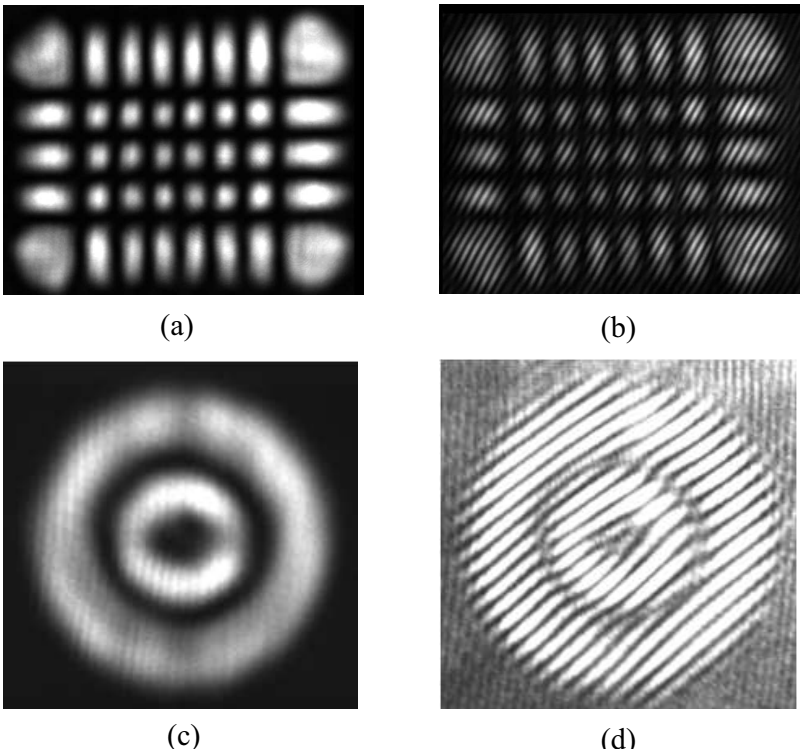

(a) (b)

(c) (d)

Figure C.5: Intensity distribution for the case of $HG_{7,4}$ (a) and $LG_{1,2}$ mode (c). The interferograms for these modes with a collimated laser beam are displayed in (b) for $HG_{7,4}$ and (d) for the $LG_{1,2}$. Image (d) reveals a fork-like structure, typical for the associated helicoidal phase distribution, which is not present for the case of $HG_{7,4}$ (b). These images were registered by a CCD camera (Sony XCD-X710).

The intensity distribution of the $HG_{7,4}$ and $LG_{1,2}$ mode and its phase structure, in the form of the interferogram with a collimated beam, are displayed in Fig. C.5. These results demonstrate an excellent agreement with the theoretical predictions as well as the feasibility of the proposed setup.

Figure C.6 displays two examples illustrating the mode composition reached by using this approach: $HG_{5,2}(\mathbf{r}) + HG_{2,5}(\mathbf{r})$ (a) and $HG_{8,6}\left(\mathfrak{R}^{-\frac{\pi}{4}}\mathbf{r}\right) + HG_{8,6}(\mathbf{r})$ (b). Note that $\mathfrak{R}^{-\frac{\pi}{4}}$ indicates the coordinate rotation at angle $-\pi/4$. These results are in excellent agreement with the theoretical predictions which are displayed in Fig. C.6 (b) and (d), correspondingly.

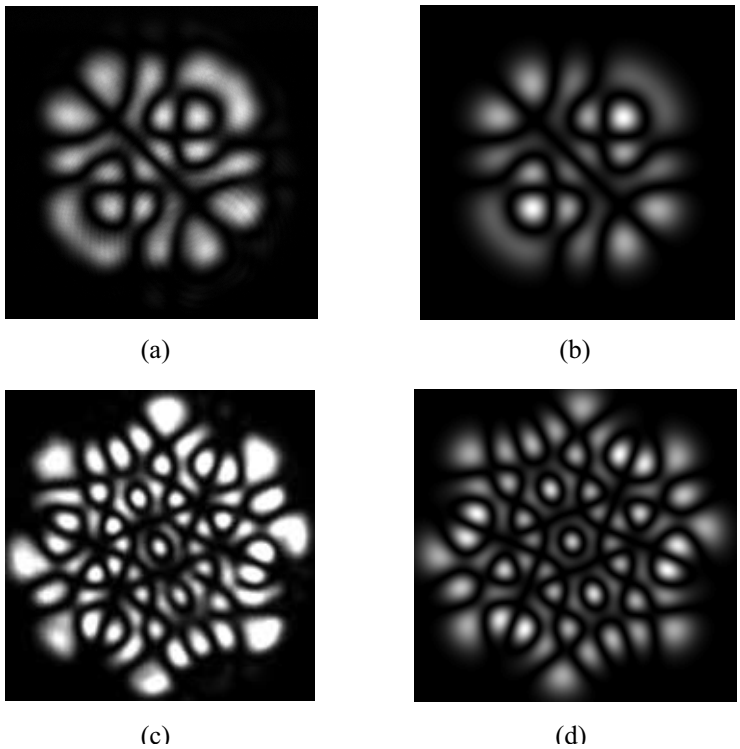

Figure C.6: Intensity distribution associated to the mode composition $HG_{5,2}(\mathbf{r}) + HG_{2,5}(\mathbf{r})$ (a, b) and $HG_{8,6}\left(\mathfrak{R}^{-\frac{\pi}{4}}\mathbf{r}\right) + HG_{8,6}(\mathbf{r})$ (c, d). The experimental results are displayed in (a) and (c), correspondingly.

In conclusion, this mode generation approach at quasi-real time is more versatile than other techniques used in digital holography or diffractive optical elements (DOE) [128]. It is a promising and useful tool for many processing applications. Other signal types such as phase modulation functions associated to generalized lens can be also implemented by using this setup. To the best of our knowledge it is the first time that this method for SLM coupling is used.

Acknowledgements

I would like to thank Siegfried Janz, Miroslaw Florjanczyk, Dan-Xia Xu, Edith Post and especially Pavel Cheben for all valuable comments and discussions as well as for their hospitality during my stay at the Optoelectronic Devices Group, Institute of Microstructural Sciences, National Research Council of Canada. Technical support and commercial assistance rendered by GreenLight Solutions; Ana Manzanares and Luz Pérez, are also gratefully acknowledged.

En estas ultimas líneas quiero hacer constar especialmente, tanto mi agradecimiento como reconocimiento a quienes han dedicado de forma ejemplar tanto tiempo y profesionalidad a esta Tesis: Tatiana Alieva, María Luisa Calvo, Pavel Cheben y Óscar Martinez-Matos. Sin duda alguna vuestra impronta está presente tanto en mí como en este trabajo. Me considero afortunado por haberme permitido realizar una investigación tan interesante como prolífica a nivel teórico y experimental. Sin embargo, aún más afortunado soy por haber compartido estos cuatro años con vosotros.

Gracias

Publications

Papers

- J. A. Rodrigo, T. Alieva, M. L. Calvo, "Optical system design for ortho-symplectic transformations in phase space," J. Opt. Soc. Am. A **23**, 2494-2500 (2006).
- J. A. Rodrigo, T. Alieva, M.L. Calvo, "Flexible Optical System for Separable Fractional Fourier Transform," 5th International Workshop on Information Optics (G. Cristobal, B. Javidi, S. Vallmitjana, eds.), AIP Conference Proc., ISBN: 978-0-7354-0356-7, **890**, pp. 220-224 (2006).
- J. A. Rodrigo, T. Alieva, M. L. Calvo, "Gyrator transform: properties and applications," Opt. Express **15**, 2190-2203, (2007).
- J. A. Rodrigo, T. Alieva, and M. L. Calvo, "Experimental implementation of the gyrator transform," J. Opt. Soc. Am. A **24**, pp. 3135-3139 (2007).
- J. A. Rodrigo, T. Alieva, and M. L. Calvo, "Applications of gyrator transform for image processing," Opt. Commun. **278**, pp. 279-284 (2007).
- J. A. Rodrigo, P. Cheben, T. Alieva, M. L. Calvo, M. Florjanczyk, S. Janz, A. Scott, B. Solheim, D.-X. Xu and A. Delâge, "Fresnel diffraction effects in Fourier Transform arrayed waveguide grating spectrometer," Opt. Express, **15**, pp. 16431-16441 (2007).
- T. Alieva, J. A. Rodrigo, and M. L. Calvo, "Introduction to gyrator transform," 6th Euro American Workshop on Information Optics. AIP Conference Proc., **949**, (J. A. Benediktsson, B. Javidi, and K. S. Gudmundsson, eds.), ISBN 978-0-7354-0463-2, pp. 256-263 (2007).

Other publications

- J. A. Davis , L. Ramirez , J. A. Rodrigo, T. Alieva and M. L. Calvo, "Focusing properties of fractal zone plates: experimental implementation with a liquid-crystal display," Optics Letters, **29**, pp. 1321-1323, (2004).
- J. A. Rodrigo, T. Alieva, M. L. Calvo, and J. A. Davis, "Diffraction by Cantor fractal zone plates," J. Mod. Optics, **52**, 2771-2783 (2005).
- M. L. Calvo, P. Cheben, O. Martínez Matos, F. del Monte, and J. A. Rodrigo, "Experimental Detection of Optical Pendellosung Effect," Phys. Rev. Lett., **97**, pp. 084801 (2006).
- F. del Monte, O. Martínez, J. A. Rodrigo, M. L. Calvo, and P. Cheben, "A Volume Holographic Sol-Gel Material with Large Enhancement of Dynamic Range by Incorporation of High Refractive Index Species," Adv. Mater., **18**, pp. 2014–2017 (2006).

- O. Martínez Matos, M. L. Calvo, P. Cheben, S. Janz, J. A. Rodrigo, D.-X. Xu and A. Delâge, "Arrayed waveguide grating based on group index modification," J. of Lightwave Technology, **24**, pp. 1551 (2006).
- J. A. Rodrigo , T. Alieva, M. L. Calvo, J. A. Davis,L. Ramirez, "Cantor fractal zone plates: numerical simulation and experimental characterization," 5th Iberoamerican Meeting on Optics and 8th Latin American Meeting on optics, Lasers and their Applications (A. Marcano, J. L. Paz, eds.), Proc. SPIE, **5622**, pp. 1474-1477 (2004).
- O. Martínez Matos, M. L. Calvo, P. Cheben, S. Janz, J. A. Rodrigo, D.-X. Xu and André Delâge, "A novel wavelength dispersive device with a dispersive element based on staircase-like straight and parallel arrayed waveguides,"Opt. Commun., **270**, pp. 31-40 (2007).
- O. Martínez Matos, M. L. Calvo, J. A. Rodrigo, P. Cheben, F. Del Monte, "Diffusion study in tailored gratings recorded in photopolymer glass with high refractive index species," Appl. Phys. Letts., **91**, pp. 141115 (2007).

Congress contributions

- T. Alieva, J. A. Rodrigo, and M. L. Calvo, "Introduction to Gyrator Transform,"Sixth Euro American Workshop on Information Optics, Iceland, June 25-30 (2007), ISBN 978-0-7354-0463-2, pp. 256-263.
- J. A. Rodrigo, P. Cheben, T. Alieva, M. L. Calvo, M. Florjanczyk, S. Janz, A. Scott, B. Solheim, and D.-X. Xu,"Moiré-Talbot effect in Fourier-transform arrayed waveguide grating devices,"Photonics North,Ottawa, Canada, June 4-6 (2007), pp. 248.
- J. A. Rodrigo T. Alieva and M. L. Calvo, "SLM optical system implementation for separable fraccional Fourier transform,"ICO Topical meeting on Optoinformatics/Information Photonics, St. Petersburg, Russia, September 4-7 (2006), ISBN 5-7921-0719-6, pp. 231-233.
- J. A. Rodrigo T. Alieva and M. L. Calvo,"Flexible optical system for separable fractional Fourier transform,"5th International Workshop on Information Optics, Toledo, Spain, June 5-7 (2006), ISBN 978-0-7354-0356-7, pp. 220-224.
- P. Cheben, J. Schmid, A. Bogdanov, M. L. Calvo, A. Delage, A. Densmore, S. Janz, B. Lamontagne, J. Lapointe, O. M. Matos, E. Post, I. Powell, J. A. Rodrigo, P. Waldron and D.X. Xu, "Advanced concepts in waveguide spectrometers,"3rd IEEE International Conference on Group IV Photonics, September 13-15 (2006), pp. 246-248.
- J. A. Rodrigo, T. Alieva, M. L. Calvo, J. A. Davis, L. Ramirez, "Cantor fractal zone plates: numerical simulation and experimental characterization,"RIAO/OPTILAS 2004, Porlamar, Venezuela, October 3-8 (2004), Proceeding of SPIE, Vol. 5622, pp. 5622-276.

Bibliography

[1] A. V. der Lugt, ed., *Optical Signal Processing* (Wiley Series in Pure and Applied Optics, JohnWiley, New York, NY, USA, 1992).

[2] G. O. Reynolds, J.B.DeVelis, B. Parrent, and B. J. Thompson, *Physical Optical Notebook: Tutorials in Fourier Optics* (SPIE Optical Engineering Press, New York, NY, USA, 1989).

[3] S. Mallat, *A Wavelet Tour of Signal Processing,* (Academic Press, ISBN : 0-12-466606-X, 1999).

[4] Y. Li, H. H. Szu, Y. Sheng, and H. J. Caulfield, "Wavelet processing and optics," Proc. IEEE **84**, 720–732 (1996).

[5] A. Walther, "Radiometry and coherence," J. Opt. Soc. Am. **58**, 1256 (1968).

[6] A. Walther, "Propagation of the generalized radiance through lenses," J. Opt. Soc. Am. **68**, 1606 (1978).

[7] A. Papoulis, "Ambiguity function in Fourier optics," J. Opt. Soc. Am. **64**, 779 (1974).

[8] M. J. Bastiaans, "The Wigner distribution function applied to optical signals and systems," Opt. Commun. **25**, 26–30 (1978).

[9] M. J. Bastiaans, "Wigner distribution function and its application to first-order optics," J. Opt. Soc. Am. **69**, 1710–1716 (1979).

[10] M. J. Bastiaans, "Application of the Wigner distribution function to partially coherent light," J. Opt. Soc. Am. A **3**, 1227 (1986).

[11] W. Mecklenbrauker and F. Hlawatsch, eds., *The Wigner Distribution - Theory and Applications in Signal Processing* (Elsevier, Amsterdam, The Netherlands, 1997).

[12] H. M. Ozaktas, Z. Zalevsky, and M. A. Kutay, *The Fractional Fourier Transform with Applications in Optics and Signal Processing* (John Wiley&Sons, NY, USA, 2001).

[13] T. Alieva, V. Lopez, F. A. Lopez, and L. B. Almeida, "The fractional Fourier transform in optical propagation problems," J. Mod. Opt. **41**, 1037–1044 (1994).

[14] H. Kober, "Wurzeln aus der Hankel-, Fourier- und aus anderen stetigen Transformationen," Quart. J. Math. Oxford. **10**, 45–59 (1939).

[15] V. Namias, "The fractional order Fourier transform and its applications to quantum mechanics," Journal of the Institute of Mathematics and Its Applications **25**, 241–265 (1980).

[16] A. C. McBride and F. H. Kerr, "On namias fractional Fourier transforms," IMA Journal of Applied Mathematics **39**, 159–175 (1987).

[17] A. W. Lohmann, "Image rotation, Wigner rotation, and the fractional Fourier transform," J. Opt. Soc. Am. A **10**, 2181 (1993).

[18] L. B. Almeida, "The fractional Fourier transform and timefrequency representations," IEEE Trans. Signal Processing **42**, 3084Ű–3091 (1994).

[19] T. Alieva and M. L. Calvo, "Fractionalization of the linear cyclic transforms," J. Opt. Soc. Am. A **17**, 2330–2338 (2000).

[20] A. Torre, "The fractional Fourier transform and some of its applications to optics," Progress in Optics **43**, 531Ű–596 (2002).

[21] M. G. Raymer, M. Beck, and D. F. McAlister, "Complex wave-field reconstruction using phase-space tomography," Physical Review Letters **72**, 1137Ű–1140 (1994).

[22] T. Alieva and M. J. Bastiaans, "On fractional Fourier transform moments," IEEE Signal Processing Lett. **7**, 320–Ű323 (2000).

[23] T. Alieva and M. J. Bastiaans, "Phase-space distributions in quasi-polar coordinates and the fractional Fourier transform," J. Opt. Soc. Am. A **17**, 2324–2329 (2000).

[24] T. Alieva, M. J. Bastiaans, and L. Stanković, "Signal reconstruction from two close fractional Fourier power spectra," IEEE Trans. Signal Processing **51**, 112Ű–123 (2003).

[25] M. J. Bastiaans and K. B. Wolf, "Phase reconstruction from intensity measurements in linear systems," J. Opt. Soc. Am. A **20**, 1046–1049 (2003).

[26] M. R. Teague, "Deterministic phase retrieval: a Green's function solution," J. Opt. Soc. Am. **73**, 1434 (1983).

[27] Z. Zalevsky, D. Mendlovic, and R. G. Dorsch, "Gerchberg-Saxton algorithm applied in the fractional Fourier or the Fresnel domain," Opt. Lett. **21**, 842 (1996).

[28] B.-Z. Dong, Y. Zhang, B.-Y. Gu, and G.-Z. Yang, "Numerical investigation of phase retrieval in a fractional Fourier transform," J. Opt. Soc. Am. A **14**, 2709–2714 (1997).

[29] W.-X. Cong, N.-X. Chen, and B.-Y. Gu, "Recursive algorithm for phase retrieval in the fractional Fourier transform domain," Appl. Opt. **37**, 6906–6910 (1998).

[30] T. Alieva and M. J. Bastiaans, "Finite-mode analysis by means of intensity information in fractional optical systems," J. Opt. Soc. Am. A **19**, 481–484 (2002).

[31] T. Alieva, M. L. Calvo, and M. J. Bastiaans, "Power filtering of nth order in the fractional Fourier domain," Journal of Physics A: Mathematical and General **35**, 7779–7785 (2002).

[32] M. J. Bastiaans and T. Alieva, "Wigner distribution moments in fractional Fourier transform systems," J. Opt. Soc. Am. A **19**, 1763–1773 (2002).

[33] M. J. Bastiaans and T. Alieva, "Wigner distributionmoments measured as intensity moments in separable first-order optical systems," EURASIP Journal on Applied Signal Processing **2005**, 1535Ű–1540 (2005).

[34] L. Stanković, T. Alieva, and M. J. Bastiaans, "Time-frequency signal analysis based on the windowed fractional Fourier transform," Signal Processing **83**, 2459–2468 (2003).

[35] M. J. Bastiaans, T. Alieva, and L. Stanković, "On rotated time-frequency kernels," IEEE Signal Processing Lett. **9**, 378Ű–381 (2002).

[36] T. Alieva and M. J. Bastiaans, "Evolution of the vortex and the asymmetrical parts of orbital angularmomentum in separable first-order optical systems," Opt. Lett. **29**, 1587–1589 (2004).

[37] J. C. Wood and D. T. Barry, "Tomographic time-frequency analysis and its application toward time-varying filtering and adaptive kernel design for multicomponent linear-fm signals," IEEE Trans. Signal Processing **42**, 2094–2104 (1994).

[38] J. C. Wood and D. T. Barry, "Linear signal synthesis using the radon-Wigner transform," IEEE Trans. Signal Processing **42**, 2105–2111 (1994).

[39] H. M. Ozaktas, B. Barshan, D. Mendlovic, and L. Onural, "Convolution, filtering, and multiplexing in fractional Fourier domains and their relation to chirp and wavelet transforms," J. Opt. Soc. Am. A **11**, 547 (1994).

[40] L. B. Almeida, "Product and convolution theorems for the fractional Fourier transform," IEEE Signal Processing Lett. **4**, 15Ű–17 (1997).

[41] D. Mendlovic, H. M. Ozaktas, and A. W. Lohmann, "Fractional correlation," Appl. Opt. **34**, 303 (1995).

[42] D. Mendlovic, Y. Bitran, R. G. Dorsch, and A. W. Lohmann, "Optical fractional correlation: experimental results," J. Opt. Soc. Am. A **12**, 1665 (1995).

[43] Z. Zalevsky and D. Mendlovic, "Fractional Wiener filter," Appl. Opt. **35**, 3930 (1996).

[44] D. J. Mustard, "Fractional convolution," Journal of the Australian Mathematical Society. Series B: Applied Mathematics **40**, 257Ű–265 (1998).

[45] B. Ruiz and H. Rabal, "Fractional Fourier transform description with use of differential operators," J. Opt. Soc. Am. A **14**, 2905–2913 (1997).

[46] A. I. Zayed, "A convolution and product theorem for the fractional Fourier transform," IEEE Signal Processing Lett. **5**, 101Ű–103 (1998).

[47] I. Raveh and D. Mendlovic, "New properties of the Radon transform of the cross Wigner/ambiguity distribution function," IEEE Trans. Signal Processing **47**, 2077Ű–2080 (1999).

[48] A. W. Lohmann, Z. Zalevsky, and D. Mendlovic, "Synthesis of pattern recognition filters for fractional Fourier processing," Opt. Commun. **128**, 199Ű204 (1996).

[49] S. Granieri, R. Arizaga, and E. E. Sicre, "Optical correlation based on the fractional Fourier transform," Appl. Opt. **36**, 6636–6645 (1997).

[50] A. M. Almanasreh and M. A. G. Abushagur, "Fractional correlations based on the modified fractional order Fourier transform," Optical Engineering **37**, 175Ű–184 (1998).

[51] O. Akay and G. F. Boudreaux-Bartels, "Fractional convolution and correlation via operator methods and an application to detection of linear fm signals," IEEE Trans. Signal Processing **49**, 979Ű–993 (2001).

[52] J. A. Davis, D. M. Cottrell, N. Nestorovic, and S. M. Highnote, "Space-variant Fresnel transform optical correlator," Appl. Opt. **31**, 6889 (1992).

[53] D. Mendlovic, Y. Bitran, R. G. Dorsch, C. Ferreira, J. Garcia, and H. M. Ozaktaz, "Anamorphic fractional Fourier transform: optical implementation and applications," Appl. Opt. **34**, 7451 (1995).

[54] J. Garcia, D. Mendlovic, Z. Zalevsky, and A. Lohmann, "Space-variant simultaneous detection of several objects by the use of multiple anamorphic fractional-Fourier-transform filters," Appl. Opt. **35**, 3945 (1996).

[55] J. Garcí́a, R. G. Dorsch, A. W. Lohmann, C. Ferreira, and Z. Zalevsky, "Flexible optical implementation of fractional Fourier transform processors. applications to correlation and filtering," Opt. Commun. **133**, 393Ű–400 (1997).

[56] Y. Bitran, Z. Zalevsky, D. Mendlovic, and R. G. Dorsch, "Fractional correlation operation: performance analysis," Appl. Opt. **35**, 297 (1996).

[57] T. Alieva and M. L. Calvo, "Importance of the phase and amplitude in the fractional Fourier domain," J. Opt. Soc. Am. A **20**, 533–541 (2003).

[58] F. T. S. Yu, C. Zhang, Y. Jin, and D. A. Gregory, "Nonconventional joint-transform correlator," Opt. Lett. **14**, 922 (1989).

[59] G. Unnikrishnan and K. Singh, "Optical encryption using quadratic phase systems," Opt. Commun. **193**, 51Ű–67 (2001).

[60] B. Zhu, S. Liu, and Q. Ran, "Optical image encryption based on multifractional Fourier transforms," Opt. Lett. **25**, 1159–1161 (2000).

[61] B. Zhu and S. Liu, "Optical image encryption based on the generalized fractional convolution operation," Opt. Commun. **195**, 371–381 (2001).

[62] N. K. Nishchal, G. Unnikrishnan, J. Joseph, and K. Singh, "Optical encryption using a localized fractional Fourier transform," Optical Engineering **42**, 566–3571 (2003).

[63] B. Hennelly and J. T. Sheridan, "Optical image encryption by random shifting in fractional Fourier domains," Opt. Lett. **28**, 269–271 (2003).

[64] B. Hennelly and J. T. Sheridan, "Fractional Fourier transform-based image encryption: phase retrieval algorithm," Opt. Commun. **226**, 61–80 (2003).

[65] B. M. Hennelly and J. T. Sheridan, "Image encryption and the fractional Fourier transform," Optik **114**, 251–265 (2003).

[66] N. K. Nishchal, J. Joseph, and K. Singh, "Fully phase encryption using fractional Fourier transform," Optical Engineering **42**, 1583Ű–1588 (2003).

[67] S. Stankovic, I. Djurovic, and I. Pitas, "Watermarking in the space/spatial-frequency domain using two-dimensional radon-Wigner distribution," IEEE Trans. Image Processing **10**, 650–658 (2001).

[68] S. S. I. Djurovic and I. Pitas, "Digital watermarking in the fractional Fourier transformation domain," Journal of Network and Computer Applications **24**, 167–173 (2001).

[69] S.-Y. Lee and H. H. Szu, "Fractional Fourier transforms, wavelet transforms, and adaptive neural networks," Optical Engineering **33**, 2326–2330 (1994).

[70] S.-G. Shin, S.-I. Jin, S.-Y. Shin, , and S.-Y. Lee, "Optical neural network using fractional Fourier transform, log-likelihood, and parallelism," Opt. Commun. **153**, 218Ű–222 (1998).

[71] S.-I. Jin, Y.-S. Bae, and S.-Y. Lee, "Generalized Vander Lugt correlator as an optical pattern classifier and its optimal learning rate," Opt. Commun. **206**, 19Ű–25 (2002).

[72] B. Barshan and B. Ayrulu, "Fractional Fourier transform pre-processing for neural networks and its application to object recognition," Neural Networks **15**, 131–140 (2002).

[73] B. Barshan and B. Ayrulu, "Comparative analysis of different approaches to target differentiation and localization with sonar," Pattern Recognition **36**, 1213–1231 (2003).

[74] S. Q. Zhang and M. A. Karim, "Fractional correlation filter for fuzzy associative memories," Optical Engineering **41**, 126–129 (2002).

[75] A. W. Lohmann, E. Tepichín, and J. G. Ramírez, "Optical implementation of the fractional Hilbert transform for two-dimensional objects," Appl. Opt. **36**, 6620–6626 (1997).

[76] A. W. Lohmann, D. Mendlovic, and Z. Zalevsky, "Fractional Hilbert transform," Opt. Lett. **21**, 281 (1996).

[77] A. W. Lohmann, E. Tepichín, and J. G. Ramírez, "Optical implementation of the fractional Hilbert transform for two-dimensional objects," Appl. Opt. **36**, 6620–6626 (1997).

[78] J. A. Davis, D. E. McNamara, and D. M. Cottrell, "Analysis of the fractional Hilbert transform," Appl. Opt. **37**, 6911–6913 (1998).

[79] Y. Zhang, G. Pedrini, W. Osten, and H. J. Tiziani, "Applications of fractional transforms to object reconstruction fromin-line holograms," Opt. Lett. **29**, 1793–1795 (2004).

[80] T. Alieva, M. Bastiaans, and M. L. Calvo, "Fractional transforms in optical information processing," EURASIP J. Appl. Signal Process **2005**, 1498–1519 (2005).

[81] T. Alieva and M. Bastiaans, "Alternative representation of the linear canonical integral transform," Opt. Lett. **30**, 3302–3304 (2005).

[82] R. K. Luneburg, *Mathematical Theory of Optics* (University of California Press, Berkeley and Los Angeles, CA, USA, 1966).

[83] K. B. Wolf, *Geometric Optics on Phase Space* (Springer-Verlag, Berlin, 2004).

[84] R. Simon and K. B. Wolf, "Structure of the set of paraxial optical systems," J. Opt. Soc. Am. A **17**, 342–355 (2000).

[85] H. Braunecker, O. Bryngdahl, and B. Schnell, "Optical system for image rotation and magnification," J. Opt. Soc. Am. **70**, 137–141 (1980).

[86] R. Simon and K. B. Wolf, "Fractional Fourier transforms in two dimensions," J. Opt. Soc. Am. A **17**, 2368–2381 (2000).

[87] J. Shamir, "Cylindrical lens described by operator algebra," Appl. Opt. **18**, 4195–4202 (1979).

[88] B. Macukow and H. H. Arsenault, "Matrix decomposition for nonsymmetrical optical systems," J. Opt. Soc. Am. **73**, 1360–1366 (1983).

[89] D. Mendlovic and H. M. Ozaktas, "Fractional Fourier transform and their optical implementation," J. Opt. Soc. Am. A **10**, 1875–1881 (1993).

[90] A. W. Lohmann, "Image rotation, Wigner rotation, and the fractional order Fourier transform," J. Opt. Soc. Am. A **10**, 2181–2186 (1993).

[91] G. Nemes and A. Kostenbauder, "Optical systems for rotating a beam," in "Proceeding of the Workshop on laser Beam Characterization," , P. M. Mejias, H. Weber, R. Martinez-Herrero, and A. Gonzales-Urena, eds. (Sociedad Española de Optica, Madrid., 1993), pp. 99–109.

[92] G. Nemes and A. E. Seigman, "Measurement of all ten second-order moments of an astigmatic beam by use of rotating simple astigmatic (anamorphic) optics," J. Opt. Soc. Am. A **11**, 2257–2264 (1994).

[93] D. Mendlovic, Y. Bitran, R. G. Dorsch, C. Ferreira, J. Garcia, and H. M. Ozaktas, "Anamorphic fractional Fourier transform: optical implementation and applications," Appl. Opt. **34**, 7451–7456 (1995).

[94] M. F. Erden, H. M. Ozaktas, A. Sahin, and D. Mendlovic, "Design of dynamically adjustable anamorphic fractional transformer Fourier," Opt. Commun. **136**, 52–60 (1997).

[95] A. Sahin, H. M. Ozaktas, and D. Mendlovic, "Optical implementations of two-dimensional fractional Fourier transforms and linear canonical transforms with arbitrary parameters," Appl. Opt. **37**, 2130–2141 (1998).

[96] I. Moreno, J. A. Davis, and K. Crabtree, "Fractional Fourier transform optical system with programmable diffractive lenses," Appl. Opt. **42**, 6544–6548 (2003).

[97] A. A. Malyutin, "Tunable Fourier transformer of the fractional order," Quantum Electronics **36**, 79–83 (2006).

[98] M. W. Beijersbergen, L. Allen, H. E. L. O. van der Veenand, and J. P. Woerdman, "Astigmatic laser mode converters and transfer of orbital angular momentum," Opt. Commun. **96**, 123–132 (1993).

[99] E. G. Abramochkin and V. G. Volostnikov, "Generalized Gaussian beams," J. Opt. A. Pure Appl. Opt. **6**, S157–S161 (2004).

[100] C. Gómez-Reino, M. V. Pérez, and C. Bao, *Gradient-Index Optics: Fundamentals and Applications* (Springer-Verlag, Berlin 2002. ISBN: 3-540-42125-4, 2002).

[101] J. Stuart A. Collins, "Lens-system diffraction integral written in terms of matrix optics," J. Opt. Soc. Am. **60**, 1168 (1970).

[102] J. W. Goodman, *Introduction to Fourier Optics,* (McGraw-Hill, New York, 1996).

[103] P. Pellat-Finet, "Fresnel diffraction and fractional-order Fourier transform," Opt. Lett. **19**, 1388 (1994).

[104] P. Pellat-Finet and G. Bonnet, "Fractional order Fourier transform and Fourier optics," Opt. Commun. **111**, 141–154 (1994).

[105] H. M. Ozaktas and D.Mendlovic, "Fractional Fourier transform as a tool for analyzing beam propagation and spherical mirror resonators," Optics Letters **19**, 1678–1680 (1994).

[106] M. Bastiaans and T. Alieva, "First-order optical systems with unimodular eigenvalues," J. Opt. Soc. Am. A **23**, 1875–1883 (2006).

[107] J. A. Rodrigo, T. Alieva, and M. L. Calvo, "Optical system design for orthosymplectic transformations in phase space," J. Opt. Soc. Am. A **23**, 2494–2500 (2006).

[108] I. Moreno, G. Paez, and M. Strojnik, "Polarization transforming properties of dove prisms," Opt. Commun. **220**, 257Ű–268 (2003).

[109] I. Moreno, "Jones matrix for image-rotation prisms," Appl. Opt. **43**, 3373–3381 (2004).

[110] E. G. Abramochkin and V. G. Volostnikov, "Beam transformations and nontransformed beams," Opt. Commun. **83**, 123–135 (1991).

[111] G. F. Calvo, "Wigner representation and geometric transformations of optical orbital angular momentum spatial modes," Opt. Lett. **30**, 1207–1209 (2005).

[112] T. Alieva and M. J. Bastiaans, "Orthonormal mode sets for the two-dimensional fractional Fourier transformation," Opt. Lett. **32**, 1226–1228 (2007).

[113] V. V. Kotlyar, S. N. Khonina, A. A. Almazov, V. A. Soifer, K. Jefimovs, and J. Turunen, "Elliptic Laguerre-Gaussian beams," J. Opt. Soc. Am. A **23**, 43–56 (2006).

[114] T. Alieva and M. Bastiaans, "Mode mapping in paraxial lossless optics," Opt. Lett. **30**, 1461–1463 (2005).

[115] J. F. Nye and M. V. Berry, "Dislocations in wave trains," in "Proc. R. Soc. London Ser. A," , vol. 336 (1974), vol. 336, pp. 165–90.

[116] J. Masajada and B. Dubik, "Optical vortex generation by three plane wave interference," Opt. Commun. **198**, 21–27 (2001).

[117] L. Allen, M. W. Beijersbergen, R. J. C. Spreeuw, and J. P. Woerdman, "Orbital angular momentum of light and the transformation of Laguerre-Gaussian laser modes," Phys. Rev. A **45**, 8185–8189 (1992).

[118] H. He, M. E. J. Friese, N. R. Heckenberg, and H. Rubinsztein-Dunlop, "Direct Observation of Transfer of Angular Momentum to Absorptive Particles from a Laser Beam with a Phase Singularity," Phys. Rev. Lett. **75**, 826–829 (1995).

[119] A. Mair, A. Vaziri, G. Weihs, and A. Zeilinger, "Entanglement of the orbital angular momentum states of photons," Nature **412**, 313–316 (2001).

[120] L. Paterson, M. P. MacDonald, J. Arlt, W. Sibbett, P. E. Bryant, and K. Dholakia, "Controlled rotation of optically trapped microscopic particles," Science **292**, 912–914 (2001).

[121] A. Jesacher, S. Fürhapter, S. Bernet, and M. Ritsch-Marte, "Shadow effects in spiral phase contrast microscopy," Physical Review Letters **94**, 233902 (2005).

[122] J. A. Rodrigo, T. Alieva, and M. L. Calvo, "Gyrator transform: properties and applications," Opt. Express **15**, 2190–2203 (2007).

[123] T. Alieva and M. L. Calvo, "Importance of the phase and amplitude in the fractional Fourier domain," J. Opt. Soc. Am. A **20**, 533–541 (2003).

[124] T. Alieva and M. L. Calvo, "Image reconstruction from amplitude only and phase only data in the fractional Fourier domain," Opt. & Spectr. **95**, 110–113 (2003).

[125] G. Unnikrishnan, J. Joseph, and K. Singh, "Optical encryption by double-random phase encording in the fractional Fourier domain," Opt. Lett. **25**, 887 (2000).

[126] B. Zhu, S. Liu, and Q. Ran, "Optical image encryption based on multifractional Fourier transforms," Opt. Lett. **25**, 1159–1161 (2000).

[127] J. A. Rodrigo, T. Alieva, and M. L. Calvo, "Applications of gyrator transform for image processing," Opt. Commun. **278**, 279–284 (2007).

[128] V. A. Soifer, ed., *Methods for Computer Design of Diffractive Optical Elements* (Wiley, 2002).

[129] J. A. Rodrigo, T. Alieva, and M. L. Calvo, "Experimental implementation of the gyrator transform," J. Opt. Soc. Am. A **24**, 3135–3139 (2007).

[130] P. Cheben, J. H. Schmid, A. Delâge, A. Densmore, S. Janz, B. Lamontagne, J. Lapointe, E. Post, P. Waldron, and D.-X. Xu, "A high-resolution silicon-on-insulator arrayed waveguide grating microspectrometer with submicrometer aperture waveguides," Opt. Express **15**, 2299–2306 (2007).

[131] P. Cheben, I. Powell, S. Janz, and D.-X. Xu, "Wavelength-dispersive device based on a Fourier-transform michelson-type arrayed waveguide grating," Opt. Lett. **30**, 1824–1826 (2005).

[132] P. Cheben, A. Delâge, L. Erickson, S. Janz, and D.-X. Xu, "Polarization compensation in silicon-on-insulator arrayed waveguide grating devices," in "Silicon-based and hybrid optoelectronics III," , vol. 4293 (SPIE Proc, 2001), vol. 4293, pp. 15–22.

[133] M. Florjanczyk, P. Cheben, S. Janz, A. Scott, B. Solheim, and D.-X. Xu, "Multiaperture planar waveguide spectrometer formed by arrayed Mach-Zehnder interferometers," Opt. Express **15**, 18176–18189 (2007).

[134] P. Cheben, D.-X. Xu, S. Janz, A. Delâge, and D. Dalacu, "Birefringence compensation in silicon-on-insulator planar waveguide demultiplexers using a buried oxide layer," in "Optoelectronic Integration on Silicon," , vol. 4997 (SPIE, 2003), vol. 4997, pp. 181–189.

[135] P. Cheben, *Optical Waveguides: From Theory to Applied Technologies* (CRC Press, London, 2007), chap. Wavelength dispersive planar waveguide devices: Echelle gratings and arrayed waveguide gratings.

[136] M. K. Smit and C. van Dam, "Phasar-based WDM-devices: principles, design, and applications," IEEE J. Sel. Top. Quantum Electron **2**, 236 (1996).

[137] H. Hamam and J. L. D. B. de la Tocnaye, "Programmable joint fractional talbot computer-generated holograms," J. Opt. Soc. Am. A **12**, 314 (1995).

[138] H. Hamam and J. L. de Bougrenet de la Tocnaye, "Efficient Fresnel transform algorithm based on fractional Fresnel diffraction," J. Opt. Soc. Am. A **12**, 1920 (1995).

[139] J. A. Rodrigo, P. Cheben, T. Alieva, M. L. Calvo, M. Florjanczyk, S. Janz, A. Scott, B. Solheim, D. X. Xu, and A. Deláge, "Fresnel diffraction effects in Fourier-transform arrayed waveguide grating spectrometer," Opt. Express **15**, 16431–16441 (2007).

[140] D. Mendlovic, Z. Zalevsky, and N. Konforti, "Computation considerations and fast algorithms for calculating the diffraction integral," J. Mod. Opt. **44**, 1997 (407).

[141] D. Mas, J. Perez, C. Hernandez, C. Vazquez, J. J. Miret, and C. Illueca, "Fast numerical calculation of Fresnel patterns in convergent systems," Opt. Commun. **227**, 245–258 (2003).

[142] I. S. Gradstein and I. M. Ryzik, *Table of Integrals, Series, and Products* (Academic Press, Boston, 1994).

Glosario

AWG Arrayed Waveguide Gratting. Page xx

DVI Digital Visual Interface. Page 76

FFT Fast Fourier Transform. Page 57

FRFT Fractional Fourier Transform. Page xix

FT Fourier Transform. Page xix

GT Gyrator Transform. Page xix

HG Hermite-Gaussian. Page 27

HIC High index contrast. Page 53

LCT Linear Canonical Integral Transform. Page xix

LG Laguerre-Gaussian. Page 27

OAM Orbital Angular Momentum. Page 33

SEM Scanning electron microscope. Page 53

SLM Spatial Light Modulator. Page xiii

SOI Silicon-on-insulator. Page 53